Interface and Additive Engineering to Improve Reproducibility and Performance of Bismuth-Based and Tin-Based Perovskite Solar Cells

Md. Abdul Karim

February 2023

Interface and Additive Engineering to Improve Reproducibility and
Performance of Bismuth-Based and Tin-Based Perovskite Solar Cells

Md. Abdul Karim
Doctoral Program in Engineering Sciences
Subprogram in Materials Science

Submitted to the
Degree Programs in Pure and Applied Sciences of the
Graduate School of Science and Technology
in Partial Fulfillment of the Requirements
for the Degree of Doctor of Philosophy in
Engineering

at the
University of Tsukuba

Abstract

Currently, renewable and clean energy sources are globally demandable, and photovoltaic technology is one of the sources of renewable energy. Photovoltaic technology can be an alternative source for the ongoing energy crisis and could avoid environmental pollution. Among the present photovoltaic technologies, perovskite solar cells (PSCs) based on organic-inorganic Pb semiconductor materials have aroused significant interest in a short time due to their high absorption coefficient, tunable bandgap, high charge carrier mobility, low cost, and low possessing temperature. Since the introduction of conventional lead (Pb) based PSCs in 2009, the fabrication process has been developed and reached a PCE of PSCs over 25%. The improvement of PSCs performance has been considerable and comparable with other solar cell technologies like traditional silicon solar cells. Unfortunately, the toxicity of Pb is possibly harmful to the ecosystem and unsuitable for large-scale production and commercialization.

This thesis work focuses on developing semiconductor materials that have excellent optoelectronic properties without toxicity issues for large-scale production. In this thesis work, I focused on the two types of Pb-free semiconductor materials, bismuth (Bi) and tin (Sn) perovskite, as absorber materials in PSCs application.

Bi-halide semiconductor materials might be a suitable alternative to Pb-based semiconductors due to the same electronic configuration ([Xe] $4f^{14}5d^{10}6s^26p^0$). Bi perovskite with $CsBi_3I_{10}$ (CBI) composition has a band gap of 1.77 eV and an absorption coefficient of 1.4 x 10^5 cm^{-1}, which is comparable to the Pb-based perovskite in the absorption spectrum ranging from 350 to 500 nm. Unfortunately, Bi-based perovskite semiconductors have lower crystallinity, and fabricated PSCs showed a lack of reproducibility and stability. We found the possible reasons for the lower quality of crystal as well as reproducibility and stability. To improve the crystal quality of fabricated Bi-perovskite films, we optimized the suitable fabrication condition, like the molarity of the precursor solution and post-annealing temperature of the films. After that, we introduced the bathocuproine (BCP) interfacial layer (BIL) at the perovskite/ETL interface as a structural modification engineering of the respective PSC with the configuration of ITO/PEDOT: PSS/CBI/BCP/C$_{60}$/BCP/Ag. The wider bandgap n-type semiconductor BCP can improve the electrical interface contact of the perovskite/ETL interface, thus limiting the possibility of hole leakage to the ETL from the HTL and improving overall PSC performance. The modified

structure with a 6 nm sized BIL in the perovskite/ETL interface of the PSC demonstrated a maximum PCE of 0.80%. Furthermore, the good reproducibility of photovoltaic performance has been observed for PSCs with BIL at the perovskite/ETL interface, which is a promising result for developing CBI-based PSCs. The best-performing PSC with a 6-nm-sized BIL demonstrated long-term air stability and retained ~90% of its initial PCE even after 528 h.

Although Bi-perovskite has many suitable properties which are comparable to Pb-perovskite, in terms of PSCs performance, Bi-PSCs are far behind from Pb-PSCs. Due to the poor crystallinity and higher band gap of Bi-perovskite, the PCE of Bi-PSCs is lower than that of Pb-PSCs. Fortunately, tin (Sn) belongs to group IV in the periodic table. It is a promising candidate for a non-toxic divalent metal cation as an alternative to Pb. The Sn-based perovskite has higher charge carrier mobility, a lower exciton binding energy, and a slightly smaller radius than Pb^{2+}.

Moreover, Sn perovskite could have a band gap between 1.1 and 1.4 eV, and it could reach the highest efficiency of 33.7% at 1.34 eV according to the Shockley-Queisser limit. Although Sn-PSCs have achieved PCE of over 14%, the performance of Sn-PSCs is still lower than Pb-PSCs due to some chemical constraints. The performance limiting factors have been associated with the notorious oxidation of Sn^{2+} to Sn^{4+} of the Sn perovskite absorber during the fabrication process and anionic vacancies (I^- losses), which lead to severe defects in Sn-perovskite. In addition, the fast crystallization during the spin-coated process forms inferior-quality films with small grain sizes, pinholes, and incomplete coverage. These problems collectively generate electronic defects which induce trap-assisted nonradiative recombination resulting in low PCE.

To address the problems of Sn^{2+} oxidation and I^- losses of fabricated Sn perovskite films, the additive with Cl^- ion is crucially essential to slow down the nucleation process and enhance the perovskite films quality.

In this thesis work, we introduced guanidine-based 1,3-diaminoguanidine monohydrochloride (DAGCl) additive as an electronic defect passivation agent in the precursor solution of $FASnI_3$ perovskite. The interaction between DAG^+ ion of DAGCl and the iodide ion (I^-) of SnI_2 formed hydrogen bonding and suppressed the I^- loss of the perovskite framework. Moreover, the Cl^- ion formed co-ordination with undercoordinated Sn^{2+} ions and stabilized the $FASnI_3$ perovskite structure with effective suppression of

oxidation of Sn^{2+} to Sn^{4+}. Suppressing the oxidation of Sn^{2+} and loss of I^- guaranteed a better Sn^{2+}/I^- stoichiometric ratio and showed a PCE of 8.92%.

Next, we investigated the origin of Sn^{2+} oxidation before film formation, and it was discovered that the ionization of SnI_2 in DMSO causes the oxidation of free Sn^{2+} ions and I^- ions due to the poor chemical stability of SnI_2-DMSO. We included the multifunctional additive 4-fluorophenylhydrazine hydrochloride (4-F-PHCl) in the FASnI3 perovskite precursor solution to address these issues. The hydrazine functional ($-NH-NH_2$) group may convert detrimental Sn^{4+} and I_2 defects back to Sn^{2+} and I^- in precursor solution while retaining the properties of perovskite solution. Furthermore, cations containing hydrazinium could passivate the cationic defect in the final $FASnI_3$ perovskite films. The 4F-PHCl additive in the perovskite films maintains moisture stability owing to the presence of a hydrophobic fluorinated benzene ring. As a result, 10% 4F-PHCl modified PSCs demonstrated a power conversion efficiency (PCE) of 10.86%, while unencapsulated PSCs retained more than 92% of their initial PCE in the N_2 glovebox for 80 days. This work opens the door to a more controlled Sn-based perovskite precursor solution for efficient and stable Pb-free PSCs.

Contents

CHAPTER 1: INTRODUCTION

Introduction

1.1 Motivation

1.1.1 Crisis of Energy

Energy is one of the fundamental needs of modern civilization. The increasing global population and rapid advancement of innovative technologies are driving an exponential energy need increase. To keep civilization in the right way, it is considerable that the energy demand is increased. There are several manifestations of energy, including nuclear energy, thermal energy, electrical energy, mechanical energy, magnetic energy, and chemical energy. Electrical energy is the most versatile kind of energy since it can be quickly transformed into any other type of energy that may be necessary. Electrical power is the primary resource upon which our contemporary society is now dependent.

In most cases, electricity is generated by the combustion of fossil fuels, various nuclear power sources, and other renewable energy sources. Nuclear power plants have lost their appeal in recent years because of concerns over safety and the complexity of the procedure for disposing of radioactive waste. In addition, several significant nuclear and radiation accidents have occurred throughout history. Moreover, the poor disposal system of radioactive waste puts the environment and human life in danger. From both a financial and a technical point of view, there is now no viable alternative to generating power via fossil fuel combustion. However, fossil fuels will not be able to satisfy the ever-increasing energy requirements of the global economy for much longer. It has been anticipated that oil and natural gas resources will be exhausted over the next few decades if other alternative energy sources are not discovered.

In addition, the burning of these fossil fuels emits greenhouse gases into the atmosphere, such as carbon dioxide (CO_2), which are the primary contributors to both global warming and changes in the climate.[1] Due to the presence of greenhouse gases, the temperature of the planet has grown.

In the modern world, people will have to find out how to satisfy a rising need for energy while preserving the integrity of the natural environment. Developing energy policies to find possible solutions to the energy crisis concerning environmental issues is essential. Renewable energy sources are the possible solution. The use of renewable energy sources has many advantages, some of which are that they have a low impact on the environment, emit very little or no carbon dioxide and other harmful gases into the atmosphere, are a natural resource that is not dependent on any external factors, and are an excellent supplement to conventional energy

sources. Increasing reliance on renewable energy may help to develop an environmentally friendly economy system.

1.1.2   Sources of Renewable Energy

Renewable energy, also known as "green energy," is energy produced from a natural source that is endless in supply. Renewable energy sources such as thermal energy, wave energy, wind energy, biomass energy, and solar energy have the potential to be converted into a kind of energy that is both environmentally friendly and harmless to the planet's atmosphere. When compared to other types of energy sources, the availability of renewable energy resources is widespread over the whole planet. Because of this, the expansion of renewable energy may help solve many of the most pressing problems we face today. It is anticipated that renewable energy sources will play a significant part in the transition of the world's energy system to one that is more secure, dependable, and environmentally friendly. In general, for renewable energy sources to be viable for everyday life, they need to have prices that are competitive with the energy supplied by traditional sources. Every different kind of renewable energy has its own set of constraints to deal with in this regard. For instance, the generation of electricity through hydropower is significantly more cost-effective than other methods; however, the most significant drawbacks of this method include the location of the plant, its reliance on rainfall, the cost of energy transmission, and its significant impact on the environment because of the need to flood a large area. Other renewable energy sources, such as geothermal, wave, and biomass, are not only exceedingly inefficient but also heavily dependent on the natural environment, making it impossible to use them in practical applications.[2] As a result, solar and wind power are the only viable alternatives to fossil fuels that provide any prospect of meeting the world's growing need for energy in the future. But these sources also have some unique drawbacks, such as the fact that they have a high cost of manufacture and are dependent on natural elements like the wind and the sun for their operation. Because of this dependence, the power grid, which integrates a significant proportion of wind and solar electricity, will need to construct a storage system or develop a highly effective energy redistribution method among distant areas. Despite these drawbacks, wind and solar power are often regarded as the only viable green energy supply options for the near future, owing to the abundance of source materials.

Introduction

Solar power is the most successful contender among the diverse types of renewable energy sources due to the huge amount of energy it supplies to the planet and the quantity of it. The sun can provide heat and light to the planet, both of which have various uses in our everyday lives.

Manufacturing solar cells might contribute to long-term economic development, and sunlight is often considered the most significant source of infinite clean energy. Solar power has a theoretical capacity of 90,000 TW, but this thermotical potential is based on the assumption that all the sun's rays can be turned into useful power and that the whole surface of the earth can be put to use in the process of converting solar energy, neither of which are realistic possibilities.[3]

If just 20% of the sunlight is converted into usable energy, we would need to cover 890 thousand km^2, or 0.17% of the Earth, to fulfill world energy demand. It is possible to drastically cut down on the amount of land needed for solar panels via building-integrated photovoltaics (PVs) and installing solar panels on the roofs of business and residential buildings. In 2050, the amount of solar energy contributing to the overall quantity of power produced in the United States is about 22%.[4] The Energy Information Administration forecasts that during the next quarter century, renewable energy sources like solar and wind will account for around fifty percent of the additions to the world's energy capacity. This illustrates both the possibility of using solar as a substitute source of energy as well as the economic drive to transform sunshine into electricity that can be used. Photovoltaics (PV) are quiet, off-grid, and low-maintenance, making them perfect for distant locations and transportable applications. Thus, solar power PV technology has garnered attention as a potentially more secure sustainable energy source and is the fastest growing generating technology, expanding at roughly 40% annually for the previous two decades.[5]

1.1.3 Photovoltaic Technology and Solar Cells

The word "photovoltaic" is used to define any device or system that is capable of converting energy from light into electricity. The conversion of light energy to electricity is called the photovoltaic effect, which was discovered by French physicist Edmond Becquerel in 1839.[6] After the invention of silicon solar cells based on p-n junctions in 1954, the photovoltaic effect was significantly utilized.[7] In 1956, MW photovoltaic modules were introduced, and since then, photovoltaic technology has been widely used to make clean energy that has less of an effect on the environment. However, photovoltaic devices were not commercialized because of their

Introduction

high cost and high level of complexity during production. In the 1960s, thanks to space program research, the basic mechanism of photovoltaics was created, significantly increasing performance and cost-effectiveness. As the cost of fossil fuels continued to rise, the researcher started investigating photovoltaic technology as a potential solution. In the present century, both the efficiency of solar panels and government help for technology has increased. In the recent decade, the use of solar energy has risen, becoming a worldwide phenomenon and a real and trustworthy source of power.

To meet the energy demand, photovoltaic technology has grown quickly and is considered the future energy hub. The term photovoltaic only makes sense when talking about turning solar energy into electricity since sunlight is the most important green and free energy source. **Figure 1-1** shows that photovoltaic devices could be divided into three generations based on the materials used and the ways they are made. Silicon solar cells, like polycrystalline silicon solar cells and monocrystalline silicon solar cells, are the first generation of photovoltaics. Silicon solar cell modules have been used in real life for a long time. But there are a few big problems with the first generation of solar cells, such as high fabrication temperature and pressure. Thin film semiconductor solar cells are often referred to as second-generation photovoltaics. The semiconductor materials of second-generation solar cells often exhibit straight bandgaps, allowing for a much thinner layer to achieve a greater light absorption rate, which is a key distinction between first and second-generation solar cells.[8] Copper indium gallium selenide (CIGS) solar cells, copper zinc tin sulfide (CZTS) solar cells, gallium arsenide (GaAs) solar cells, etc., are all examples of second-generation photovoltaics. But there isn't a lot of gallium available as a raw material, especially when large-scale industrial production and deposition are taken into account. Even worse, the arsenide compound is poisonous. GaAs solar cells couldn't be used as much because they were toxic. Moreover, second-generation solar cells are still expensive because they need sophisticated fabrication technology. Organic photovoltaics, quantum dot solar cells (QD), dye-sensitized solar cells (DSSC), and perovskite solar cells are all types of third-generation solar cells (PSC). The DSSC fabrication process is easy and uses low-cost raw materials. In a short time, PSCs showed a rapid increase in PCE and became a competitor to silicon solar cells on the market. Even though PSCs have a higher PCE, they have some drawbacks, like the toxicity of Pb and lower reproducibility and stability. Based on the most recent progress in PSCs, this study aims to investigate the suitable fabrication conditions for higher crystalline films

by molarity, annealing temperature, and additive engineering. By this time, the interfacial layer was introduced for enhanced reproducibility and stability.
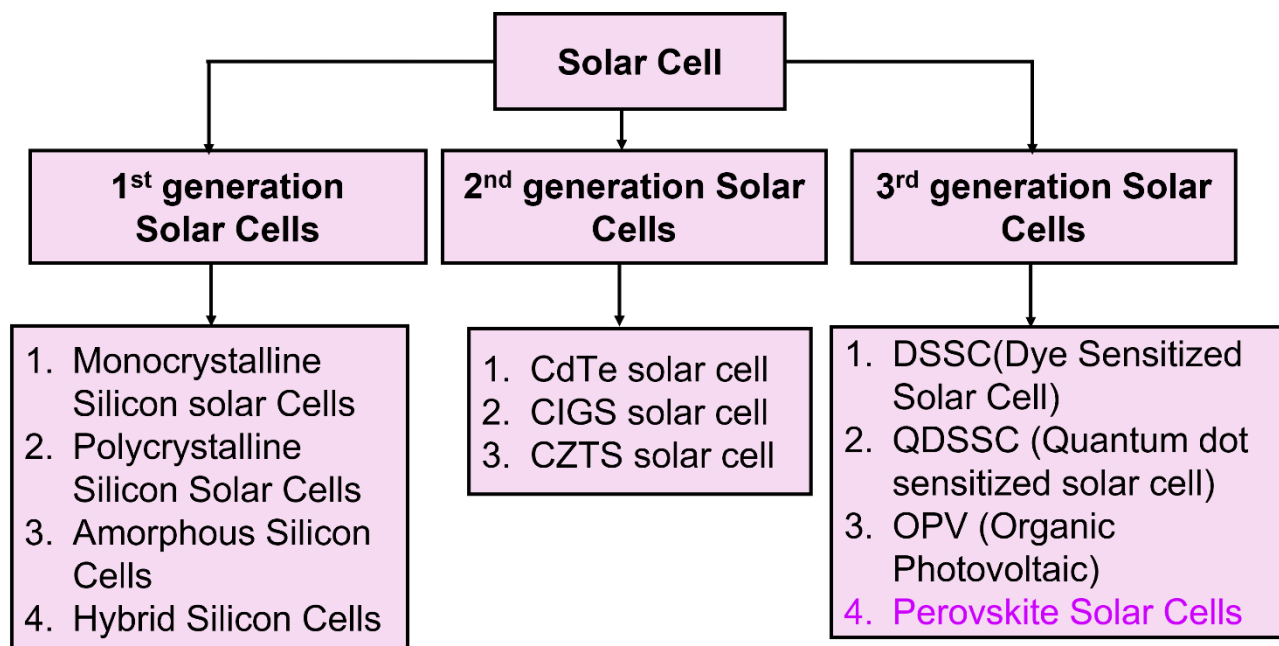
Figure 1-1. Solar cells generation.[9]

1.2 Perovskite Solar Cells

1.2.1 Properties of Perovskite Materials

Perovskite solar cells are solar cells that use perovskite materials as an absorber or active layer in solar cell operation. Prof. Miyasaka was the first person to use perovskite as a sensitizer in DSSC in 2009. Since its introduction to the research community, the PSC has been capable of attaching many researchers due to its excellent electrical and optical properties for photovoltaic applications. The following section will discuss the properties of perovskite materials in detail.

In 1839, Gustav Rose discovered the first perovskite mineral, $CaTiO_3$, which was named after Russian mineralogist Lev Perovskite.[10] Any substance with the generic formula ABX_3, where A site is a monovalent inorganic or organic cation ($CH_3NH_3^+$ or $NH_2CHNH_2^+$ or Cs^+), B represents the divalent metal cations (Pb^{2+}or Sn^{2+}or Bi^{2+}), and X represents an anion (Cl^-, Br^- or I^-), is considered to have a perovskite structure, as shown in **Figure 1-2**. Here, the $[BX_6]^{4-}$ octahedrons share a corner of space in three dimensions.

According to theoretical analysis, there are two parameters such as tolerance factor (t) and octahedral

Introduction

Figure 1-2. Scheme of the structure of perovskite materials.[11]

factor (μ), that need to be a consideration for a stable perovskite structure. The t and μ can be calculated by using the following equations.[12]

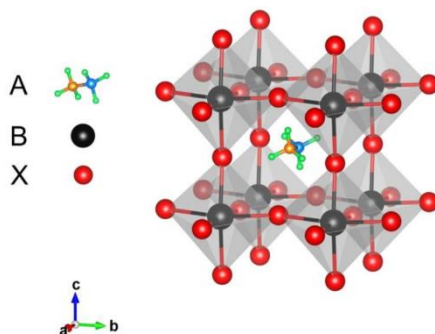$$\text{Tolerance factor, } t = \frac{(rA+rX)}{\sqrt{2}\,(rM+rX)}$$

$$\text{Octahedral factor, } \mu = \frac{rM}{rX}$$

Where rA, rM, and rX are the ionic radii of the monovalent cation, divalent metal, and halide anion, respectively, on the perovskite formula ABX_3. To produce a stable perovskite structure, the tolerance factor (t) must be between 0.81 and 1.11, whereas the octahedral factor (μ) must be between 0.44 and 0.90.

A common characteristic of perovskite materials is a high absorption coefficient. For instance, at wavelengths below 600 nm, $CH_3NH_3PbI_3$ ($MAPbI_3$) has an absorption value of $10^4 \sim 10^5$ cm^{-1}. This value is higher than the silicon solar materials.[13, 14] Compared to more common semiconductors like GaAs, CdTe, or Cu (In, Ga) Se$_2$, the optical absorption coefficient of $MAPbI_3$ is either greater or on par with it (CIGS).[13] Thin layers of perovskite may absorb a lot of light because of their high absorption coefficient. For optimal solar performance, a thinner film with fewer defects and less charge recombination is crucial.[15, 16] The produced carriers will be recombined if the absorber's thickness is greater than the diffusion length, preventing them from entering the electron transport layer (ETL) or the hole transport layer (HTL).

When a photon with an energy more than or equal to the bandgap energy is absorbed by a semiconductor, a quasiparticle called an exciton is formed. When light creates an electron-hole pair, the pair is held together by the attractive Coulomb attraction. Perovskite material's weak interaction allows excitons to freely flow throughout the crystal. For instance, the exciton binding energy of $CH_3NH_3PbI_3$ ranges from 15 to 34 meV at

low temperatures to from 5 to 29 meV at ambient temperature.[17] Energy loss may be minimized by lowering the exciton binding energy.

The carrier diffusion length in solution-process organic-inorganic perovskites is 500 nm-800 nm, which is orders of magnitude larger than in organic semiconductors (~10 nm).[18] One of the most crucial parameters for effective charge transfer in solar applications is the carrier diffusion length. A greater absorber layer thickness may be achieved with a longer diffusion length without compromising charge recombination and collection. According to the following equation, the diffusion length (L_D) is correlated to the lifetime (τ) and mobility (μ) of charge carriers.

$$\text{Diffusion length, } L_D = \sqrt{(K_B T \mu \tau)}/e$$

Where K_B, T, and e are the Boltzmann constant, temperature, and elementary charge, respectively. The crystallinity, morphology, and defects type effect above mentioned parameters.

Even though perovskite is a natural semiconductor, its behaviour is usually either p-type or n-type, depending on how it is made. For example, if Sn-based perovskite is made in a reducing environment, it becomes an n-type semiconductor. On the other hand, if it is made in an oxidizing environment, it acts like a p-type semiconductor. But in general, p-type behaviour is seen in both Sn-based and Bi-based perovskites.

1.2.2   Perovskite Solar Cells Structure and Working Mechanism

The initial structure of PSCs is based on that of DSSCs, and perovskites ($(CH_3NH_3)^+PbI_3$) are employed as sensitizers rather than Ru complexes, with a 3.8% conversion efficiency.[19] The perovskite layer as an absorber is mainly sandwiched between the ETL and the HTL to generate holes and electrons, and those carriers are collected by respective transport layers in solar cells configuration. Based on the use of the transport layer, the PSCs structure can be divided into three categories, as shown in **Figure 1-3.**

(a) **(b)** **(c)**

Au	Au or Ag	Ag or Al
HTL	HTL	ETL
Perovskite		Perovskite
mp-TiO₂	Perovskite	
ETL	ETL	HTL
TCO	TCO	TCO

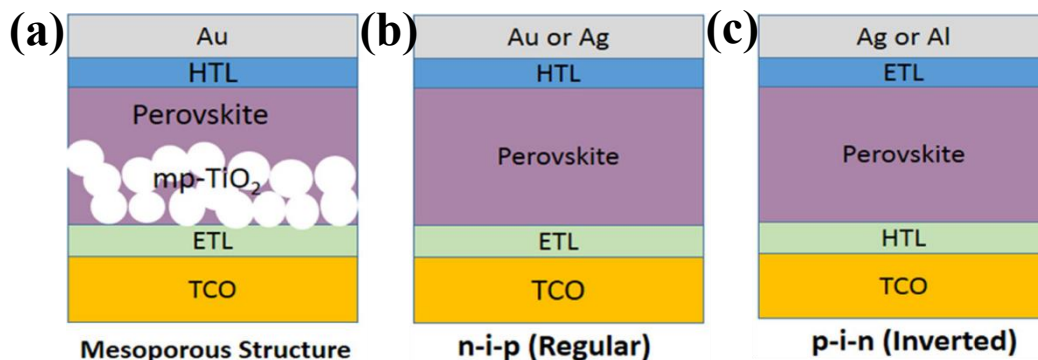| **Mesoporous Structure** | **n-i-p (Regular)** | **p-i-n (Inverted)** |

Figure 1-3. Illustrations of the three kinds of PSC architecture. (a) n-i-p mesoporous structure. (b) n-i-p planer structure. (c) p-i-n planer structure.[20]

The general operating concept of PSCs consists of photon absorption, charge separation, and charge transportation. When a light source is directed towards a perovskite material, an exciton is formed as a result of an electron moving from the valence band to the conduction band (i.e., electron-hole pair). Due to the low excitonic binding energy of perovskites (i.e., 4-22 meV for $CH_3NH_3PbI_3$), excitons in these materials dissociate into free holes and electrons at ambient temperature, allowing them to move freely throughout the device. The electrons and holes move across the perovskite and are collected by the respective transport layer. It is crucial to select the ETL and HTL that match the energy levels of the perovskites conduction band (CB) and valence band (VB) level that guarantees efficient carrier transportation. To do this, the most important thing is to choose ETL or HTL with energy levels that match those of perovskite. For a good HTL to work well in photovoltaics, its conduction band or lowest unoccupied molecular orbital should be much higher than that of perovskite. At the same time, the highest occupied molecular orbital, or valence band, of HTL should be right above the valence band of perovskite. For the ETL, the opposite specifications are needed. This charge selectivity property is important for how well the device works because if an electron goes to the wrong electrode, it will combine with one of the many holes there without giving off any radiation. Photogenerated charges are lost because of this process. The schematic illustration of the inverter planer PSC is shown in **Figure 1-4**. Recombination of charges by non-radiative recombination happens at the grain boundaries and interface that converts the photogenerated charge into heat. By controlling the defects, the unwanted losses of photogenerated carriers could be minimized.
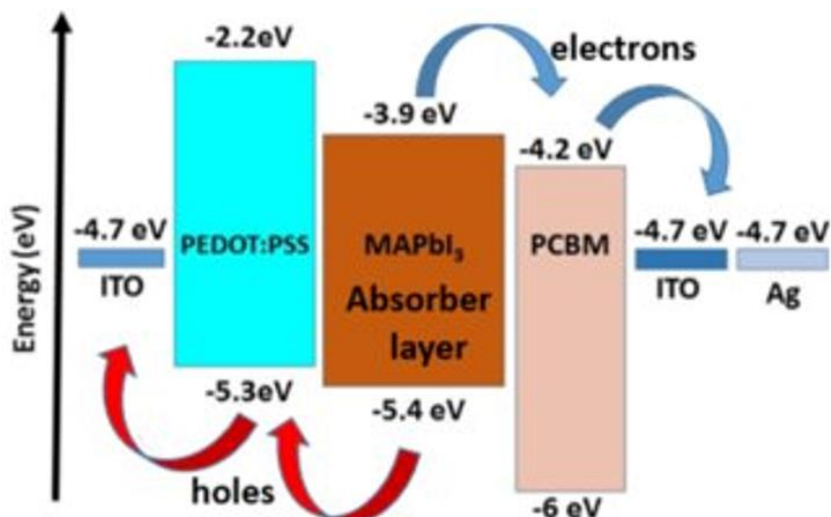
Figure 1-4. Schematic illustration of working principle of PSC for inverted planar (ITO/HTL/perovskite/ETL/metal electrode) structure with energy diagram.[21]

1.3 Lead-Halide Perovskite

Many research groups are interested in hybrid organic–inorganic perovskites (HOIPs) as possible semiconductive materials because they are easy to fabricate and have good optoelectronic properties for photovoltaic applications. Perovskite materials can be used as absorbers in perovskite solar cells because they have a high absorption coefficient, a bandgap that can be tuned, and a low processing temperature (PSCs). In the 12 years since it was first used in 2009, conventional PSCs based on lead (Pb) have reached a power conversion efficiency (PCE) of over 25% on the lab scale.[22] Studies aimed to optimize the Pb halide perovskite layer's stability, deposition, device layout, interface engineering with neighbouring semiconductor layers, and high-throughput fabrication techniques in preparation for commercialization.

1.3.1 Lead-Halide Perovskites Issues

In spite of the many exciting benefits and recent developments, lead-based solar cells still have several significant issues. The toxicity of the Pb^{2+} cation, as well as the pollution that is created by the loss of lead from the perovskite solar cell module are two of the most significant issues. In addition, the deployment of Pb-based PSCs in real life is effectively hindered owing to the prohibition of utilizing a large quantity of dangerous Pb in industrial production. This restriction was put in place to protect humans from the harmful effects of Pb. Scientists found that exposure to Pb^{2+} cation has negative effects on both the human neurological system and the reproductive system.[23] High concentrate Pb^{2+} cations would be produced if lead perovskites were degraded

in a humid environment or by intense UV light.

Even though careful encapsulation can keep the lead loss to a small amount, the lead perovskite degradation is usually irreversible. Perovskite photovoltaics are most destroyed by moisture and high temperatures. The results of a study showed that hybrid lead perovskite materials break down quickly when there is a lot of water or when the temperature is high (over 140 ℃).[24] These breakdowns often happen at the defect sites at the interfaces. When there is a lot of oxygen around, UV light can speed up the movement of oxygen molecules through the perovskite layer.

The U.S. EPA says that the most Pb^{2+} that can be in the air and water is 0.15 g L^{-1} and 15 g L^{-1}, respectively.[25] Perovskites degrade into PbI_2, which has a higher solubility (K_{sp}) than the toxic Cd^{2+} in CdTe solar cells, which has a K_{sp} on the order of 1x 10^{-22}.[26] This makes PSCs fabricated from lead more dangerous than CdTe solar cells. Perovskite is easily dissolved in water, which means it could leak into the environment through rain and have a big effect on the environment and nature around us. With the risk that PSCs could release a lot of Pb into the environment, it is important to replace the toxic Pb in PSCs with non-toxic materials before commercialization. **Figure 1-5** represents the toxic effect of Pb on the environment and human body.
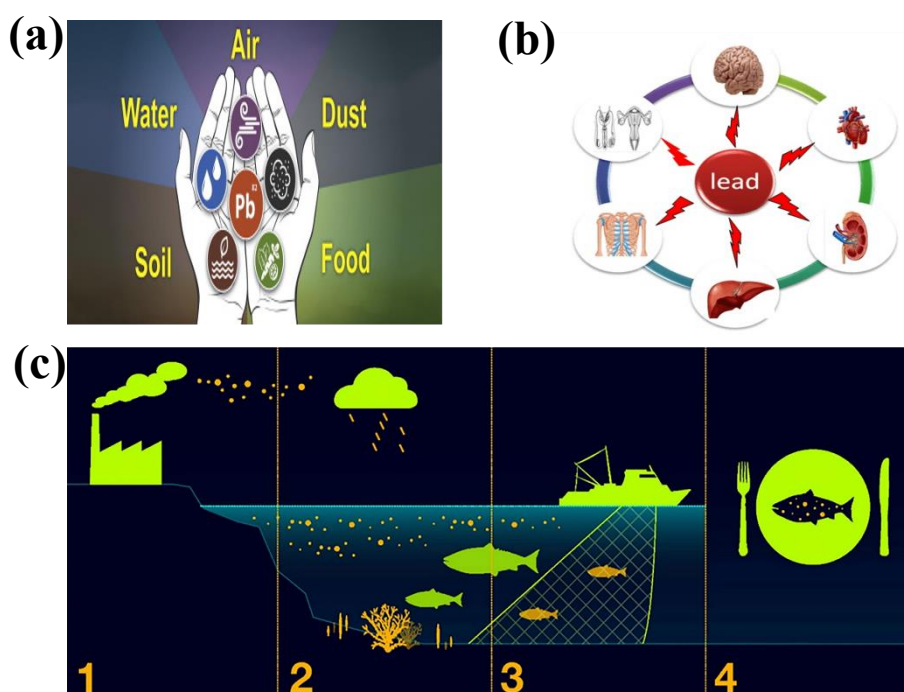

Figure 1-5. (a) Environment pollution by Pb. (b) Toxicity of Pb in human body. (c) Risk of Pb-based PSCs for food chain.[27]

Introduction

1.4 Non-Toxic Elements to Substitute Pb in Perovskite Solar Cells

Numerous research efforts have been made to address the aforementioned concerns. Good encapsulation and cautious fabrication methods may often slow or stop the degradation of a solar cell. It is true that these issues are unsolvable. Developing effective lead-free perovskites to replace those containing lead in halide perovskites seems like the most likely way to proceed.

Many potential replacement components have been studied up to now. Bismuth (Bi), a member of the VA group of the periodic table, has been investigated as a substitute element of Pb. Fortunately, Bi^{3+} and Pb^{2+} have the same electronic configuration ([Xe] $4f^{14}5d^{10}6s^26p^0$) and have relatively comparable ionic radii.[28] Experiments and theoretical modeling have shown that bismuth perovskites have a high defect tolerance, a long carrier lifetime, and a low defect state density. Bismuth has been shown to be much less toxic than lead. However, bismuth perovskite has shown several significant issues. As a result of forming a 2D hexagonal layered structure, bismuth perovskite would have some intrinsic defects.[29] Furthermore, bismuth perovskite has a larger (~2.0 eV) and indirect bandgap which ensures the lower performance of the solar cells.[30] Another important problem of bismuth perovskite is lower electron mobility compared to Pb perovskite.[31]

As an alternative to Pb^{2+}, tin (II) has been considered in PSCs applications. Sn-based halide perovskites have structural similarities with Pb-based perovskites, and both may produce compounds with +2 valence. In addition to having almost the same atomic radius, Pb and Sn have the same outer shell orbitals that are not being used. Due to the similarities between Pb and Sn, it is easier to replace Pb with Sn without changing the excellent optoelectronic properties. Because of their optimal band gap in the spectrum of 1.1 eV to 1.4 eV, Sn-based PSCs have theoretical limitations of about 32.91%, which is greater than Pb-based PSCs (30.14%).[32] In contrast, the limitations of Sn-based perovskites were revealed. Instability has been observed for Sn^{2+} cations. The 3D perovskite quickly reduces to 2D or even decomposes when exposed to moisture or any oxidizing agent since Sn^{2+} is rapidly oxidized into Sn^{4+}.

1.5 General Introduction

Perovskites containing lead (Pb) halide have attained a significant amount of attention since it was introduced.[33] The efficiency has swiftly eclipsed that of all third-generation photovoltaics (PVs), reaching a

Introduction

PCE of over 25% in a decade.[34] Methylammonium lead iodide (MAPbI$_3$) is the compound that has received the most attention from researchers because it possesses an impressive combination of material properties. These material properties include a suitable bandgap, long diffusion length of charge carrier, a high absorption coefficient, and a high tolerance for defects, and they can be made in the solution process.[35-39] Due to the suitable optoelectronic properties, Pb halide perovskites are an exciting photovoltaic technology for making high-performance solar cells at low cost.[40, 41] Also, Pb halide perovskites have a bandgap that can be changed, which lets this material be used in different optoelectronic devices like LEDs, lasers, and photodetectors.[42-45]

The toxicity and the inherent instability of lead halide perovskites are the two primary factors that hinder the widespread commercialization of lead halide perovskites.[46, 47] Even though careful encapsulation can keep the lead loss to a small amount, the lead perovskite degradation is usually irreversible. The decomposition happens faster when there is water, heat, and light.[48, 49] When the material decomposes, it turns into water-soluble Pb halides, which are hazardous to the environment because they can pollute water sources.[50]

It is important to replace or lower the quantity of Pb in PSCs while maintaining optoelectronic properties. Recently, for photovoltaic applications, studies have been conducted to identify Pb-free materials with suitable optoelectronic properties. The emphasis is increasingly shifting toward discovering and developing low-toxic and stable materials for widespread use. Therefore, bismuth (Bi), a member of the VA group of the periodic table, has been investigated as a substitute element of Pb. Fortunately, Bi^{3+} and Pb^{2+} have the same electronic configuration ([Xe] $4f^{14}5d^{10}6s^26p^0$) and have relatively comparable ionic radii.[28] Although Bi-PSCs have a lower PCE until now but in terms of stability promise aspiring results initially.[51] Among all Bi-based absorbers, A$_3$Bi$_2$I$_9$ (A = MA, FA, and Cs) has attracted considerable attention. However, because of the poor morphology of the fabricated thin films, the performance of A$_3$Bi$_2$I$_9$-PSC remains challenging. Fengzhu *et al.* used a cation displacement approach to fabricate MA$_3$Bi$_2$I$_9$ perovskite films with a PCE of 0.33%.[52] Park *et al.* used a one-step spin-coating process to incorporate two distinct cations, Cs and MA, in A$_3$Bi$_2$I$_9$-PSC and achieved a PCE of >1%.[53] However, the lower PCE could be attributed to the inferior surface morphology and wider bandgap (2.03 eV).[54] CsBi$_3$I$_{10}$ (CBI) might be a possible solution in the Bi-PSCs community. CBI has a suitable bandgap of 1.77 eV and an absorption coefficient of 1.4×10^5 cm^{-1}, which is comparable to the Pb-based perovskite in the absorption spectrum ranging from 350 nm to 500 nm. Unfortunately, few studies have been conducted on

Introduction

the CBI perovskite because of the lack of reproducibility. Previously, Johansson *et al.* performed a one-step spin-coating technique to deposit CBI on top of mesoporous TiO_2 and achieved a PCE of 0.40%; however, their fabricated CBI layer had multiple pinholes.[55] Then, the same group used a two-step recrystallization method with 4-tert-butylpyridine to improve the crystal size.[56] Liang *et al.* used a solvent annealing process, and the fabricated PSCs exhibited decay under ambient conditions even for 10 days.[57] Although the stability of CBI-PSCs may be promising, the CBI-PSCs performance remains low. In our previous study, we examined CBI-PSCs using various solvent and anti-solvent techniques to improve the surface morphology of the CBI perovskite with a PCE of 0.63%.[58] Then, we focused on determining the impact of different hole transport layers on fabricating highly crystalline CBI films.[59] During those investigations, we observed that the reproducibility of Bi PSCs is significantly lower than that of Pb-PSCs and Sn-PSCs. Lower reproducibility can be explained by two factors: (i) crystal defects and lower surface coverage and (ii) weaker interfacial contact in the perovskite/electron transport layer (ETL). Lower crystallinity generates pinholes that remain inside the crystal, thus resulting in short-circuit of the overall PSC because of the direct contact between ETL and HTL through the pinholes of the Bi-perovskite. Collectively, crystal defects and weaker interface contact at the Bi-perovskite/ETL remain a critical issue for the limited photovoltaic performance and low reproducibility of the respective PSCs.[60]

As per the Gibbs–Thomson effect and thermodynamic theory, the concentration (molarity) of the precursor solution and annealing temperature affect the crystallization of the film during the fabrication process.[61, 62] The precursor solution concentration assists in the crystal size regulation by lowering the crystal curvature as crystal size increases. Fortunately, the appropriate solution concentration gradients assist in the reduction of small particles by diffusing the growth direction to the largest particles, resulting in the appearance of larger particles. However, a suitable post-annealing temperature generates the appropriate inter-atomic energy for the crystal with homogeneous nucleation. Furthermore, the appropriate energy of the crystal assists in the crystal's growth in the same direction and produces a larger crystal. Another performance-limiting factor is the weaker interface contact at perovskite/ETL or perovskite/HTL. The weaker interfacial contact reduced the carrier transportation to ETL or HTL or both layers and was responsible for charge accumulation. However, a few attempts have been made to improve the interface contact of CBI perovskite/ETL or CBI perovskite/HTL.

Introduction

We fabricated CBI perovskite thin films under different fabrication conditions (by varying the molarity and temperature) and optimized the suitable fabrication condition. Furthermore, we introduced the bathocuproine (BCP) interfacial layer (BIL) at the perovskite/ETL interface as a structural modification engineering of the respective PSC with the configuration of ITO/PEDOT: PSS/CBI/BCP/C$_{60}$/BCP/Ag. The wider bandgap n-type semiconductor BCP can improve the electrical interface contact of the perovskite/ETL interface, thus limiting the possibility of hole leakage to the ETL from the HTL and improving overall PSC performance. In this study, the modified structure with a 6 nm-sized BIL in the perovskite/ETL interface of the PSC demonstrated a maximum PCE of 0.80%. Furthermore, the good reproducibility of photovoltaic performance has been observed for PSCs with BIL at the perovskite/ETL interface, which is a promising result for developing CBI-based PSCs. The best-performing PSC with a 6-nm-sized BIL demonstrated long-term air stability and retained ~90% of its initial PCE even after 528 h.

Although Bi-perovskite has many suitable properties which are comparable to Pb-perovskite, in terms of PSCs performance, Bi-PSCs are far behind from Pb-PSCs. Due to the poor crystallinity and higher band gap of Bi-perovskite, the PCE of Bi-PSCs is lower than that of Pb-PSCs. Fortunately, tin (Sn) belongs to group IV in the periodic table and is a promising candidate for a non-toxic divalent metal cation as an alternative to Pb. The Sn-based perovskite has higher charge carrier mobility, a lower exciton binding energy, and a slightly smaller radius than Pb^{2+}.[63] Moreover, Sn perovskite could have a band gap between 1.1 and 1.4 eV, and it could reach the highest efficiency of 33.7% at 1.34 eV according to the Shockley-Queisser limit.[64, 32] Although Sn-PSCs have achieved PCE of over 14%, the performance of Sn-PSCs is still lower than Pb-PSCs due to some chemical constraints.[65] The performance limiting factors have been associated with the notorious oxidation of Sn^{2+} to Sn^{4+} of the Sn perovskite absorber during the fabrication process and anionic vacancies (I$^-$ losses), which lead to severe defects in Sn-perovskite. In addition, the fast crystallization during the spin-coated process forms inferior-quality films with small grain sizes, pinholes, and incomplete coverage. These problems collectively generate electronic defects which induce trap-assisted nonradiative recombination resulting in low PCE.

Moreover, Sn-PSCs are subjected to a more serious energy level mismatch with the frequently used carrier transport layers.[66] This mismatch is responsible for the nonradiative recombination center at the

Introduction

perovskite/transport layer interface, leading to the loss of V_{OC}. The V_{OC} loss called V_{OC} deficit is defined as E_g/q - V_{OC}, where E_g is the optical band gap, and q is the elementary charge.[67] In an attempt to reduce the nonradiative recombination and trap density of the tin perovskite films and improve the V_{OC} and stability of the respective Sn-PSC, several surface passivator agents have been adopted.[68] Meanwhile, Lewis acid or Lewis base molecules and inorganic or organic salts have been used as passivation agents.[69] In the fabricated perovskite films, the positive or negative charge defects may present simultaneously. Commonly used Lewis acid/base molecules could passivate only positively or negatively charged defects.[70] On the other hand, inorganic or organic salts have been considered promising due to the ability of cationic and anionic defects passivated together. Recently, we have adopted a Lewis base molecule diaminomaleonitrile (DAMN) with a cyano group, reduced the electron losses at the perovskite/ETL interface, and improved the V_{OC} of an Sn-PSC.[71] Islam et al. showed that N_2H_5Cl, as a co-additive with amino and Cl^- groups, could retard the rapid crystallization process and improve the PSC performance.[72] Diau et al. revealed that the introduction of ethylenediammonium diiodide (EDAI$_2$) regulated the formation of the FASnI$_3$ film and successfully passivated the surface defects.[73] Our group recently introduced hydroxylamine hydrochloride (HAHc) salt with the functional group hydroxyl and anion Cl^-, which efficiently reduced the electronic defects of the tin perovskite film and resulted in an improved V_{OC} of the respective PSC.[74] Abate et al. introduced ionic liquid n-butylammonium acetate (BAAc) to the perovskite precursor solution and controlled the perovskite crystallization by the N-H$\cdots$X hydrogen bonds and solid O$\cdots$Sn bonds through interactions between the BAAc and perovskite precursors.[75] Recently, 2-guanidinoacetic acid (GAA) has been used to passivate the Sn-related and I-related defects, improve the structural toughness, and promote the carrier transport of Sn perovskites.[76] An additional study has shown that bulky cations such as butylammonium (BA$^+$), phenylethylammonium (PEA$^+$), 5-ammoniumvaleric acid (5-AVA$^+$) with the functional group -NH$_3^+$, and guanidinium (GA$^+$) with the functional group -NH$_2$ can passivate defects, tune the energy levels of the respective perovskite layer, and improve the V_{OC} of the Sn-PSC.[77-80] When nonpolar GA$^+$ was incorporated into a perovskite composition of formamidinium tin triiodide (FASnI$_3$), the V_{OC} of the respective PSC was enhanced significantly by mitigating the surface defects.[78] In earlier work, Hu et al. introduced a guanidine-based additive, aminoguanidine hydrochloride (NH$_2$GACl), as an additive into a precursor solution of Sn-

Introduction

based perovskite and achieved a V_{OC} of 0.54 V with PCE of 7.3%.[81] Yao et al. introduced the 1,3-diaminoguanidine monohydrochloride (DAGCl) into the Pb-based perovskite precursor solution for a two-step fabrication process.[82] Surprisingly, other than lead-based PSCs, no one has used DAGCl for Sn-based PSCs in a one-step solution process. So, it is important to find out the feasible approach to passivate the defects of Sn-based perovskite films and improve the Sn-PSC device performance with the addition of the DAGCl additive.

The effective electronic defect passivation of FASnI$_3$ perovskite has been achieved by adding an optimized concentration of the guanidine-based additive DAGCl in the perovskite precursor solution. The multiple polar hydrogen groups ($N^{\delta-}-H^{\delta+}$) of DAGCl and the electronegative iodide ion ($I^{\delta-}$) could form strong hydrogen bonding (-NH$\cdots I^-$) in the perovskite framework and suppress the loss of I^-. Additionally, the Cl^- ion may be coordinated with the undercoordinated Sn^{2+} in the perovskite structure, stabilizing the perovskite framework and retarding the oxidation of Sn^{2+}. This dual function of the DAGCl additive helps to form compact and uniform films and enhance the crystallinity of the respective perovskite film. We revealed that incorporating DAGCl in perovskite films successfully passivated the electronic defect, enhanced the carrier lifetimes, and improved the V_{OC} of PSCs. As a result, the optimized DAGCl (3 mol %) in PSCs showed a PCE of 8.92% with a high V_{OC} of 0.61 V and an enhancement of $\approx$110 mV from the pristine PSC (0.50 V). Additionally, DAGCl-modified PSCs demonstrate excellent light-soaking stability under simulated AM 1.5G (100 mWcm^{-2}) at the maximum power point tracking (MPPT) conditions in ambient conditions (room temperature, humidity ~34%) and keep 95% of the initial PCE after being stored in an N$_2$ glovebox for 1100 h with encapsulation.

However, we improved the PCE of FASnI$_3$ PSC after modifications, but there is still a disparity in efficiency, reproducibility, and stability between tin-based PSCs and lead-based PSCs. We focused on the root of defects which is the properties of the perovskite precursor solution. Because all research mainly focused on the reduction of Sn^{2+} oxidation and suppression of bulk defects of fabricated perovskite films.

To prepare the FASnI$_3$ perovskite precursor solution, traditional dimethyl sulfoxide (DMSO) is used as a solvent, and it is responsible for the irreversible oxidation of Sn^{2+} in the precursor solution even in the glovebox with very less amount of oxygen.[83] In addition to this, during the annealing process, the I ions (I^-) can easily be volatilized and reduce the fabricated film quality.[84] Gao et al. reported that SnI$_2$ was dissociated in solvent,

and I^- ions were oxidized in addition to Sn^{2+}.[85] They found that Sn^{2+} oxidation generated from the dissociation of SnI_2. The oxidation of Sn^{2+} and I^- in precursor solution directly hampered the stoichiometric ratio of the fabricated films and damaged the film's quality. Many research groups claimed that the devices performance from various research facilities is difficult to reproduce, sometimes even by the same individual, due to the properties of the precursor solution.[86] PSCs performances are very much sensitive to precursor solutions properties. Given its relevance, precursor solution properties have received less research interest than perovskite solar device stability in the last decade.

Here, we report a low-cost multifunctional molecule, 4-fluorophenylhydrazine hydrochloride (4F-PHCl), in perovskite precursor solution to enhance the PCE and stability of $FASnI_3$-PSCs. The hydrazine functional ($-NH-NH_2$) group in 4F-PHCl additive can effectively I_2 defects back to I^-, which inhibits the formation of I_2 and generation of free Sn^{2+} ions in precursor solution and effectively suppresses the Sn^{2+} oxidation. In addition, large organic cation $4F-PH^+$ ions are successfully incorporated into the crystal lattice without any dimensionality reduction of 3D perovskite crystals. Because of these multifunction effect, the 4F-PHCl-modified PSC showed a PCE of 10.86 %. Most importantly, the encapsulated PSC maintained 92 % of the initial PCE upon storing in the N_2-filled glovebox over 80 days. The incorporation of a hydrophobic fluorinated benzene ring in Sn-perovskite enhanced the moisture stability of the fabricated films and devices. Overall, this work provides an in-depth insight into the properties of perovskite precursor solutions for fabricated high-quality films and promoting highly efficient and stable Sn-PSCs.

1.6   Aim of this Thesis

Lead-based perovskite photovoltaics have emerged as the most promising third-generation solar cells since it was introduced in 2009. However, the commercialization of perovskite solar cells faces challenges due to the toxic element of Pb in PSCs. After fully replacing the Pb element with Bi and Sn, other challenges arise for the research community. Bi-perovskite has a lower quality of crystallinity, and in the case of photovoltaic application, the reproducibility and stability are lower compared to Pb-PSCs. In Sn-perovskite, the most challenging is the fast crystallization process during the fabrication process. Another challenging issue for Sn-perovskite is the easy oxidation of Sn^{2+} and I^- ions and reduced stability, as well as the performance of the solar cells.

Introduction

Considering the challenges mentioned above for Pb-free PSCs, this thesis aims to develop the fabrication process of Bi-PSC with higher reproducibility and stability. In the case of Sn-PSCs, we controlled the crystallization process and suppressed the Sn^{2+} oxidation and I^- ions losses in the final films. Also, we focused on the origin of Sn^{2+} during the fabrication process and successfully controlled the Sn^{2+} and I^- ions oxidation in the precursor solution.

In Chapter 3.1, I discussed the suitable fabrication conditions of $CsBi_3I_{10}$ thin films to develop the films' quality and reduce the weaker interfacial contact in the perovskite/electron transport layer (ETL) interface. I have introduced the bathocuproine (BCP) interfacial layer (BIL) at the perovskite/ETL interface for the first time in Bi-PSCs and improved the reproducibility and stability as well as PCE.

In Chapter 3.2, I have focused on the most challenging issues of Sn-PSCs. I have used an additive engineering process to suppress the Sn^{2+} oxidation and I^- losses in Sn perovskite films by introducing the 1,3-diaminoguanidine monohydrochloride (DAGCl) additive in the $FASnI_3$ perovskite precursor solution. The interaction between the DAG^+ ion of DAGCl and the iodide ion (I^-) of SnI_2 formed hydrogen bonding and suppressed the I^- loss of the perovskite framework. Moreover, the Cl^- ion formed co-ordination with undercoordinated Sn^{2+} ions and stabilized the $FASnI_3$ perovskite structure with effective suppression of oxidation of Sn^{2+} to Sn^{4+}. Suppressing the oxidation of Sn^{2+} and loss of I^- guaranteed a better Sn^{2+}/I^- stoichiometric ratio and showed a PCE of 8.92%.

In Chapter 3.3, I have focused on the root of Sn^{2+} and I^- ions oxidation in the $FASnI_3$ perovskite precursor solution and introduced the possible approach to solve this problem by 4-fluorophenylhydrazine hydrochloride (4F-PHCl) additive. Interestingly, $4F-PH^+$ was incorporated into the $FASnI_3$ perovskite crystal lattice. Moreover, the hydrazine group of 4F-PHCl effectively reduced I_2 or I_3^- defects back to I^- and suppressed the Sn^{2+} oxidation. Those positive effects of the 4F-PHCl on perovskite films have shown improved PSCs performance and achieved a PCE of 10.86 %.

CHAPTER 2: EXPERIMENTAL SECTION

Experimental Section

2.1 Raw Materials

We used all chemicals as-received without any further purification, including Bismuth Iodide (III) (BiI$_3$) (Sigma Aldrich, 99%), Cesium Iodide (CsI) (Sigma Aldrich, 99.999%), Tin (II) iodide (SnI$_2$, 99.99%, Sigma–Aldrich), Formamidinium Iodide (FAI, > 98%, Tokyo Chemical Industry Co., Japan), Tin (II) Fluoride (SnF$_2$, >99%, Sigma-Aldrich), Ethylenediammonium Diiodide (EDAI$_2$) (Merck), 1,3-Diaminoguanidine Hydrochloride (DAGCl, > 98%, Tokyo Chemical Industry Co., Japan), 4-fluorophenylhydrazine Hydrochloride (4F-PHCl, > 97%, Tokyo Chemical Industry Co., Japan), poly(3,4-ethylenedioxythiophene)-polystyrene sulfonate (PEDOT:PSS) (Clevious P VP Al 4083), C$_{60}$ (99.5%, Lumtec Co., Taiwan). Bathocuproine (BCP), N,N-dimethylformamide (DMF, 99.8%), anhydrous dimethyl sulfoxide (DMSO, 99.8%), anhydrous chlorobenzene (CB, 99.8%), methanol, and ethanol, were purchased from Wako Co., Japan.

2.2 Adduct Preparation

The SnI$_2$- DAGCl or SnI$_2$-4F-PHCl adducts were prepared by mixing SnI$_2$ (298 mg) with DAGCl (7.53 mg) or 4F-PHCl (16.25 mg) in 1 ml of DMSO solvent. The solution was stirred for 2 hours. After that, the solution was kept overnight. The final precipitate was collected, washed with chlorobenzene, and dried under a vacuum.

2.3 Perovskite Solar Cells Fabrication Process

2.3.1 Fabrication Process of Bi-Based Solar Cells

2.3.1.1 Preparation of Bi-Perovskite films

CsI and BiI$_3$ were mixed at a molar ratio of 1:3, dissolved in a 7:3 volume ratio of DMF: DMSO solvent, and stirred overnight at 50 °C to create the precursor solution for the CsBi$_3$I$_{10}$ perovskite film. Spin-coating procedures were used to fabricate the CsBi$_3$I$_{10}$ thin films in two stages, the first lasting 12 seconds at 1000 rpm and the second 24 seconds at 5500 rpm. Annealing on a hot plate at 80 °C for 10 minutes, 100 °C for 10 minutes, 120 °C for 10 minutes, and 140 °C for 10 minutes was followed by anti-solvent dripping with 150 µl of chlorobenzene added in the last 10 seconds.
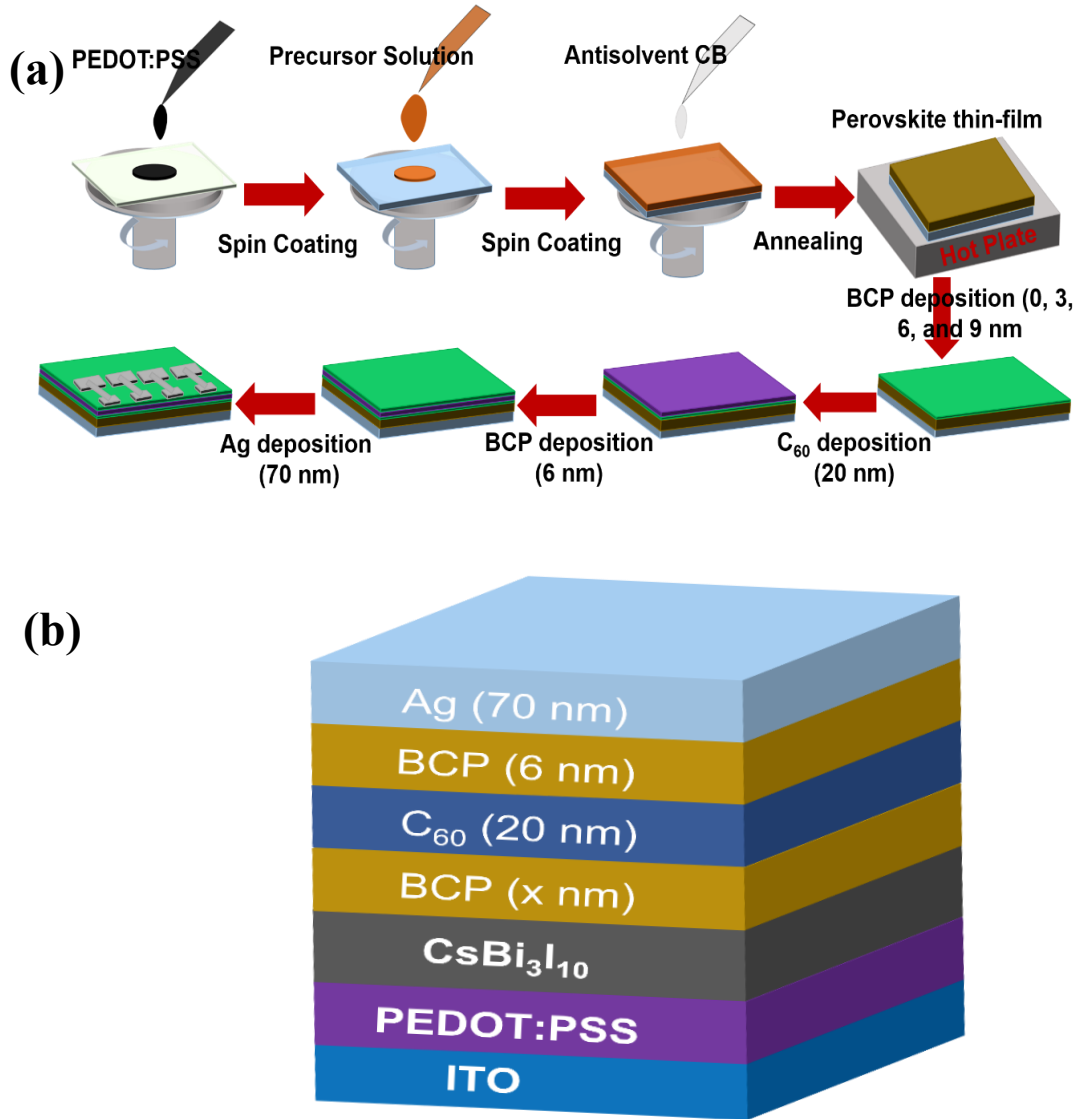
Figure 2-1. (a) The fabrication steps of Bi-based perovskite solar cells. (b) Fabricated Bi-PSC structure.

2.3.1.2   Solar Cells Fabrication

PSCs were fabricated on glass substrates coated with patterned indium tin oxide (ITO). Substrates were cleaned using deionized water, detergent, ethanol, and acetone in an ultrasonic cleaner. We used nitrogen gas to dry the glass substrates and then cleaned them with UV-Ozone for 30 minutes. To deposit the PEDOT: PSS on the ITO substrate, spin-coating methods were used twice, the first time at 1000 rpm for 10 seconds and the second time at 4000 rpm for 30 seconds. Afterward, the PEDOT: PSS films were annealed at 150 °C for 15 minutes before being cooled to room temperature. After the substrates cooled to room temperature, they were moved to the glove box where $CsBi_3I_{10}$ perovskite films were deposited. Next, we used thermal evaporation to deposit BCP

(X nm), C_{60} (20 nm), and BCP (6 nm). Finally, a 70-nm-thick Ag layer with an active area of 0.09 cm^2 was vacuum-deposited through a shadow mask. Pictured in **Figure 2-1** are the overall steps for fabricating devices.

2.3.2   Fabrication Process of Sn-Based Solar Cells

2.3.2.1   Preparation of Sn-Perovskite films

For the FASnI$_3$ perovskite film, an equimolar ratio of SnI$_2$ and FAI was combined with 10 mol% SnF$_2$ in 1 ml DMSO solvent. Different amounts of DAGCl or 4F-PHCl were included in the perovskite-based solution for the modification. EDAI$_2$ was added to all of the precursor solutions at a concentration of 1.5 mol%. For the fabrication of the FASnI$_3$ film, the precursor solution was spin-coated at 5000 rpm for 62 seconds before being annealed at 100 °C for 10 min. After 34 seconds of spin-coating, the antisolvent chlorobenzene was dripped over the spinning sample.

2.3.2.2   Solar Cells Fabrication

Sn-PSCs were fabricated on the patterned indium tin oxide (ITO) coated glass substrates. The substrates were ultrasonically cleaned with detergent, de-ionized water, acetone, and ethanol, respectively, for 10 min each. After that, the cleaned ITO substrates were exposed to UV/ozone radiation for 30 minutes to remove any contaminants. A PEDOT: PSS hole transport layer was deposited on top of the ITO substrate by spin-coating at 4000 rpm for 30 s. The PEDOT: PSS films were then annealed at 150 °C for 30 min and cooled down to room temperature. After cooling at room temperature, the substrates were transferred to the N$_2$ glove box, and the FASnI$_3$ films were deposited. Subsequently, C$_{60}$ (50nm) electron transport layer and BCP (7 nm) were deposited by carrying out thermal evaporation at the rate of 1.0 /s. Finally, a 60 nm thick Ag layer was vacuum deposited through a shadow mask with an active area of 0.09 cm^2. **Figure 2-2** shows the fabrication steps for Sn-PSC. For encapsulation of PSCs, we added a little amount of UV glue on the edges of transparent cavity glass and covered the solar cell. The encapsulation was finished after 15 s of soaking under UV light (**Figure 2-2c**).
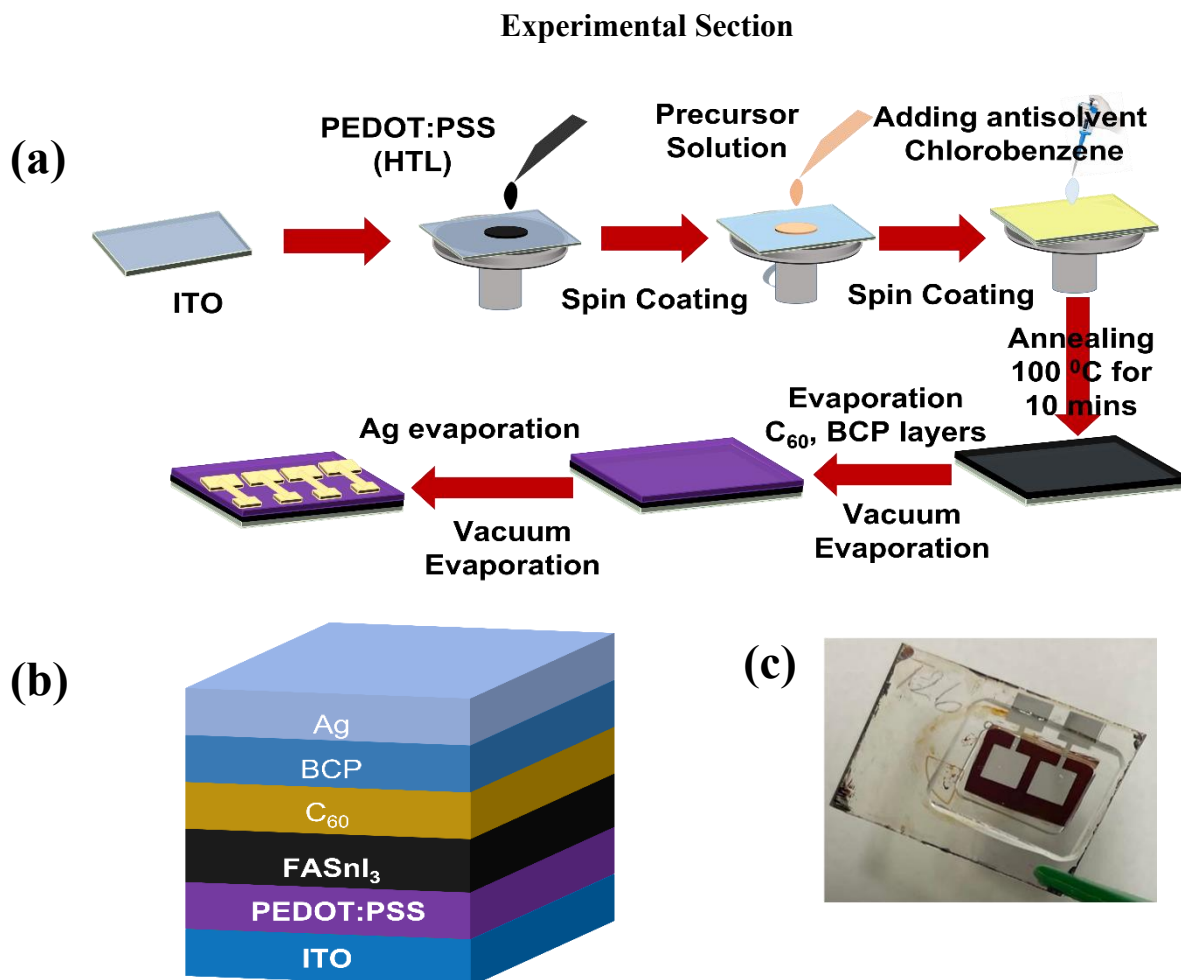
Figure 2-2. (a) The fabrication steps of Sn-based perovskite solar cells. (b) Fabricated Sn-PSC structure. (c) Encapsulated Sn-PSC.

2.4 Characterization

Fourier transform infrared (FTIR) measurements were performed to study the bonding between the used organic additives with SnI_2. X-ray diffraction (XRD) measurements were carried out on the perovskite films to confirm the crystal structure. The top view of surface morphological images of films was obtained using screening electron microscopy (SEM) with energy-dispersive spectroscopy (EDX) for element mapping. The UV−visible absorption spectra were measured to study the band gaps of the perovskite films. The photoelectron emission spectra were measured using an AC-3E photoelectron spectrometer for Sn-perovskite and UPS for Bi-perovskite. The steady-state photoluminescence (PL) and time-resolved photoluminescence (TRPL) spectra were measured to understand the charge transfer properties and kinetics of the fabricated perovskite films. The changes in electron mobility and electron trap-state density of the perovskite films were evaluated by dark current-voltage ($J−V$) analysis for electron-only devices. To investigate the effect of additives on the photovoltaic performance of PSCs, we fabricated the PSCs. The current density-voltage ($J-V$) and incident photon-to-current efficiency

(IPCE) of the fabricated PSCs were measured. The transient photocurrent (TPC) decay and the transient photovoltage (TPV) decay were measured in the PSCs to obtain information about the electron transportation process and the change in the carrier recombination process. The charge recombination of the PSCs was also examined using electrochemical impedance spectroscopy (EIS). Finally, the operational stability under maximum power point conditions and stability inside an N_2 glovebox were investigated. **Figure 2-3** shows the image of instrumental tools used for the fabrication and characterization of PSCs.
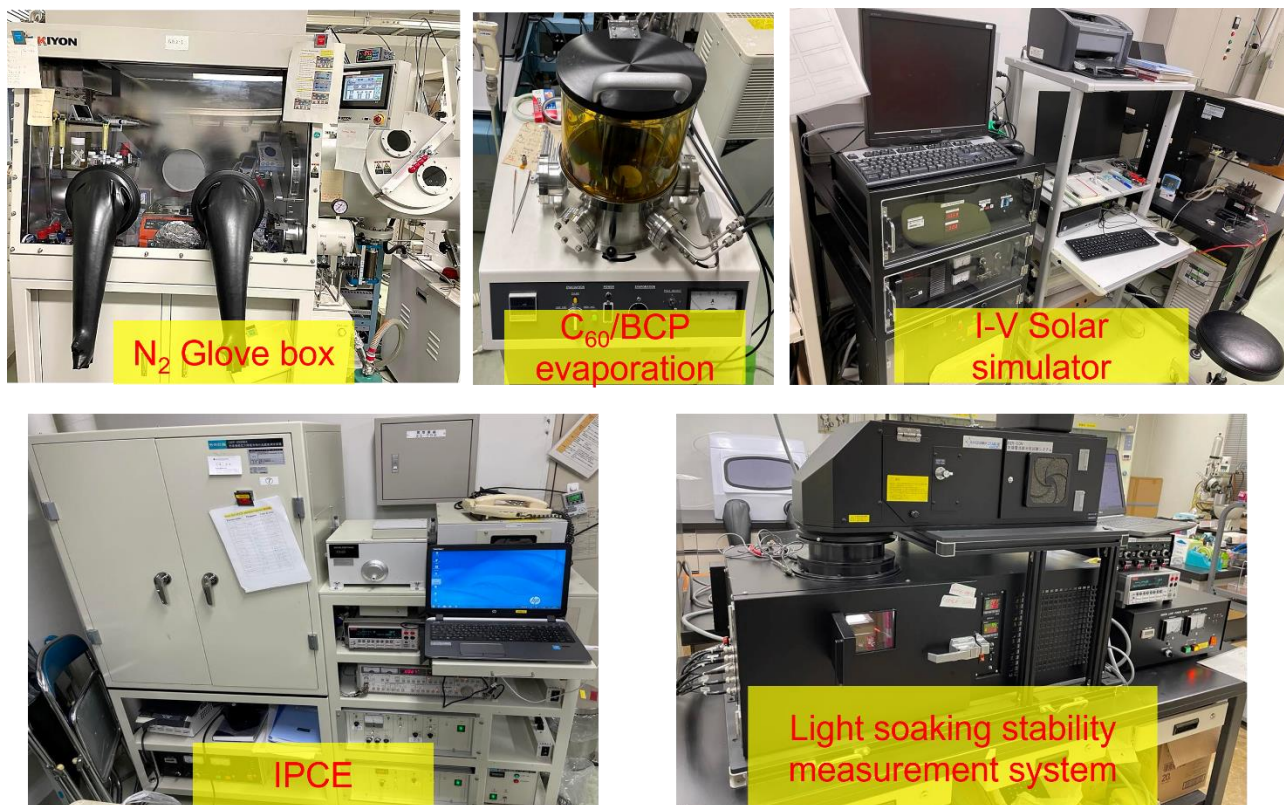

Figure 2-3. The instruments used for the fabrication and characterization of PSCs.

CHAPTER 3:
RESULTS AND
DISCUSSION

3.1 Bathocuproine Interfacial Layer Leads to Solid Improvement of Reproducibility and Stability of Pb-free CsBi$_3$I$_{10}$-Based Perovskite Solar Cells

Results and Discussion

3.1.1 Crystallographic Properties of Bi-Perovskite Films

First, we fabricated the CBI films on top of the ITO/PEDOT: PSS using a two-step spin coating process. We used precursor solutions with different molar concentrations (0.8M, 1.0M, or 1.2 M) and defined them as CBI-1 (0.8 M), CBI-2 (1.0 M), and CBI-3 (1.2 M), respectively. Second, the optimized CBI-2 (1.0 M) films were annealed at 80 °C, 100 °C, 120 °C, and 140 °C to understand the effects of annealing temperature on the nucleation and crystal growth properties.

We used X-Ray diffraction (XRD) to examine the structural properties of the obtained CBI films after changing the respective precursor solution concentration and annealing at 120 °C. **Figure 3.1-1a** shows the XRD patterns at different molar concentrations of the precursor solution of CBI on top of the ITO/PEDOT: PSS. The CBI film shows certain diffraction peaks primarily located at 12.87°, 24.50°, 25.72°, and 41.71°. These diffraction peaks are easily assigned to (003), (006), (115), and (300) crystal planes of the hexagonal CBI phase, respectively. The peaks plane (003), (006), (115), and (300) indicate that CBI had a layered crystal structure.[57, 59] CBI-2(1.0 M) had the most significant highly intensified peaks from (003) and (006) crystal planes rather than CBI-1 (0.8 M) and CBI-3 (1.2 M). The results show that CBI-2 (1.0 M) film annealed at 120 °C has better crystallinity than other fabrication conditions. The other two crystal planes (115) and (300) were observed with the same intensity for all precursor solution concentrations.
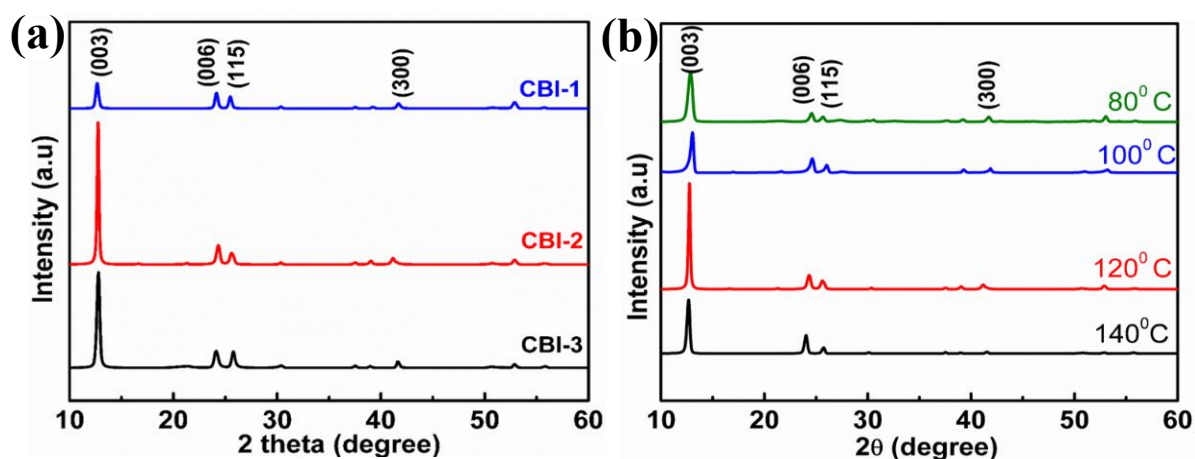

Figure 3.1-1. (a) XRD of CBI films on ITO/PEDOT: PSS with different solution concentrations and annealed at 120 °C. (b) XRD of CBI-2 (1.0 M) films on ITO/PEDOT: PSS and annealed at 80 °C, 100 °C, 120 °C, and 140 °C.

Results and Discussion

We examined the effect of annealing temperature on the crystallization of CBI-2 (1.0 M) films. **Figure 3.1-1b** shows the XRD patterns of CBI-2(1.0 M) films annealed at 80 °C, 100 °C, 120 °C, and 140 °C. To obtain the best crystallinity, the most intensified diffraction peaks (003) at $2\theta = 12.87°$ and (006) at $2\theta = 24.50°$ are observed for 120 °C post-annealing temperature, indicating that the suitable annealing temperature was 120 °C. Furthermore, when the annealing temperature was increased to 140 °C, the intensity of the prominent diffraction peak became weaker, indicating a decrease in the crystallinity. The faster nucleation at higher annealing temperatures would decrease the crystal quality of the thin films at >120 °C. To gain a better understanding, we calculated the crystallographic parameters for the peak at $2\theta = 12.87°$ of the CBI films grown in different fabrication conditions (**Figure 3.1-2**). The CBI-1 (0.8 M) and CBI-3 (1.2 M) films annealed at 120 °C exhibited full width at half maximum (FWHM) of 0.32° and 0.26°, respectively; however, the CBI-2 (1.0 M) film annealed at 120 °C exhibited narrower FWHM of 0.21°. Moreover, we calculated the crystal size of the respective CBI films to quantitatively evaluate the crystallization under different fabrication conditions.

The CBI-2 (1.0 M) film produced the largest average crystal size of 38 nm among the attempted fabrication conditions (**Figure 3.1-2a, b**). Previously, our group found that the average crystal size of the CBI perovskite was about 30 nm on top of the ITO/NiO$_x$.[59] The appropriate solution concentration and annealing temperature helped to improve the crystallinity of the CBI perovskite films. The larger the crystal size, the lower the grain boundaries and defects. This result is important for optimized fabrication conditions. The defect concentration and non-radiative recombination are closely associated with a micro-strain.[87] CBI-2 (1.0 M) thin films annealed at 120 °C exhibited a lower micro-strain value of 8.2 x 10^{-3}, while CBI-1 (0.8 M) and CBI-3 (1.2 M) thin films annealed at 120 °C exhibited micro-strain values of 12.7 x 10^{-3} and 10.1 x 10^{-3}, respectively (**Figure 3.1-2c**). For all fabrication conditions, the dislocation density values demonstrate a similar trend as micro-strain (**Figure 3.1-2c).** CBI-2 (1.0 M) films annealed at 120 °C exhibited lower micro-strain and dislocation density. Therefore, from these results, CBI-2 (1.0 M) thin films annealed at 120 °C have the lowest crystal defects among the attempted fabrication conditions.
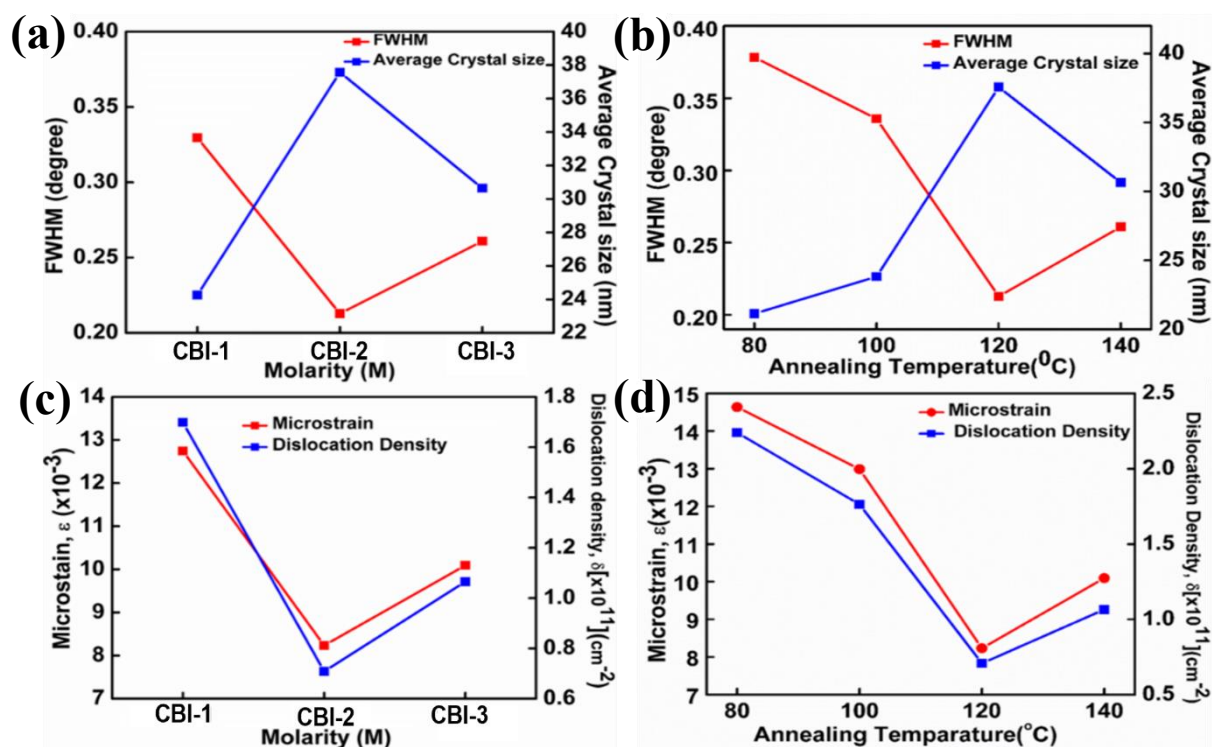
Figure 3.1-2. (a, b) Full-width half maxima (FWHM) and average crystal size: different molarity and annealing temperature of the CBI thin films at diffraction angle, $2\theta=12.87^0$. (c, d) Micro-stain and dislocation density: different molarity and annealing temperature of the CBI thin films at diffraction angle, $2\theta=12.87^0$.

We used the energy dispersion spectroscopy (EDX) mapping to confirm the element distribution of the CBI-2 (1.0 M) thin films annealed at 120 °C. The components of Cs, Bi, and I were uniformly distributed throughout the films (**Figure 3.1-3**). The atomic percentages of the element for CBI-2 (1.0 M) film were calculated to be Cs of 6.9 at.%, Bi of 21.47 at.%, and I of 71.63 at.%, respectively. The atomic percentages of each element are within an acceptable range and significantly close to the stoichiometric ratio of CBI thin film.[57]
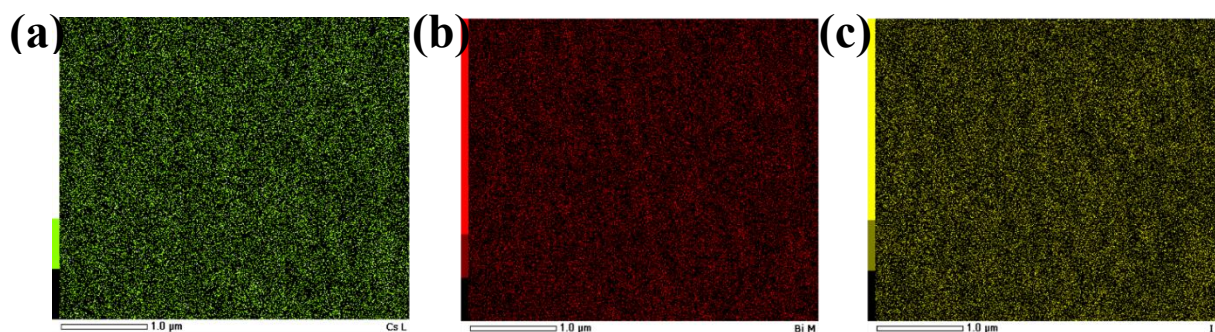

Figure 3.1-3. Energy dispersive X-Ray spectroscopy (EDX) element maps of CBI-2(1.0 M) thin film and annealed at 120 ^{0}C: (a) Cs, (b) Bi, (c) I.

Results and Discussion

3.1.2 Photophysical Properties of Perovskite Films

UV–Vis measurements were performed on CBI thin films to determine the absorption spectra and energy bandgap. **Figure 3.1-4a** shows the absorption spectrum for different concentrations of CBI thin films annealed at 120 °C. With increasing concentrations of CBI precursor solution, the absorption intensity gradually increases. The higher concentration affects the thickness of the film. The film's thickness is a critical factor for light absorption in the visible region. Increasing the solution concentration causes the film's color to change from light to deep (**Figure 3.1-5**). **Figure 3.1-4b** shows the absorption spectra of CBI-2 (1.0 M) thin films annealed at different temperatures. The highest absorption was obtained at 120 °C, indicating that the film's surface coverage was improved. The thickness of CBI-2 film annealed at 120 °C was about 550 nm. The absorption spectrum dramatically decreases when annealed at 140 °C. This can be attributed to the decrease in surface coverage of the thin films at high temperatures.
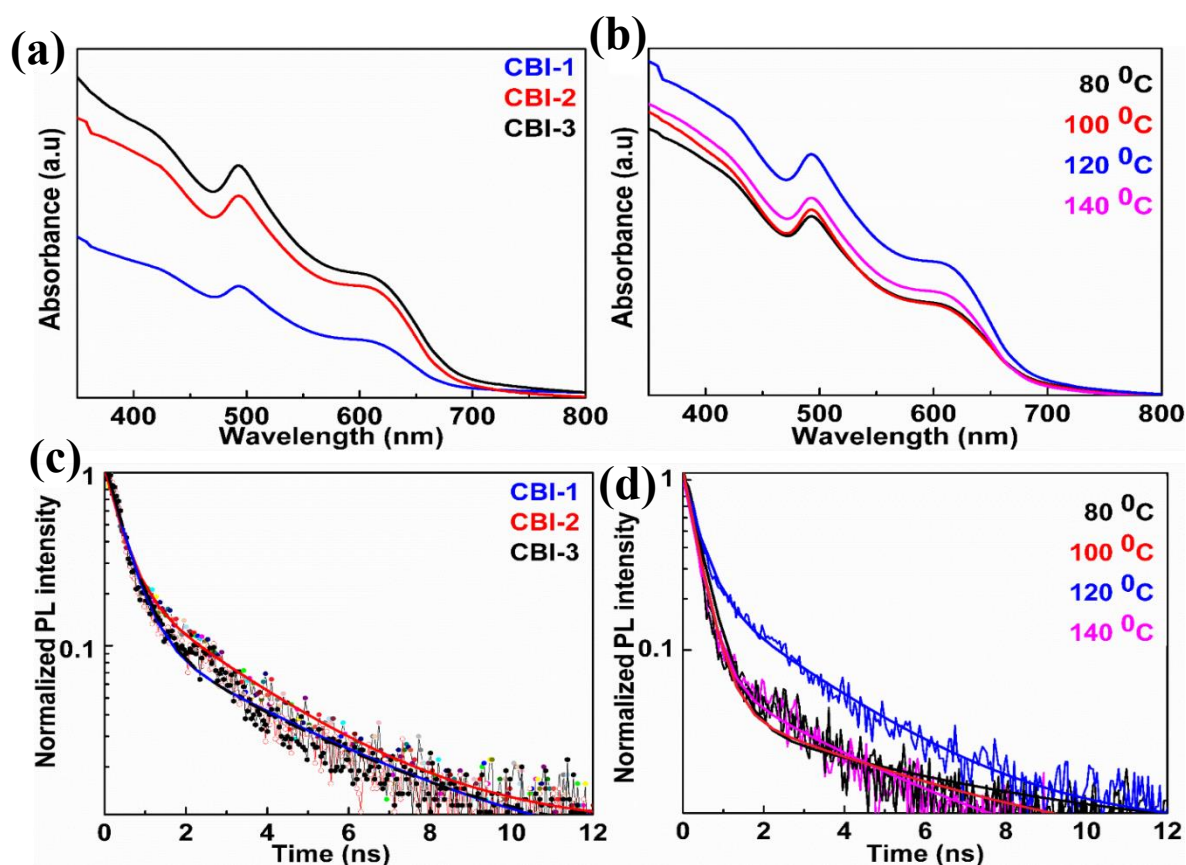

Figure 3.1-4. (a, b) Absorption spectra of CBI films on ITO/PEDOT: PSS. (c, d) Time-resolved PL decay curves (measured at 650 nm) of CBI films on glass.

Results and Discussion

TRPL decay technique fitted with a bi-exponential model was used to examine the effect of the precursor solution concentration and annealing temperature of CBI perovskite thin film on charge transport dynamics; the results are shown in **Figure 3.1-4c, d**. The longer PL lifetime τ_{ave} = 1.92 ns is obtained at CBI-2 (1.0 M) films compared to CBI-1 (0.8 M) of τ_{ave} = 1.63 ns and CBI-3 (1.2 M) of τ_{ave} = 1.67 ns films. CBI-3 (1.2 M) thicker perovskite films demonstrated shorter PL lifetimes, which could be attributed to increased charge recombination. Furthermore, we investigate the PL lifetime of CBI-2 (1.0 M) perovskite thin film annealed at different temperatures. The longest PL lifetime save for CBI-2 (1.0 M) annealed at 120 °C was observed, which suggests fewer defects. The calculated lifetime for Figure **3.1-4d** is shown in **Table 3.1-1**.
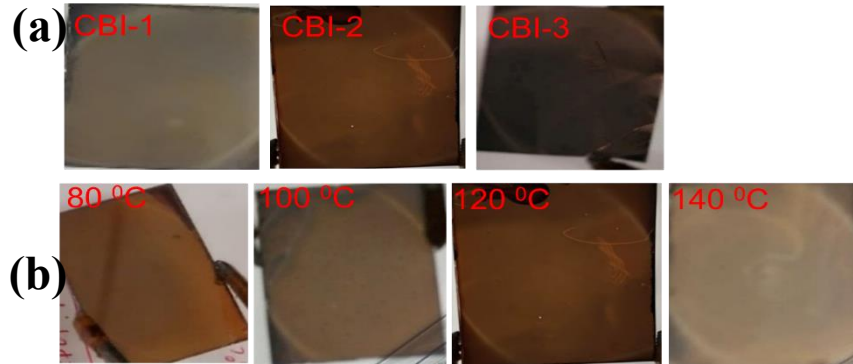

Figure 3.1-5. (a) CBI films for different concentrations annealed at 120 ^{0}C.(b) CBI-2(1.0 M) thin films at different annealing temperatures.

Table 3.1-1. Calculated PL Lifetime of CBI-2 perovskite films at different annealing temperatures.

Temperature (^{0} C)	τ_{avg}
80	1.49 ns
100	1.70 ns
120	1.92 ns
140	1.71 ns

Ultraviolet photoemission yield spectroscopy (UPS) measurement was used to determine the Fermi energy level (E_F) and the valence band energy level (E_V) of the CBI-2 (1.0 M) films annealed at 120 °C. The Fermi energy level and valence band maximum for CBI-2 (1.0 M) films were calculated using the UPS measurement at - 4.65 and - 5.91 eV, respectively (**Figure 3.1-6**). The optical bandgap of CBI-2 (1.0 M) thin

film was determined using the Tauc plots to be 1.78 eV (**Figure 3.1-6c**). Therefore, the conduction band minimum of the CBI-2 (1.0 M) film is calculated at - 4.13 eV (**Figure 3.1-6d**). The E_F energy level is located above the middle value of the bandgap.
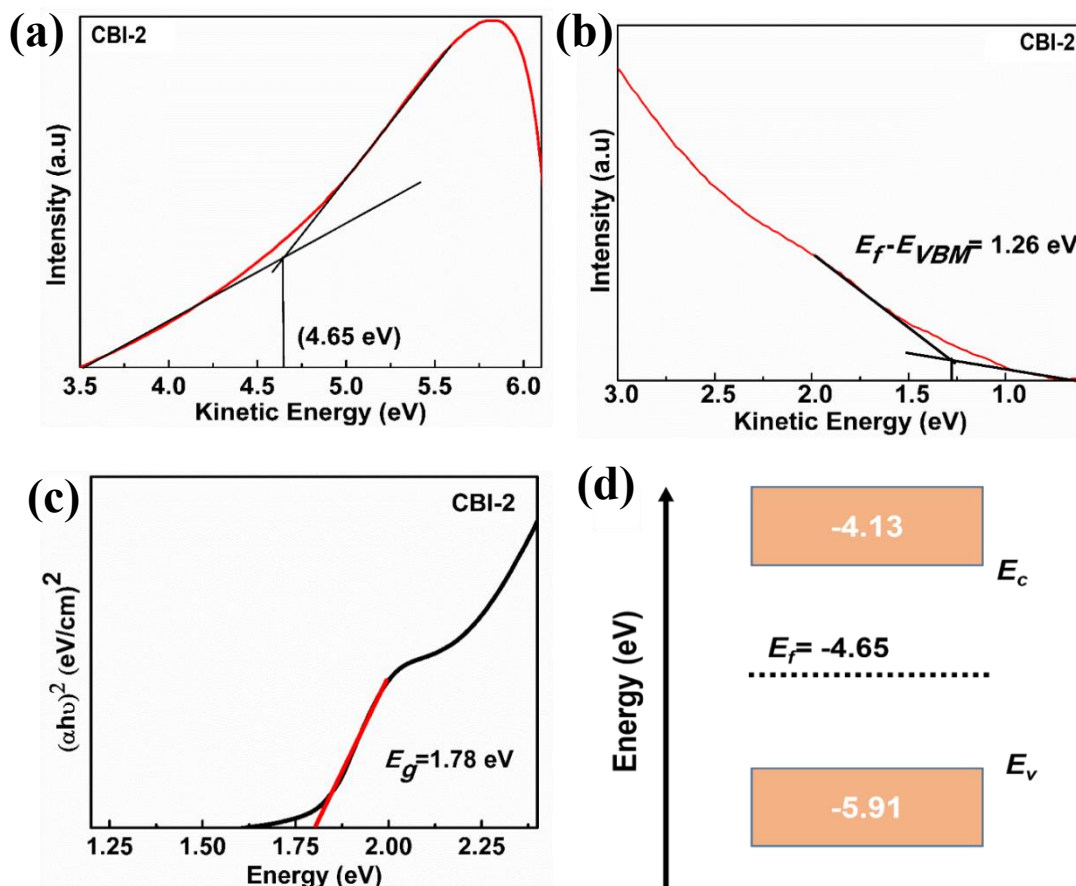

Figure 3.1-6. (a,b) UPS spectrum measurement of CBI-2 (1.0 M) thin film annealed at 120 °C. (c) Plot of $(\alpha h\upsilon)^2$ vs. photon energy hυ for the CBI-2 (1.0 M) thin film annealed at 120 °C. (d) Experimental band energy level of the CBI-2 (1.0 M) thin film annealed at 120 °C.

3.1.3 Morphological Properties of Perovskite Films

Based on the above observations, CBI-2 (1.0 M) films annealed at 120 °C show better optoelectronic properties than other fabrication conditions. Although the CBI-2 (1.0 M) thin films annealed at 120 °C (from now defined as "control") have better crystallinity and optical properties than other fabrication conditions, nanoscale SEM observations confirmed that in the corresponding film, a few pinholes remain (**Figure 3.1-7a**). To overcome this limitation, we introduced (or included) a BIL on the top of the CBI layer, with control thickness using thermal evaporation. **Figure 3.1-7b–d** shows the nanoscale SEM images of the BIL-modified

perovskite thin films. We reported that introducing the BIL improved surface quality and reduced the number of pinholes that were responsible for the hole leakage from HTL to ETL through the CBI layer, resulting in maximum PSCs being short-circuited.
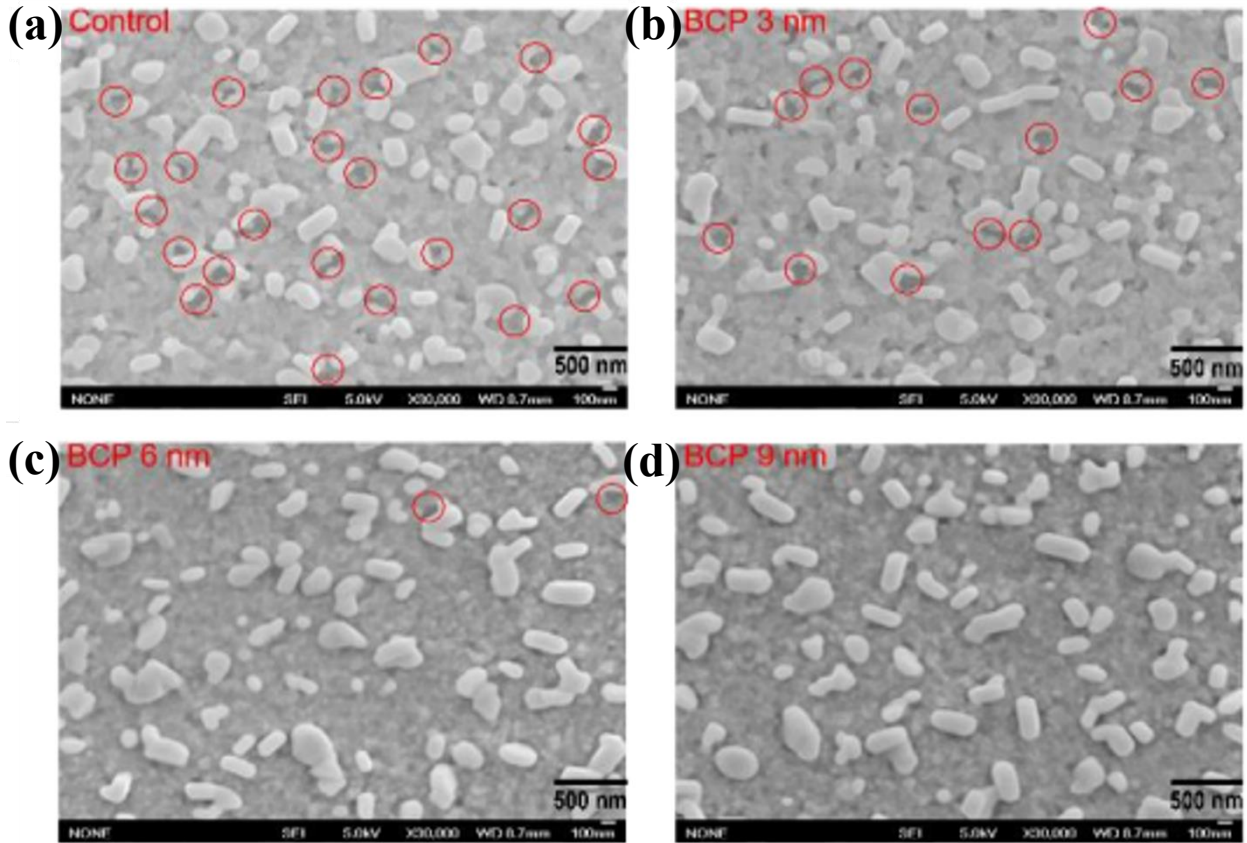

Figure 3.1-7. Nanoscale SEM images of perovskite films on ITO/PEDOT: PSS: (a) control, (b) with a 3 nm BIL, (c) with a 6 nm BIL, (d) with a 9 nm BIL.

3.1.4 Working Mechanism of BCP Interfacial Layer

We performed TRPL of the control/ETL and 6-nm sized BIL modified/ETL thin films to confirm the beneficial aspect of the BIL inclusion on top of the CBI layer. The TRPL decay curve is fitted by a biexponential model. The bi-exponential curve confirmed that BIL does not interfere with the carrier diffusion or may not act as a barrier for carrier injection to the ETL (**Figure 3.1-8**).

To evaluate the photovoltaic performance of control and BIL-modified perovskite thin films, we fabricated inverted planar type PSC (**Figure 3.1-9a, b**). The corresponding energy-level alignments of PSCs with control and BIL modification (**Figure 3.1-9c, d**). The wider bandgap BCP (3.5 eV) as an interfacial layer plays two important roles in the perovskite/ETL interface of PSCs configuration to improve PSCs performance.

Results and Discussion

First, BCP works as a hole leakage-blocking layer that limits the hole recombination to the ETL through the perovskite (**Figure 3.1-9b, d**). Second, BCP reduces the electrical interfacial resistance and increases the charge transportation of the perovskite/ETL interface.
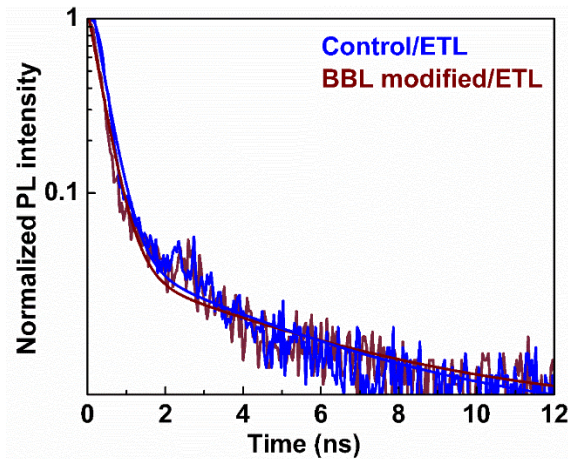

Figure 3.1-8. TRPL curves of the control/ETL and BIL modified/ETL thin film perovskite layer on the glass.
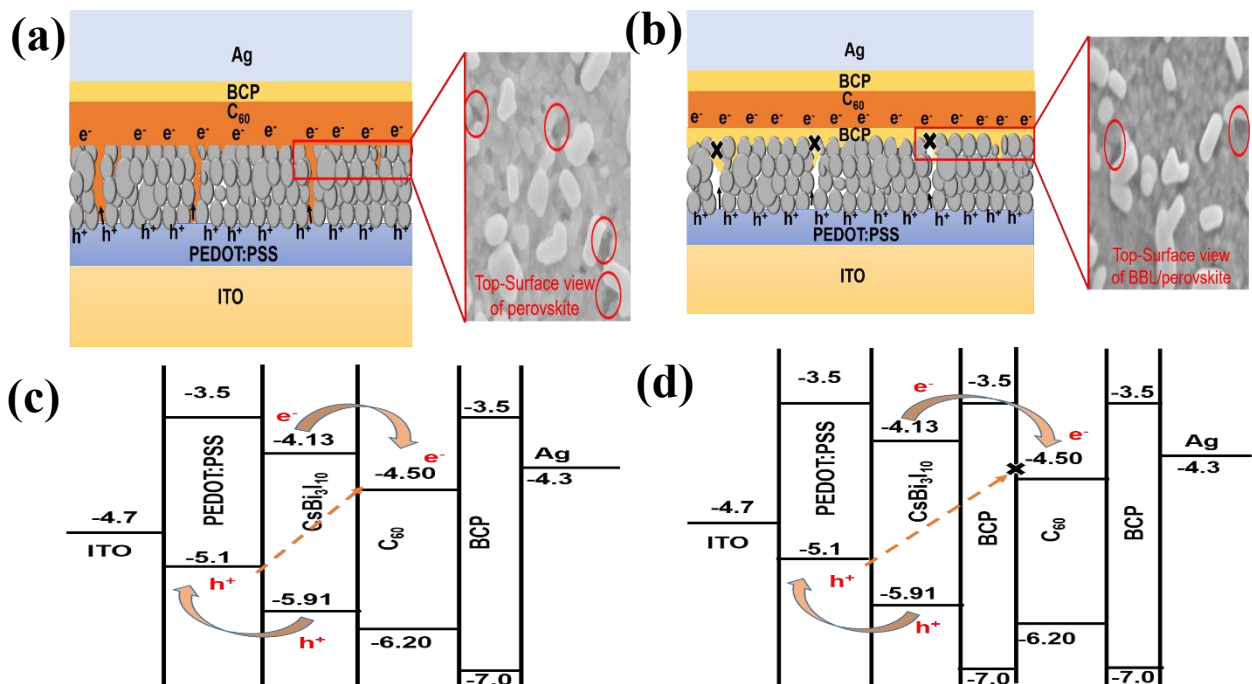

Figure 3.1-9. (a,b) Schematic diagram of control and BIL modified PSC. (c,d) Schematic energy band diagram of control and BIL modified PSC.

Results and Discussion

3.1.5 Photovoltaic Performance

A series of control PSCs were fabricated based on the structure shown in **Figure 3.1-9a**. The fabricated control PSC exhibited a maximum PCE of 0.38% with J_{SC} of 1.68 mA cm^{-2}, V_{OC} of 0.53 V, and FF of 43% (**Table 3.1-2**). The photovoltaic performance was measured under AM 1.5 G sunlight simulations (100 mW cm^{-2} illuminations) with an active area of 0.09 cm^2. The *J–V* curves of the control PSCs (8 PSCs are listed here) are shown in **Figure 3.1-10a**. Most PSCs exhibited a short-circuit or significantly low PCE, whereas few PSCs showed potential photovoltaic performance from a couple of batches of PSCs. The presence of pinholes within the control perovskite films could be responsible for the hole leakage to the ETL. Therefore, most PSCs exhibited short circuits and negatively affected the performance of photovoltaic devices.[88] Several batches of PSCs have been fabricated with BIL, and the photovoltaic performances were evaluated. **Figure 3.1-10b** shows the *J–V* curves of PSCs with control and BIL modification. PSC with a 6-nm-sized BIL modification demonstrated a maximum PCE of 0.80% with J_{SC} of 2.46 mA cm^{-2}, V_{OC} of 0.67 V, and FF of 49% in reverse scanning under the same measurement conditions.

Table 3.1-2. Photovoltaic performance parameters of PSCs with control and BIL modification.

Thickness of BIL	J_{SC} (mAcm^{-2})	V_{OC} (V)	FF	η (%)	R_s (Ωcm^{-2})	R_{sh} (Ω/cm^{-2})
0 nm	1.68	0.53	0.43	0.38	7.89	70.32
3 nm	2.21	0.67	0.46	0.68	5.25	81.36
6 nm	2.46	0.67	0.49	0.80	3.17	96.25
9 nm	2.40	0.63	0.45	0.68	5.26	89.96

Note that the PCE first increased with increasing BIL thickness, achieving a maximum of 0.80% when the BIL thickness was equal to 6 nm, and then decreased with increasing BIL thickness. **Table 3.1-2** lists the best performance parameters of PSCs with different thicknesses of the BIL layer. J_{SC} and FF increased first with increasing BIL thickness until 6 nm and decreased after 6 nm. The inclusion of BIL at the perovskite/ETL interface improved the interfacial contact and reduced the series resistance (R_S). The increase in J_{SC} and FF could be attributed to the decreases of R_S and recombination rate (larger shunt resistance R_{SH}) when the BIL layer thickness increases from 0 to 6 nm. However, the reverse trend was observed as the BIL thickness was increased beyond 6 nm. The thicker layer of the BIL reduced the interface contact between perovskite and ETL

in the PSC configuration as the R_S increased (**Table 3.1-2**). The J_{SC} and FF decreased due to the larger R_S and higher recombination rate induced by the thick BIL layer (**Table 3.1-2**). We infer that the thicker BIL behaves as an electron-blocking layer because of the wider bandgap.

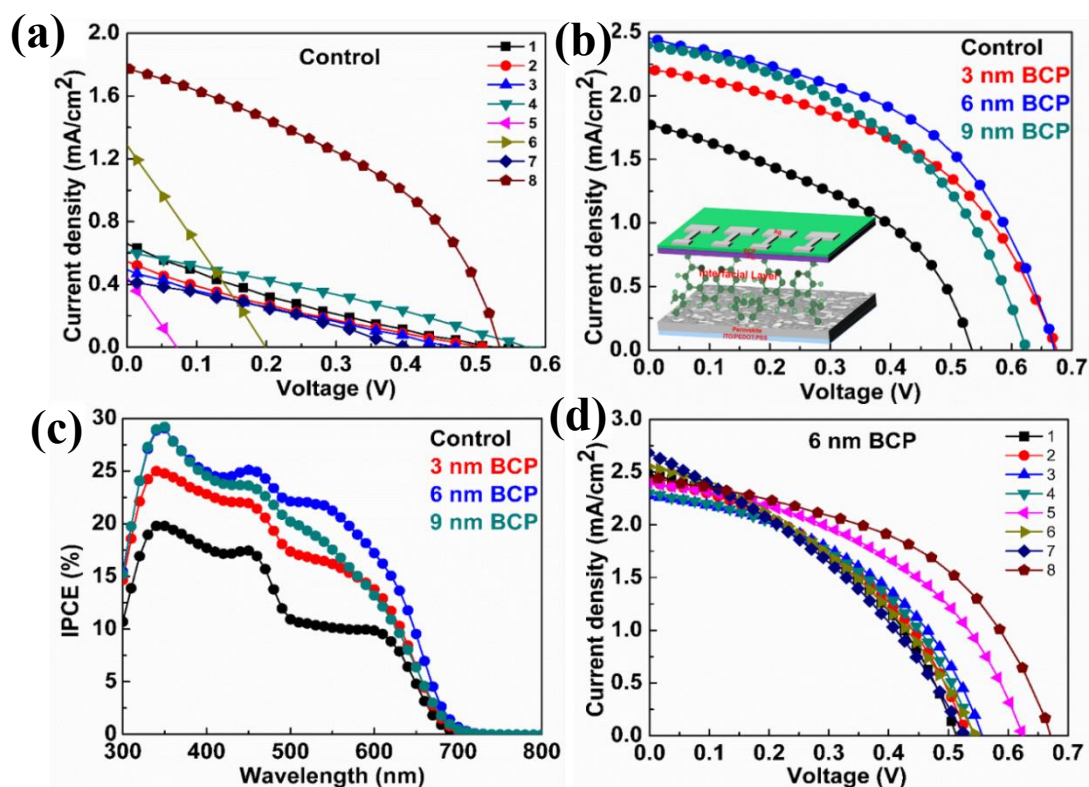**Figure 3.1-10.** (a, b) Reverse scan J–V curves of the perovskite thin films for control (8 PSCs) and modified PSCs. (c) IPCE spectra of the PCSs with control and BIL modification. (d) Reverse scan J–V curves of perovskite thin-film PSCs with a 6 nm BIL modification (8 PSCs are listed).
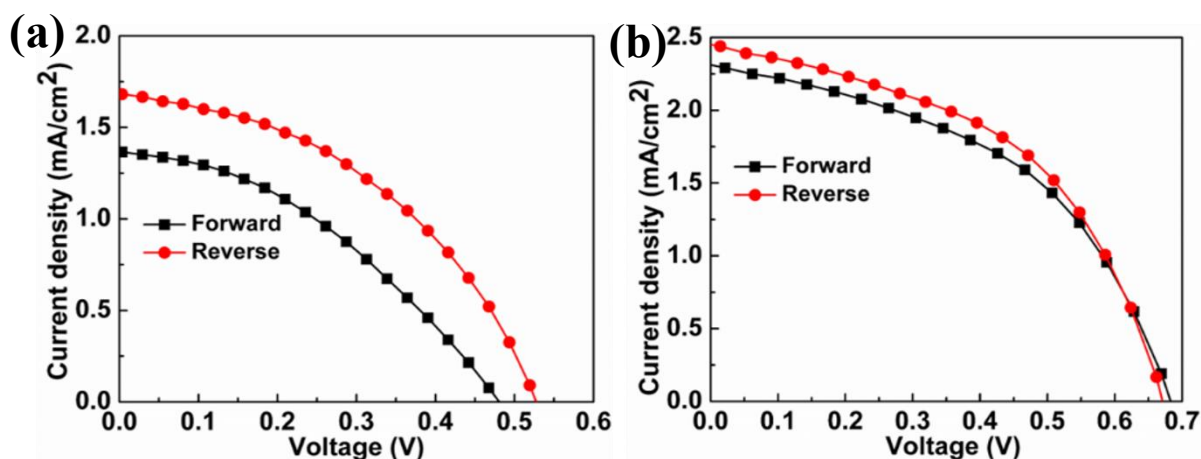

Figure 3.1-11. The forward and reverse scan J-V curve of PCS: (a) control, (b) 6 nm BIL modification.

Figure 3.1-10c shows the corresponding IPCE curves. The IPCE of the PSCs was measured to understand the spectral response. The champion PSC with a 6-nm-sized BIL demonstrates the highest IPCE response among the PSCs in this study. This result agrees with the J_{SC} trend. **Figure 3.1-11a, b** shows the forward and reverse scan $J–V$ curves of the control and 6-nm-sized BIL-modified PSCs. The PSCs with a 6-nm-sized BIL have a negligible hysteric effect. BIL improved the interface contact of perovskite/ETL and reduced the charge accumulation. The lower charge accumulation in the PSC structure potentially reduces the hysteresis effect (S-shape). **Figure 3.1-10d** shows the $J–V$ curves of PSCs with 6-nm-sized BIL (8 PSCs are listed here). From **Figure 3.1-10a, d**, it is observed that the BIL improved in the PSCs' reproducibility. The BIL assists in improving reproducibility by reducing or protecting from the short-circuit of PSCs.

3.1.6   Reproducibility and Stability
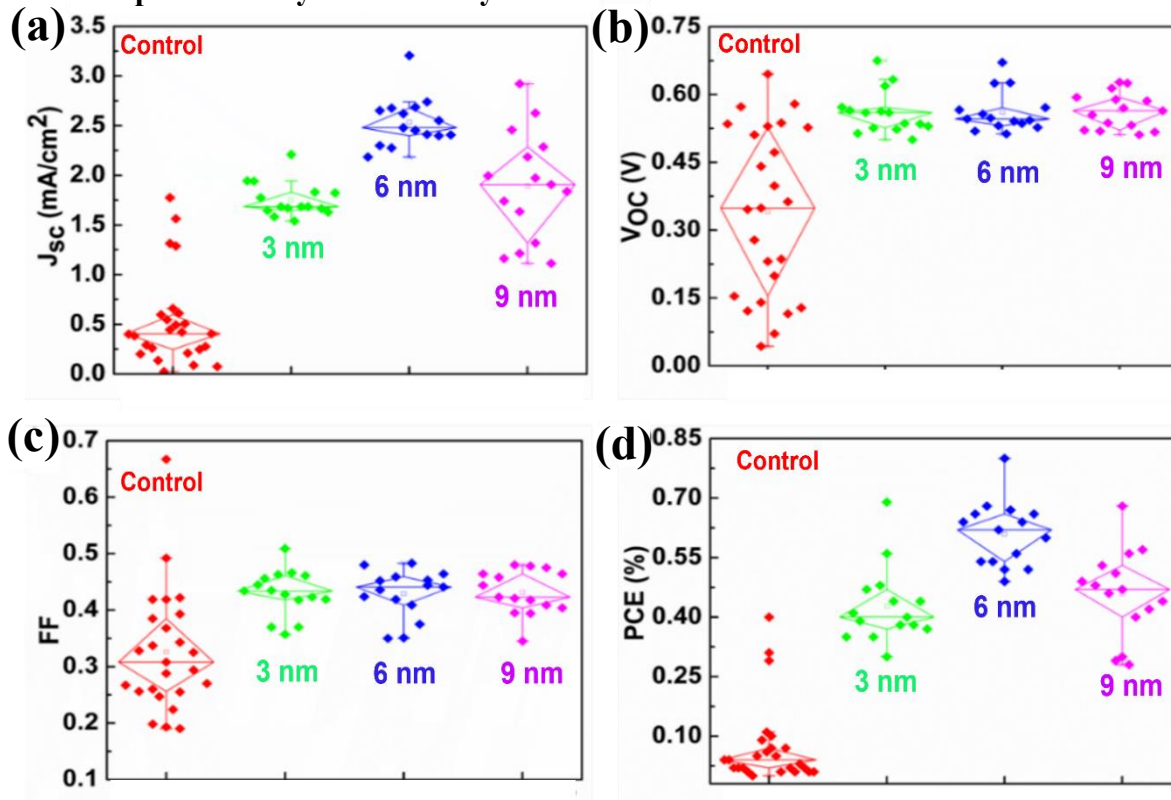
Figure 3.1-12. Performance parameters statistics of PSCs with control and BIL modification: (a) J_{SC}, (b) V_{OC}, (c) FF, (d) PCE.

Figure 3.1-12 shows the PSCs performance parameters such as J_{SC}, V_{OC}, FF, and PCE with control and BIL modification. The J_{SC} distribution of PSCs confirmed that the highest current density of 3.21 mA cm^{-2} was obtained with a 6-nm-sized BIL compared to other conditions (**Figure 3.1-12a**). The V_{OC} of PSCs with a BIL ranges from 0.5 to 0.68 V (**Figure 3.1-12b**). This is understandable because the V_{OC} of photovoltaic devices

depends on the relative energy levels of the absorber layer between the LUMO level of the ETL and the HOMO level of the HTL. **Figure 3.1-12c** shows the highest average value of the fill factor was obtained using a 6-nm-sized BIL layer. This result is attributed to the decrease in the PSCs' series resistance. After including BIL in the perovskite/ETL interface, PSCs demonstrated an improved PCE (**Figure 3.1-12d**). These observations indicate that the inclusion of BIL improves the performance of PSCs.
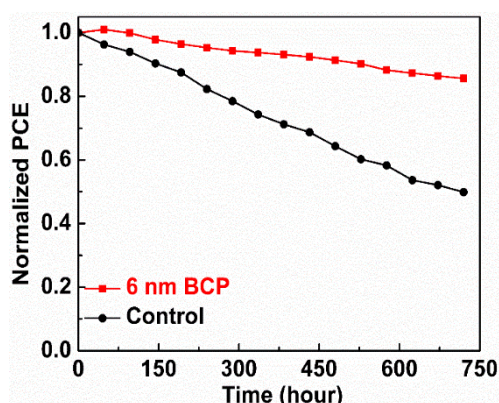

Figure 3.1-13. Normalized PCE of the PSCs with control and BIL modification as a function of time in an N_2 filled glove box.

We examined the effect of BIL on the long-term stability of the PSCs in an N_2 glove box, in addition to their performances. For the periodic photovoltaic performance measurements of the PSCs, they were taken out from the N_2 glovebox, and after the *J-V* measurement, the PSCs were stored in a glovebox. **Figure 3.1-13** shows the normalized PCEs of the control and 6-nm-sized BIL-modified PSCs. After 144 h, the champion control PSC retains approximately 90% of its initial PCE. After the BIL inclusion in the PSC configuration, it influenced the performance and stability of PSCs. The champion PSC with a 6 nm BIL retains ∼90% PCE of its initial efficiency after 528 h. The stability of the PSC with 6-nm-sized BIL is ∼4 times higher than that of control PSCs. This improved stability may be attributed to the reduction of interface charge accumulation. The stability data indicate that Bi perovskite will be a promising candidate in the photovoltaic device community.

In this study, we have demonstrated the reproducible and stable CBI PSCs with optimized fabrication conditions of thin films and introduced BIL at the perovskite/ETL interface. We obtained the best crystalline films with a molar concentration of 1 M and annealed them at 120 °C. The optimized CBI perovskite thin film showed a bandgap of 1.78 eV with a carrier lifetime of 1.92 ns. Furthermore, for the first time in Bi-PSCs, we introduced a BIL in the perovskite/ETL interface of inverted planar device structure; ITO/ PEDOT:

Results and Discussion

PSS/CBI/BCP/C$_{60}$/BCP/Ag. The inclusion of BIL at the perovskite/ETL interface reduced the possible hole leakage from the HTL to the ETL through CBI. The BIL reduced the interfacial defects at perovskite/ETL interfaces and improved the reproducibility of the respective PSCs. The PSC with a 6-nm-sized BIL has a maximum PCE of 0.80% and excellent reproducibility. Furthermore, the PSC exhibits negligible hysteresis effects and retains ~90% PCE of its initial efficiency after 528 h. Although the PCE of CBI PSC is still lacking; however, this study showed the pathway how to improve the reproducibility and stability of Bi-PSCs, which is a basic requirement for the systematic development of PCE.

3.2 Additive-Assisted Electronic Defect Passivation in Lead-Free Tin Perovskite Solar Cells: Suppression of Sn^{2+} Oxidation and I^- Losses

Results and Discussion

3.2.1 Interaction of 1,3-diaminoguanidine Monohydrochloride with Perovskite Precursor

To examine the interaction of DAGCl with SnI_2 and the formation of the hydrogen bonding, we measured the Fourier-transform infrared (FTIR) spectra for SnI_2 powder, SnI_2-DMSO adduct, DAGCl powder, and SnI_2-DAGCl adduct, as shown in **Figure 3.2-1a**. We can clearly see from the FTIR analysis that the stretching vibration frequencies of NH and NH_2 groups of DAGCl were shifted to lower wavenumbers after interaction with SnI_2, as shown in **Table 3.2-1**. This shift can be attributed to the formation of hydrogen bonding between DAGCl and iodide ions in SnI_2.[84] For SnI_2 and SnI_2-DMSO, no peaks appeared in the FTIR spectra. Additionally, we noticed a peak shift to a lower wavenumber due to the donation of the unshared electrons from the N atom of the C=N group in DAGCl to the vacant orbital of the Sn element.[89] Furthermore, the color of the DAGCl additive turned yellowish from white after interacting with SnI_2, as shown in **Figure 3.2-2**.
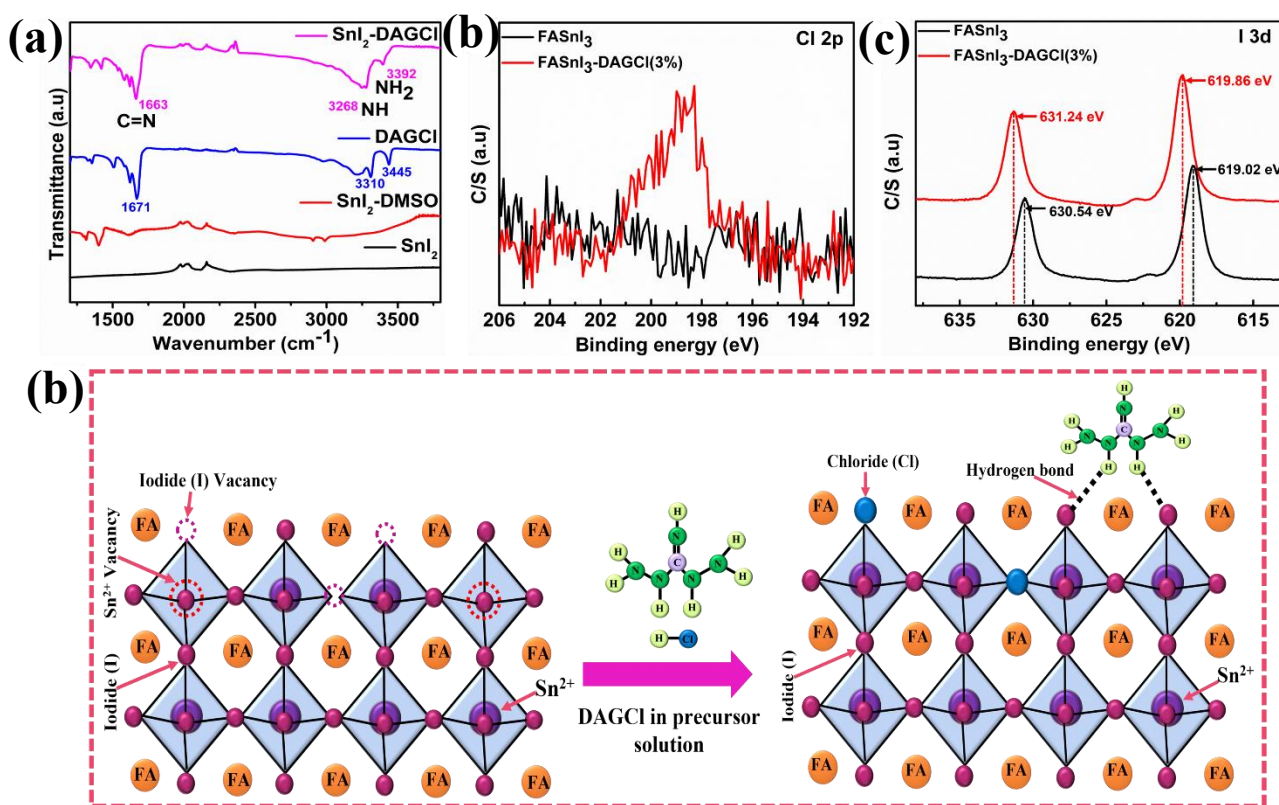

Figure 3.2-1. (a) FTIR spectra of SnI_2, SnI_2-DMSO, DAGCl, and SnI_2-DAGCl films. High-resolution XPS spectra of (b) Cl 2p and (c) I 3d of $FASnI_3$ films without and with an additive. (d) Diagram of a possible mechanism of DAGCl modification in $FASnI_3$ perovskite.

Results and Discussion

Table 3.2-1. FTIR analysis data for DAGCl and SnI_2-DAGCl adduct.

Group	DAGCl	SnI_2-DAGCl
NH	3310 cm^{-1}	3268 cm^{-1}
NH$_2$	3445 cm^{-1}	3392 cm^{-1}
C=N	1671 cm^{-1}	1663 cm^{-1}

SnI$_2$ **DAGCl**   **SnI$_2$+ DAGCl**

Figure 3.2-2. Pictorial presentation of SnI_2 powder, DAGCl powder and SnI_2+DAGCl adduct.

It can be concluded that guanidine-based additive materials have a strong interaction with SnI_2 and stabilize the weak Sn-I bond.[81] Also, an X-ray diffraction (XRD) analysis of SnI_2-DAGCl shows that the intensity of the main peak of SnI_2 becomes weaker, and there is a clear shift in the peak position, which is due to the interaction between SnI_2 and DAGCl, as shown in **Figure 3.2-3**. Additionally, the chemical interaction between DAGCl and perovskites was examined using X-ray photoelectron spectroscopy (XPS). The peak of Cl 2p (198.24 eV) was detected in the $FASnI_3$-DAGCl (3%) perovskite film, which can be assigned to the $SnCl_2$ peak and is in accord with our previous work, indicating the presence of the DAGCl additive in the final perovskite films, as shown in **Figure 3.2-1b**.[74] It is expected that such $SnCl_2$ formation of the respective films may result in lower oxidation. To further understand the influence of chemical interaction, we have observed the binding energy peaks of I 3d3 and I 3d5 for the pristine and $FASnI_3$-DAGCl (3%) films. The binding energies of peaks of I 3d3 (631.24 eV) and I 3d5 (619.86 eV) in the $FASnI_3$-DAGCl (3%) perovskite film shifted to higher energies as compared to the pristine perovskite film that exhibits peaks of I 3d3 (630.54 eV) and I 3d5 (619.02 eV), as shown in **Figure 3.2-1c**. These shifts indicate the successful electronic passivation of the respective perovskite films. From the above discussion, it is expected that the DAGCl additive could improve the perovskite structure through hydrogen bonding and reduce the Sn^{2+} oxidation and anionic vacancies, as shown in **Figure 3.2-1d**.
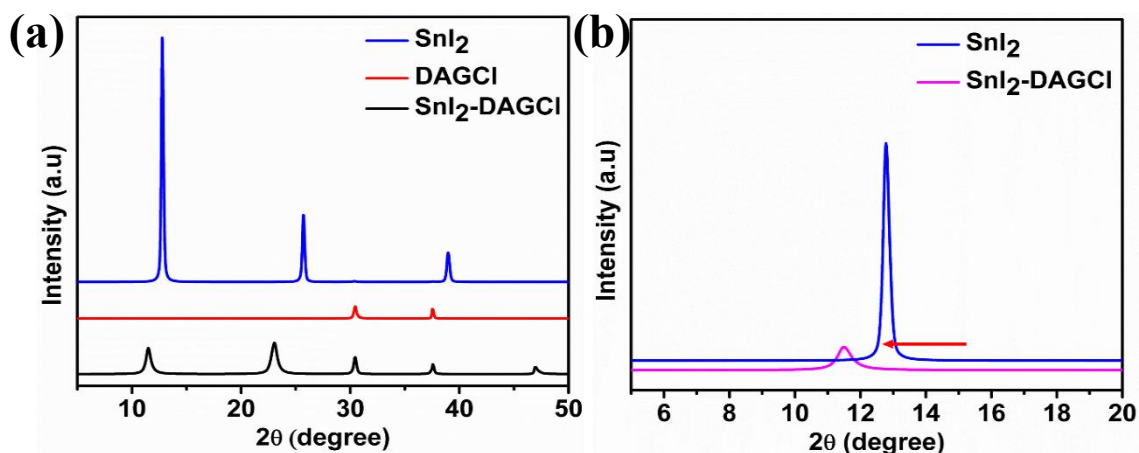
Results and Discussion

Figure 3.2-3. (a) XRD for SnI_2, DAGCl and SnI_2-DAGCl, (b) Magnification of XRD for SnI_2 and SnI_2-DAGCl.

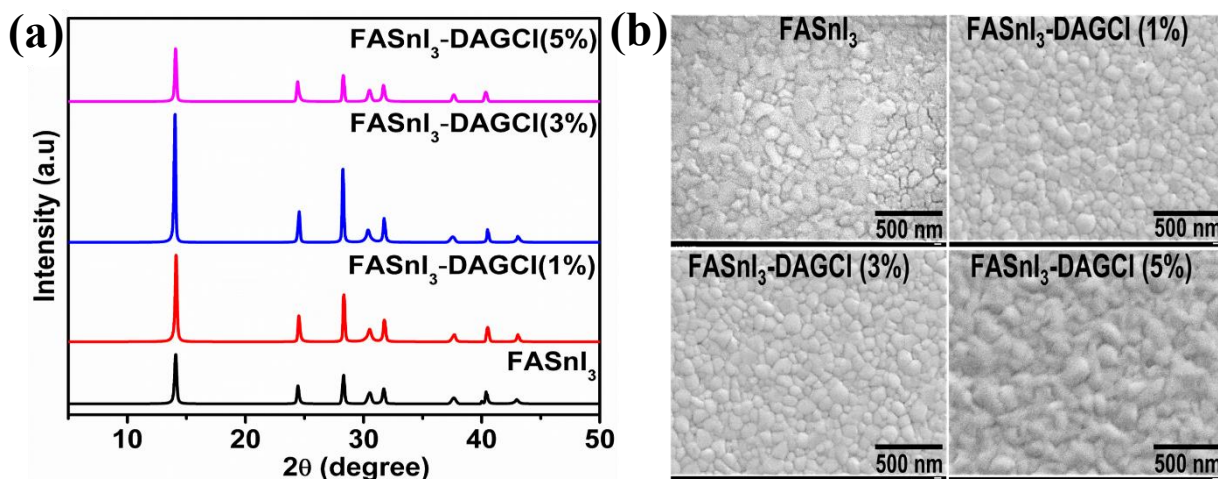### 3.2.2 Crystallinity and Morphology of the Perovskite Film

Figure 3.2-4. (a) XRD patterns and (b) SEM images of $FASnI_3$ perovskite films with 0, 1, 3, and 5 mol % DAGCl.

The XRD patterns of a series of $FASnI_3$ perovskite films with different concentrations of DAGCl were examined to better understand the influence of the DAGCl additive on the crystal structure of $FASnI_3$, as shown in **Figure 3.2-4a**. The highlighted diffraction peaks appear at 2θ angles of 14.14, 24.44, 28.34, 31.73, and 40.54°, which correspond to the crystallographic planes of (100), (102), (200), (122), and (222) of the orthorhombic $FASnI_3$ perovskite lattice (*Amm2* space group), respectively. In comparison to the pristine film, the intensity of (100) and (200) crystal planes increased with the DAGCl (3 mol %) additive in $FASnI_3$ perovskite films. Additionally, none of the samples exhibited diffraction peaks at low angles, or no additional peaks appeared in all samples. From the XRD results, we observed no peak shift up to the addition of 3 mol % of the DAGCl additive. But with the addition of 5 mol % of DAGCl, the XRD peak shifted to a lower angle,

Results and Discussion

as indicated in **Figure 3.2-5**. This type of a small XRD peak shift is possibly due to the incorporation of Cl⁻ ions into the lattice position. The finding from XRD indicated that the presence of a very negligible amount of DAGCl could help to improve the crystallinity and did not form a two-dimensional (2D) or quasi-2D structure.[90, 91] This improvement may be attributed to adding a small amount of DAGCl in the $FASnI_3$ precursor, which acts as an additive and is not integrated into the main lattice. Although DAGCl is a bulky material, we strongly believe that the trace amount of DAGCl did not form a 2D/3D heterostructure. **Table 3.2-2** shows the full width at half-maximum (FWHM) of $FASnI_3$ and modified $FASnI_3$ perovskite films. Interestingly, modified $FASnI_3$ perovskite films showed narrower FWHM for (100) and (200) peaks. Understandably, the small amount of the DAGCl additive induced better crystallinity than the pristine $FASnI_3$ perovskite. Notably, it is well known that changes in the FWHM of the XRD peaks could impact on the crystallographic parameters of the perovskite films. The crystallographic parameters such as grain size, dislocation density, and micro-strain are summarized for [200] crystal orientation in **Table 3.2-3**. To quantify the relevant crystallographic parameters of **Table 3.2-3**, we have used Bragg's law, the Debye-Scherrer formula, and crystal geometry as the following equations.

$$2d_{hkl}\sin\theta = n\lambda$$

Crystalline size $D_{hkl} = \dfrac{0.9\lambda}{\beta_{hkl}\times\cos\theta}$

Micro-strain, $\varepsilon = \dfrac{\beta_{hkl}}{4\tan\theta}$

Dislocation density, $\delta = \dfrac{15\varepsilon}{\alpha D_{hkl}}$

where, d_{hkl} and D_{hkl} are the interatomic distance and crystalline size along the [hkl] direction, λ is the wavelength of the X-ray (CuK_α radiation value = 0.15406 nm). β_{hkl} is the FWHM for the (hkl) diffraction peak.[92] The calculated average crystallite size was 62.15 nm for the $FASnI_3$-DAGCl (3%) film, increasing from 42.38 nm for the pristine $FASnI_3$ perovskite films. In addition, the modified $FASnI_3$-DAGCl (3%) film showed lower dislocation and micro-strain values than the pristine $FASnI_3$ perovskite films. These results clarify that the small amount of the DAGCl additive could improve the crystallographic properties. This improvement could reduce the V_{OC} loss and improve the overall photovoltaic performance.
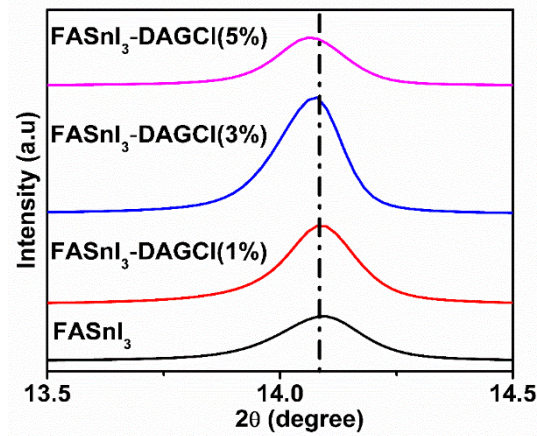
Results and Discussion

Figure 3.2-5. Magnification of XRD for FASnI$_3$ perovskite films with 0, 1, 3, and 5 mol % DAGCl in the range of $2\theta= 13.5^0$-14.5^0.

Table 3.2-2. Full width at half maxima (FWHM) of different peaks obtained from XRD at different angles.

Sample	FWHM at	
	14.10°	28.40°
FASnI$_3$	0.2064	0.1933
FASnI$_3$-DAGCl (1%)	0.1717	0.1445
FASnI$_3$-DAGCl (3%)	0.1577	0.1318
FASnI$_3$-DAGCl (5%)	0.1693	0.1801

Table 3.2-3. Calculated crystallite size, Dislocation density and Micro strain at (200) peaks from XRD results.

Sample	Crystallite size (nm)	Dislocation Density, $\delta \times 10^{-3}$ (nm)	Micro strain, ε [$\times 10^{-3}$]
FASnI$_3$	42.38	0.828	4.079
FASnI$_3$-DAGCl (1%)	56.70	0.533	3.271
FASnI$_3$-DAGCl (3%)	62.15	0.455	3.031
FASnI$_3$-DAGCl (5%)	45.48	0.623	3.543

Scanning electron microscope (SEM) images of perovskite films fabricated with the FASnI$_3$ precursor solution without and with the DAGCl additive are shown in **Figure 3.2-4b.** The pristine FASnI$_3$ perovskite film has shown numerous cracks and small grain sizes. By the inclusion of 1 or 3 mol % DAGCl additive, the

surface became more compact with bigger grains and showed considerably almost no crack at the grain boundary. Compared to the pristine FASnI₃, the grain size distribution of the perovskite films in **Figure 3.2-6** demonstrated a narrower distribution with a bigger grain size after the inclusion of 3 mol % DAGCl. The increased grain size and compact surface morphology of the modified FASnI₃ perovskite film can influence better charge transportation in the respective PSC. Although the highest concentration of additive (5 mol % DAGCl) has shown a bigger grain size than other conditions, a layer seems to form on top of the modified perovskite layer, as shown in **Figure 3.2-4b**. We suppose that this layer may hamper the effective charge transportation through the devices. The improvement of crystallinity and film morphology should be helpful for effective charge transportation and would enhance the photovoltaic performance of PSCs.
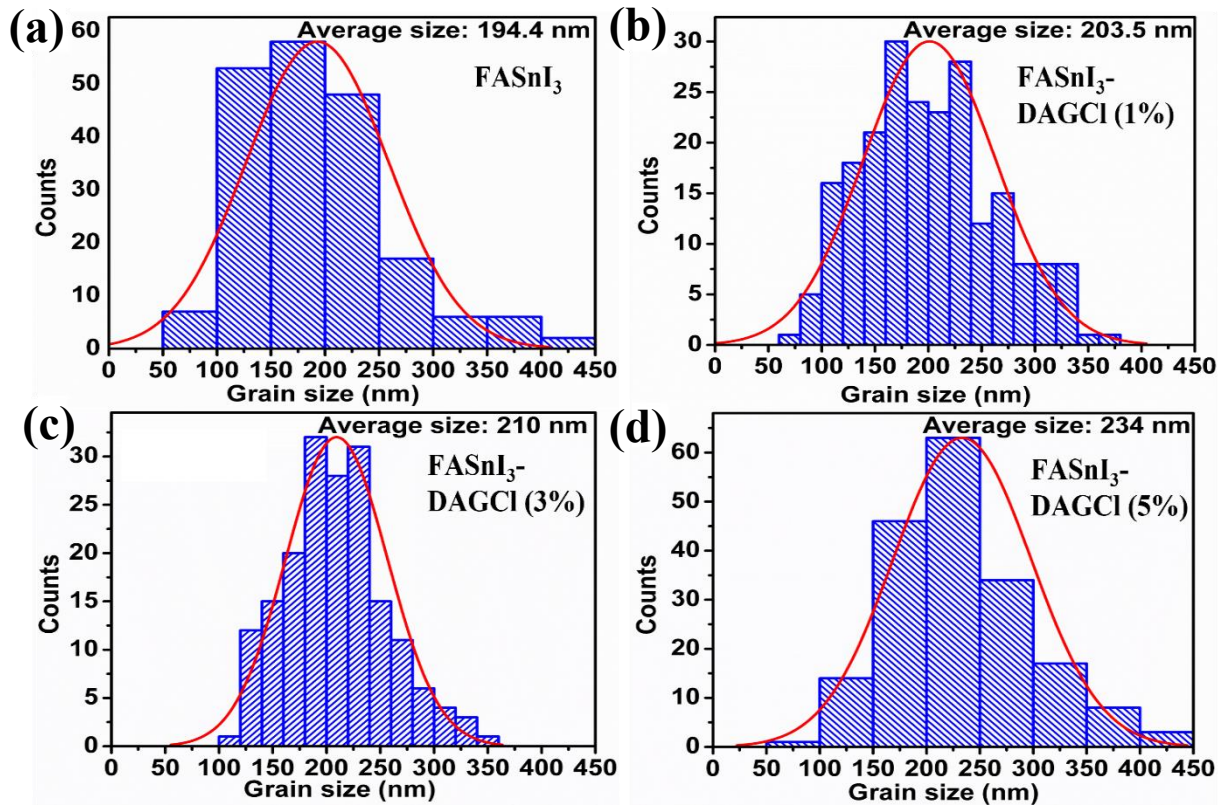
Figure 3.2-6. The graine size distribution of FASnI₃ perovskite film with (a) 0 mol%, (b) 1 mol%, (c) 3 mol% and (d) 5 mol% DAGCl, respectively. Grain size (total 200 for each case) calculated by ImageJ software.

3.2.3 Suppression of Sn^{2+} Oxidation and I^- Losses of Perovskite Film

The electronic defects of the perovskite films are responsible for the lower photovoltaic performance of PSCs. In Sn perovskite thin films, the defects are originated from the oxidation of Sn^{2+} and I^- loss and

responsible for serious deep-level traps, which results in severe nonradiative recombination. To evaluate the influence of DAGCl on the suppression of the Sn^{2+} oxidation level and I^- loss on the surface of the $FASnI_3$ film, we performed XPS measurements on the fabricated perovskite films. We quantify the content of Sn^{2+} and Sn^{4+} of the perovskite films for pristine and modified perovskite films, as shown in **Figure 3.2-7**.

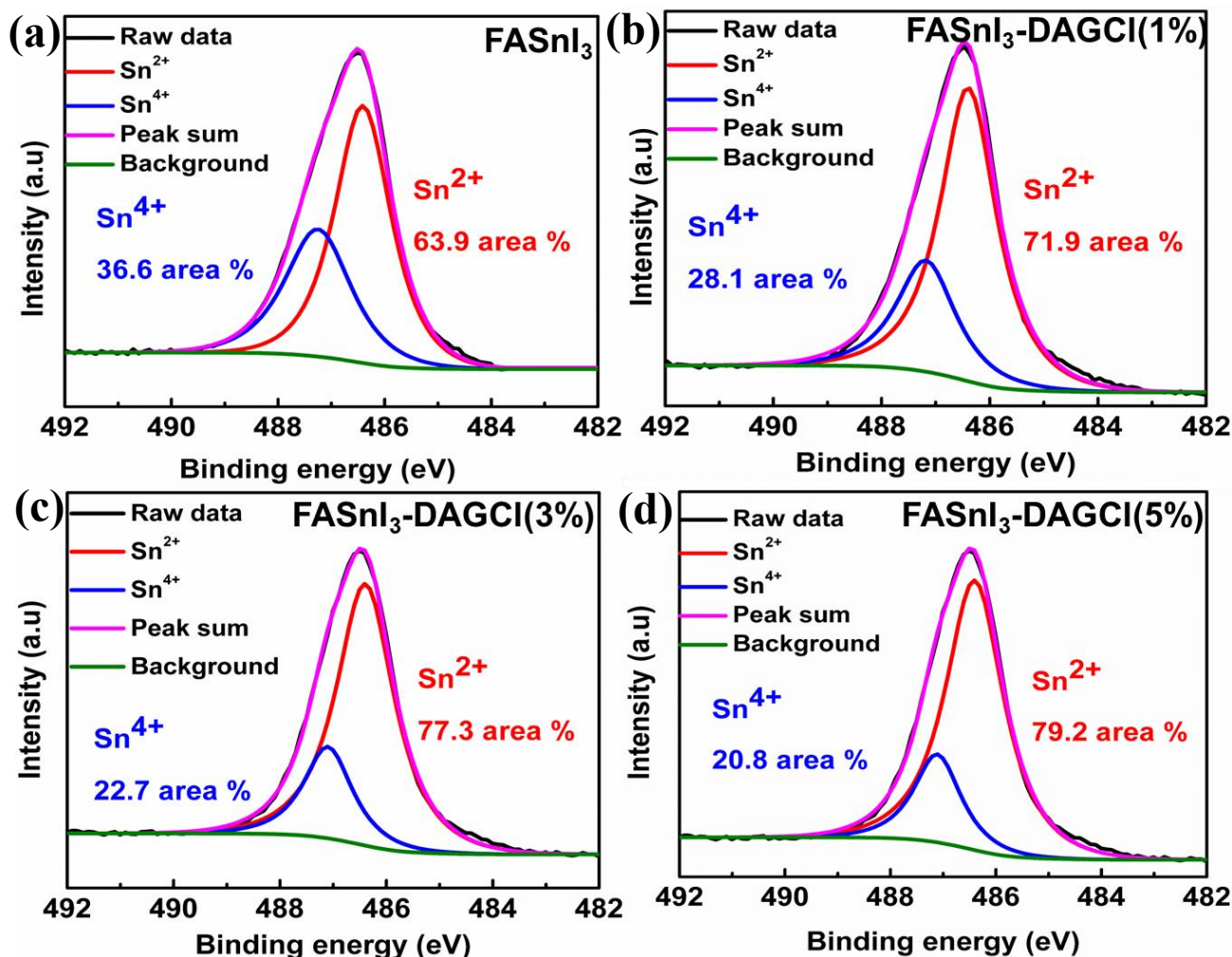**Figure 3.2-7.** High-resolution XPS spectra for Sn $3d_{5/2}$ of $FASnI_3$ films with (a) 0 mol%, (b) 1 mol%, (c) 3 mol% and (d) 5 mol% DAGCl, respectively.

It can clearly be seen that the Sn^{4+} content of the pristine $FASnI_3$ film is 36.6%, significantly decreasing to 22.7% of $FASnI_3$-DAGCl (3%) films. The details of XPS-related data for $FASnI_3$ and $FASnI_3$-DAGCl (3%) are shown in **Table 3.2-4.** The reduction of the content of Sn^{4+} by 38% in the $FASnI_3$-DAGCl (3%) films compared to $FASnI_3$ films indicates that the DAGCl additive can significantly suppress the oxidation of Sn^{2+} to Sn^{4+}. The DAGCl additive in the perovskite solution not only improves the crystallinity and film morphology and suppresses the oxidation of Sn^{2+} to Sn^{4+} but also may suppress the loss of I^- in the fabricated

Results and Discussion

perovskite films and may enhance the stability of the perovskite structure. To justify the suppression of I^- loss after the inclusion of the DAGCl additive, we have calculated the amount of I^- in pristine and DAGCl modified perovskite films, as shown in **Figure 3.2-8**. The perovskite film with 3 mol% DAGCl additive possesses a higher percentage of I^- (up to 82.5%), which is much higher than that (69.6%) of the pristine film. The lower I^- loss found on the perovskite film with 3 mol % DAGCl can be attributed to the hydrogen bonding ($-NH \cdots I^-$) between polar hydrogen groups ($N^{\delta-}-H^{\delta+}$) of DAGCl and the electronegative iodide ion ($I^{\delta-}$) in the respective film. The strong hydrogen bond suppressed the oxidation of I^- to I_3^- or I_2 and reduced the loss of I^- of the $FASnI_3$ perovskite films.[83] The addition of the DAGCl additive improved the ratio of Sn^{2+}/I^- (1:2.34), whereas the pristine perovskite film has a nonstoichiometric ratio of 1:1.92, as shown in **Table 3.2-4**.

Table 3.2-4. The fitting results of XPS spectra for the pristine $FASnI_3$ and modified $FASnI_3$-DAGCl (3%) films.

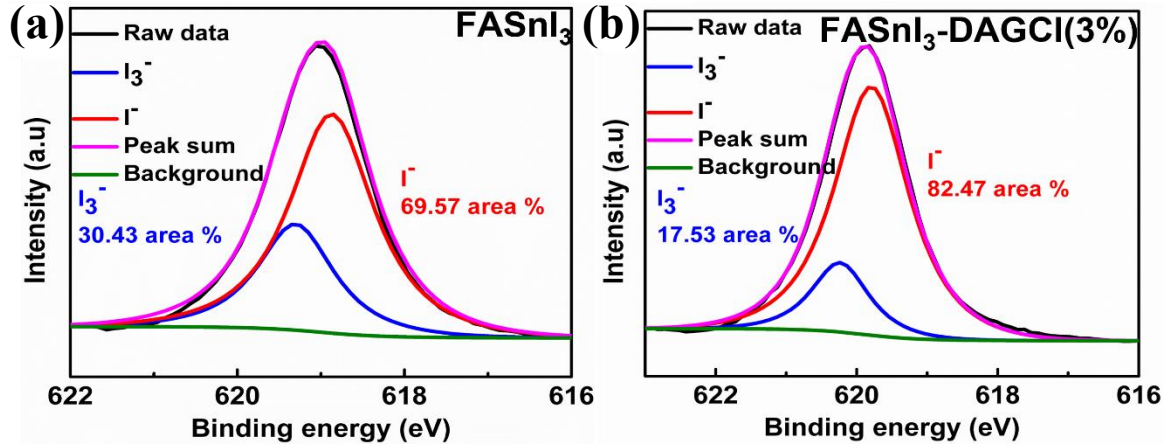| FASnI$_3$	Sn 3$d_{5/2}$		I 3$d_{5/2}$		Stoichiometric ratio of Sn^{2+} and I$^-$
	Sn^{2+}	Sn^{4+}	I$^-$	I$_3^-$	
Position (eV)	486.407	487.25	618.868	619.301	1:1.92
Area	7486.28	4325.13	14382.3	6288.34	
FASnI$_3$-DAGCl (3%)	Sn 3$d_{5/2}$		I 3$d_{5/2}$		
	Sn^{2+}	Sn^{4+}	I$^-$	I$_3^-$	
Position (eV)	486.40	487.09	619.788	620.235	1:2.34
Area	8059.7	3198.4	18918.5	4023.26	

Figure 3.2-8. High-resolution XPS spectra of FASnI$_3$ and FASnI$_3$-DAGCl (3%) films for (a,b) I 3$d_{5/2}$, respectively.

3.2.4 Photophysical Properties of Perovskite Film

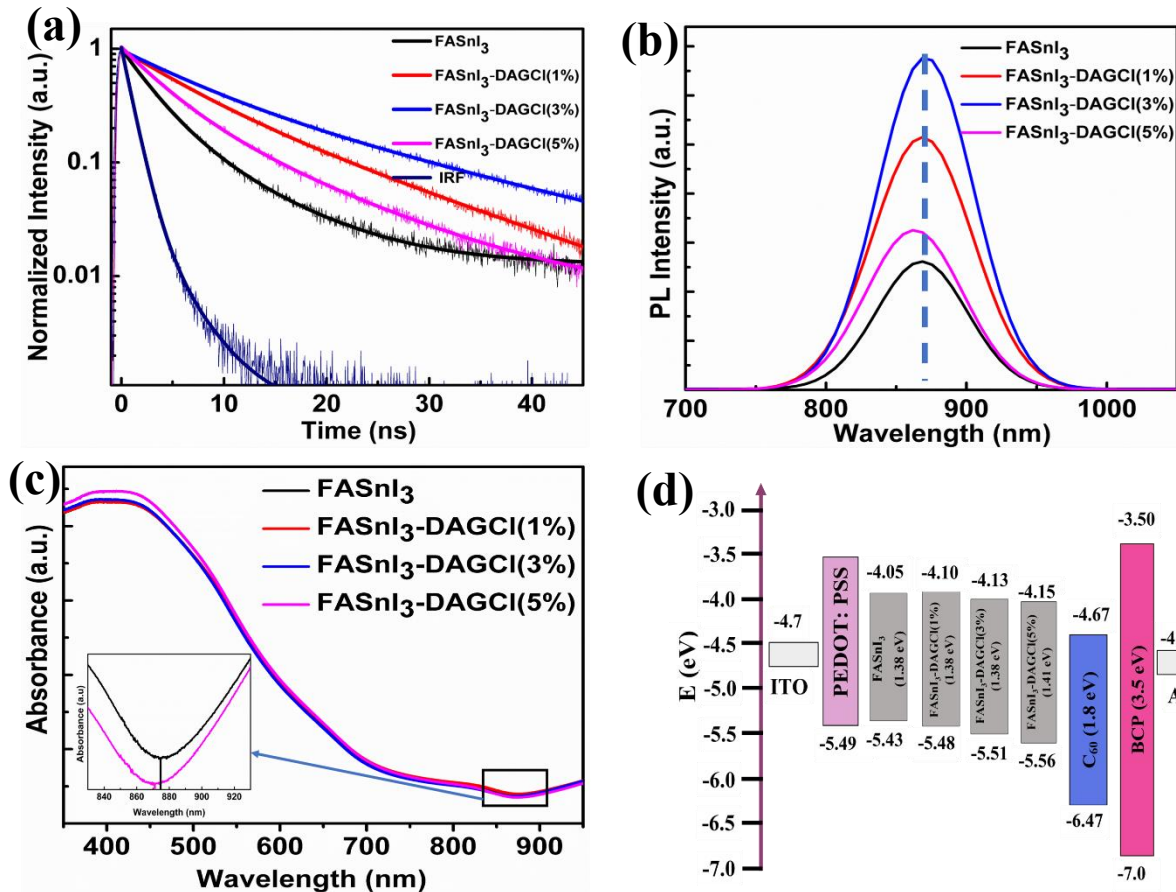**Figure 3.2-9.** (a) Normalized time-resolved photoluminescence (TRPL) spectra and (b) steady-state PL spectra of the FASnI$_3$ perovskite films fabricated on glass substrates with 0, 1, 3, and 5 mol % DAGCl. (c) UV-visible-IR spectra of the FASnI$_3$ perovskite films fabricated with 0, 1, 3, and 5 mol % DAGCl. (d) Schematic energy level diagram of the inverted planar PSCs of FASnI$_3$ without and with DAGCl.

Results and Discussion

The modified (3 mol % DAGCl) perovskite films have shown a stabilized perovskite framework, which is beneficial for the PSC performance. The stabilized perovskite structure has significantly prolonged the average charge carrier lifetime (τ_{avg}) from 5.85 ns for pristine to 15.95 ns for modified (3 mol % DAGCl) perovskite films, as shown in **Figure 3.2-9a**. The charge carrier defect states are responsible for the comparatively shorter decay lifetime of τ_1, whereas bimolecular radiative recombination is responsible for the relatively longer decay lifetime of τ_2, as shown in **Table 3.2-5.** The greatly prolonged τ_1 and τ_2 values indicate that the defect density in the bulk and on the surface of the associated perovskite film has significantly reduced, resulting in more efficient carrier transportation to the adjacent transport layer. This finding is in good agreement with the increased steady-state photoluminescence (PL) intensity seen in **Figure 3.2-9b**. The FASnI$_3$ and FASnI$_3$-DAGCl (1 and 3 mol %) films showed a PL peak at 870 nm. The emission peak was blue-shifted by adding an excess amount of DAGCl (5 mol %). This may be possibly due to the incorporation of Cl$^-$ ions into the lattice due to the higher amount of the DAGCl additive. The enhancement in the PL intensity of films with an optimal additive concentration provides compelling evidence that the defect density is efficiently decreased with suppressed nonradiative recombination in perovskite film.

Table 3.2-5. TRPL lifetime parameters from the fitting of the PL decay measurements.

Sample	τ_1(ns)	τ_2 (ns)	τ_{avg} (ns)
FASnI$_3$	2.89	7.55	5.85
FASnI$_3$-DAGCl (1%)	5.93	14.11	11.11
FASnI$_3$- DAGCl (3%)	7.24	20.58	15.95
FASnI$_3$- DAGCl (5%)	4.35	14.51	9.12

The UV-visible-IR absorption spectra of the perovskite films have been measured to understand the effect of additives on absorption, as shown in **Figure 3.2-9c.** It was demonstrated that the presence of a minimal amount (1 and 3 mol %) of DAGCl did not affect the absorption band edge. However, the modified FASnI$_3$-DAGCl (5%) film showed a slight blue shift at the absorption band edge. This indicates that the inclusion of higher amounts of DAGCl could slightly change the band gap of FASnI$_3$. Moreover, in the lower wavelength absorption spectrum, some differences were observed for FASnI$_3$-DAGCl (5%) perovskite films. The change of bang gap and absorption in the lower wavelength absorption spectrum may be possibly due to the incorporation of Cl$^-$ ions into the lattice position with an excess amount of DAGCl and a slight change in the

morphology. The band gap was determined to be ~1.38 eV for the pristine FASnI$_3$ and the modified FASnI$_3$ (1 and 3 mol % DAGCl) films and ~1.41 eV for the modified FASnI$_3$ (5 mol %) film, respectively. The changes in the band gaps are confirmed by PL spectroscopy. The energy level diagram of the PSCs is illustrated in **Figure 3.2-9d**. The PSC is based on an inverted cell architecture, and the device structure is ITO/poly(3,4-ethylenedioxythiophene) polystyrene sulfonate polystyrene sulfonate (PEDOT:PSS) (HTL)/FASnI$_3$/C$_{60}$ (ETL)/bathocuproine (BCP)/Ag, considering that the matching of the energy levels between layers is a critical factor affecting the PSC performance. The valence band maximum (VBM) values of the perovskite films were determined using an AC-3E photoelectron spectrometer. We estimated the conduction band minimum (CBM) values using the optical band gap and VBM values (**Figure 3.2-10**). Due to the suppression of Sn^{2+} oxidation, the 3 mol % DAGCl-contained perovskite film shows shallower VBM and CBM of the perovskite films, resulting in a better alignment at the HTL/perovskite interface and the perovskite/ETL interface. The VBM of the FASnI$_3$-DAGCl (3%) perovskite films were well aligned with the highest occupied molecular orbital (HOMO) level of the HTL. The reduced trap states and well-matched energy alignment accelerated the carrier transportation and hence may result in an improved V_{OC}.
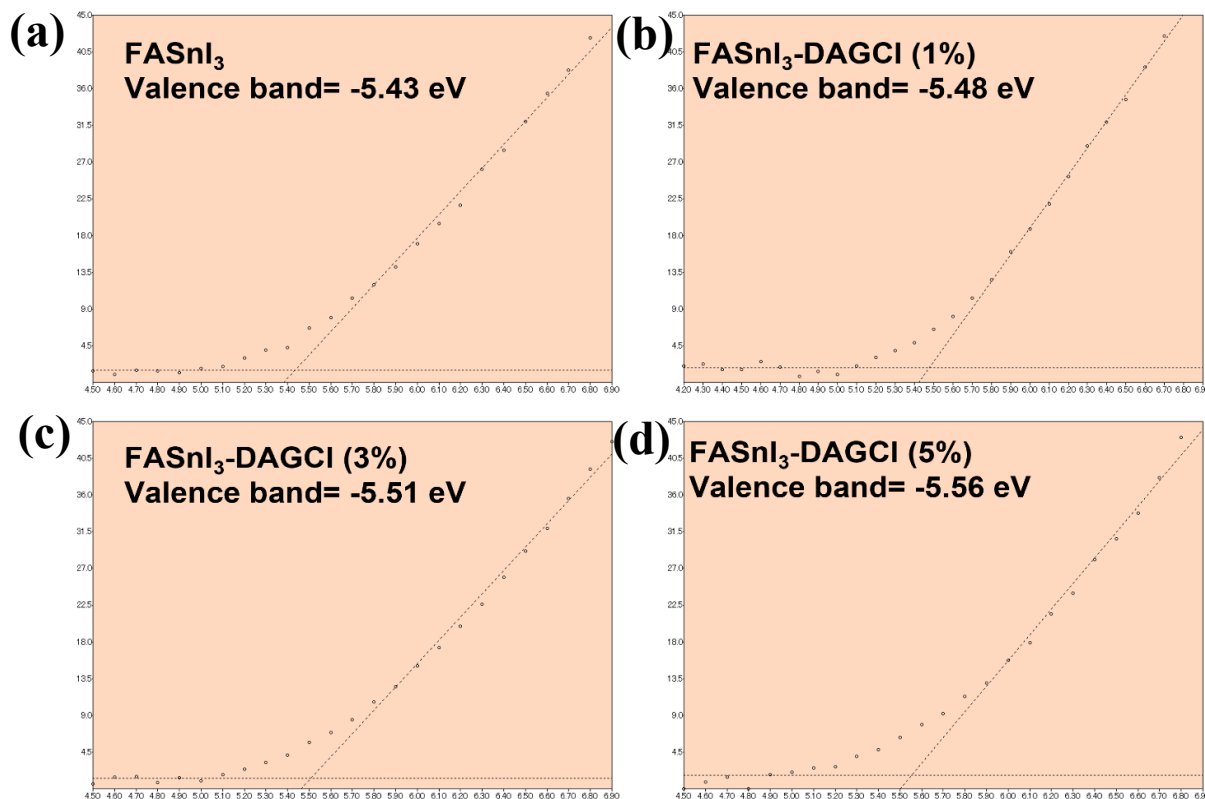

Figure 3.2-10. The photoelectron emission spectra of the perovskite films (a) FASnI$_3$, (b) FASnI$_3$-DAGCl (1%), (c) FASnI$_3$-DAGCl (3%) and (d) FASnI$_3$-DAGCl (5%).

3.2.5 Photovoltaic Performances and electron mobility

To validate the changes of modified FASnI$_3$ perovskite film properties, we fabricated PSCs with the inverted architecture of ITO/PEDOT:PSS/FASnI$_3$/C$_{60}$/BCP/Ag, as shown in **Figure 3.2-11a**. The corresponding cross-sectional SEM images of FASnI$_3$ and FASnI$_3$-DAGCl (3%) PSCs are presented in **Figure 3.2-12**. The typical current density-voltage (*J-V*) curves of the fabricated PSCs were measured under 1 sun (100 mWcm^{-1}) illuminated conditions. The *J-V* curves of the best-performing pristine and modified PSCs are shown in **Figure 3.2-11b**, and the PSC parameters are summarized in **Table 3.2-6**. The pristine PSCs displayed the best PCE of 6.04 % with a *J*$_{SC}$ of 17.60 mAcm^{-2}, a *V*$_{OC}$ of 0.50 V, and an FF of 68.6%. The FASnI$_3$ PSCs with 3 mol % DAGCl displayed a *J*$_{SC}$ of 20.18 mAcm^{-2}, a *V*$_{OC}$ of 0.61V, an FF of 72.5%, and a PCE of 8.92%. In comparison to the pristine FASnI$_3$, 1 mol % DAGCl showed a higher PCE of 7.28 %, whereas 5 mol % DAGCl exhibits a PCE of 7.53%.
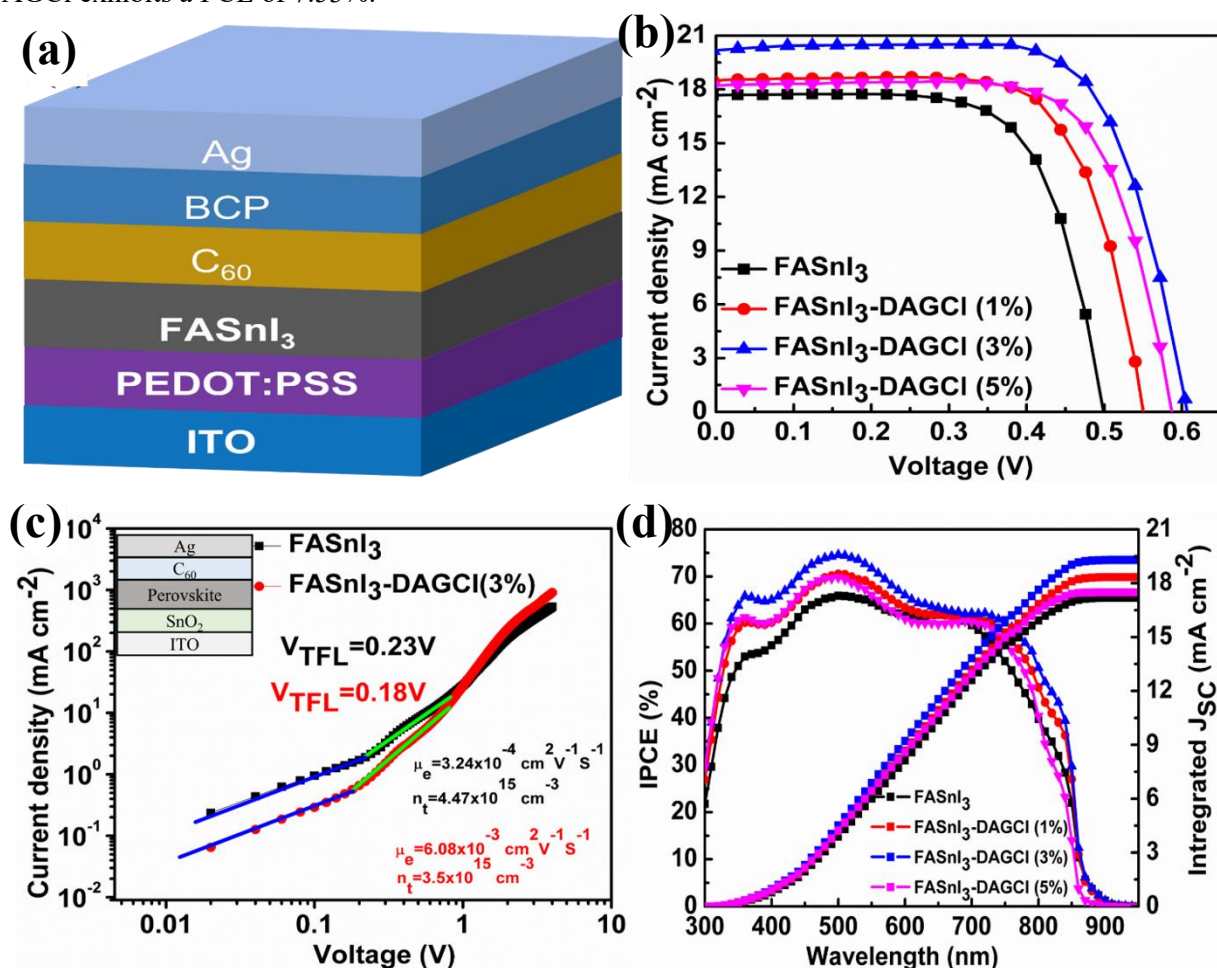

Figure 3.2-11. (a) Complete PSC structure, (b) *J-V* curves of the FASnI$_3$-based PSCs with 0, 1, 3, and 5 mol % DAGCl, respectively, (c) dark *J-V* curves of the electron-only devices fabricated with FASnI$_3$ and FASnI$_3$-DAGCl (3%), (d) IPCE of the FASnI$_3$-based PSCs with 0, 1, 3, and 5 mol % DAGCl, respectively.
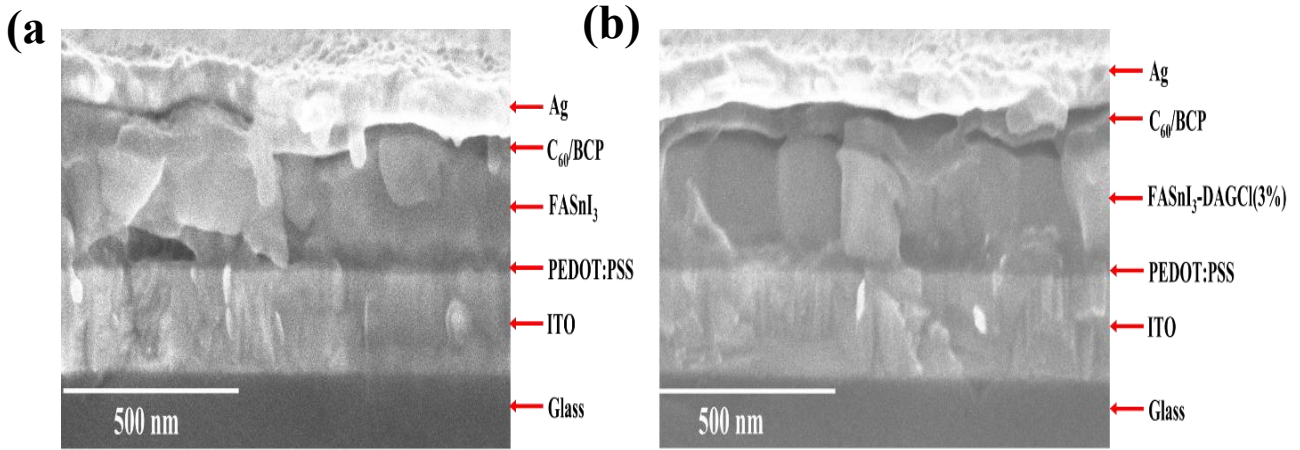
Figure 3.2-12. Cross-sectional SEM images of (a) FASnI₃, (b) FASnI₃-DAGCl (3%) based PSCs.

The improvement of PCE is contributed by the increase in the value of J_{SC}, V_{OC}, and *FF*. The enhancement of J_{SC} is mainly attributed to the improved morphology of the perovskite film with the suppressed oxidation of Sn^{2+} and I^- loss. To confirm the enhancement of J_{SC} due to the improvement of the perovskite film quality, we have examined the dark current-voltage (*J-V*) analysis of the electron-only device with a configuration of ITO/SnO₂/ FASnI₃ (without and with DAGCl)/C₆₀/Ag. Since electrons as minority carriers in the p-type FASnI₃ perovskite play a crucial role in the PSC performance, we have calculated the electron mobility (μ_e) using the following equation.

$$J= 9\varepsilon_r\varepsilon_o\mu_e V^2/8L^3$$

where, ε_r, ε_o, and V are the relative dielectric constant (5.7), the absolute dielectric constant of vacuum (8.85 × 10^{-14} Fcm^{-1}), and the voltage of the electron-only device, respectively.[94] The thickness (*L*) of the perovskite film is about 180 nm that is the same as that of the PSC device shown in **Figure 3.2-12**. The electron-only device based on FASnI₃ shows the electron mobility of 3.24 × 10^{-4} cm^2 V^{-1} s^{-1}, while FASnI₃-DAGCl (3%) exhibits a one-order higher electron mobility of 6.08 × 10^{-3} cm^2 V^{-1} s^{-1}. The increase in electron mobility after the inclusion of DAGCl additives is responsible for the increase in the J_{SC} of the PSCs. The unshared electrons from the N atom of the C=N group in DAGCl to the vacant orbital of the Sn element in the perovskite framework help to improve the electron mobility, and the hydrogen bonding stabilizes the perovskite structure by suppressing the I^- loss.

Space-charge-limited current (SCLC) analysis was used to calculate the trap-state density of the fabricated

electron-only devices based on $FASnI_3$ and $FASnI_3$-DAGCl (3%). The dark J-V curve can be divided into the ohmic region at the low bias voltage, the trap-filled region (TFL) and the child region at the high bias voltage. The kink point of the ohmic region and TFL is called trap-filled limit voltage (V_{TFL}), where all the traps are completely filled by injected carriers. The trap-state density can be calculated using the following equation.

$n_t = 2 \, \varepsilon_r \varepsilon_o V_{TFL}/qL^2$

Here, q is the elementary charge of the electron.

The estimated lower V_{TFL} of the $FASnI_3$-DAGCl (3%) based devices indicates the lower trap density of the respective device. The calculated trap-state densities of the $FASnI_3$ and $FASnI_3$-DAGCl (3%) perovskite films are 4.47×10^{15} and 3.5×10^{15} cm^{-3}, respectively. The reduced trap density indicates the higher quality of perovskite films and the efficient suppression of Sn^{2+} oxidation. The reduction of trap densities of the perovskite films could strikingly boost the value of V_{OC} and FF in PSCs. Moreover, V_{OC} enhancement is also attributed to the favourable energy level alignments of the PSCs. The achieved V_{OC} improvement was 110 mV, which was 22% higher than that of the pristine PSCs. **Figure 3.2-11** shows the monochromatic incident photocurrent conversion efficiency (IPCE) of the best-performing PSCs fabricated with $FASnI_3$ and $FASnI_3$-DAGCl (1, 3, and 5 mol %). The integrated J_{SC} values are well consistent with the obtained results from J-V curves. The PSCs with 3 mol % DAGCl have shown the highest photogenerated current.

Table 3.2-6. Photovoltaic Parameters of the $FASnI_3$-Based PSCs without and with the DAGCl Additive.

PSC		PCE (%)	J_{SC} (mA cm^{-2})	V_{OC} (V)	FF (%)
$FASnI_3$	average[a]	5.89 ± 0.29	17.55 ± 0.67	0.49 ± 0.01	67.5 ± 2.7
	best	6.04	17.60	0.50	68.6
$FASnI_3$-DAGCl(1%)	average[a]	6.99 ± 0.14	17.98 ± 0.54	0.54 ± 0.01	70.7 ± 1.6
	best	7.29	18.61	0.55	71.3
$FASnI_3$-DAGCl(3%)	average[a]	8.77 ± 0.08	20.01 ± 0.25	0.60 ± 0.01	71.5 ± 0.6
	best	8.92	20.18	0.61	72.5
$FASnI_3$-DAGCl(5%)	average[a]	7.50 ± 0.11	18.14 ± 0.30	0.57 ± 0.01	70.7 ± 0.5
	best	7.53	18.21	0.58	71.3

[a] Average of 20 PSCs.

3.2.6 Reproducibility

To further understand the effect of DAGCl on PSC performance parameters and reproducibility, we

plotted the performance parameters of 20 PSCs for each condition, as shown in **Figure 3.2-13.** The performance of the PSCs is significantly improved by the DAGCl additive, especially in terms of J_{SC}, V_{OC}, and PCE. Interestingly, the photovoltaic parameters of the fabricated PSCs showed good reproducibility, and PSCs based on FASnI$_3$-DAGCl (3%) gave the best average performance.
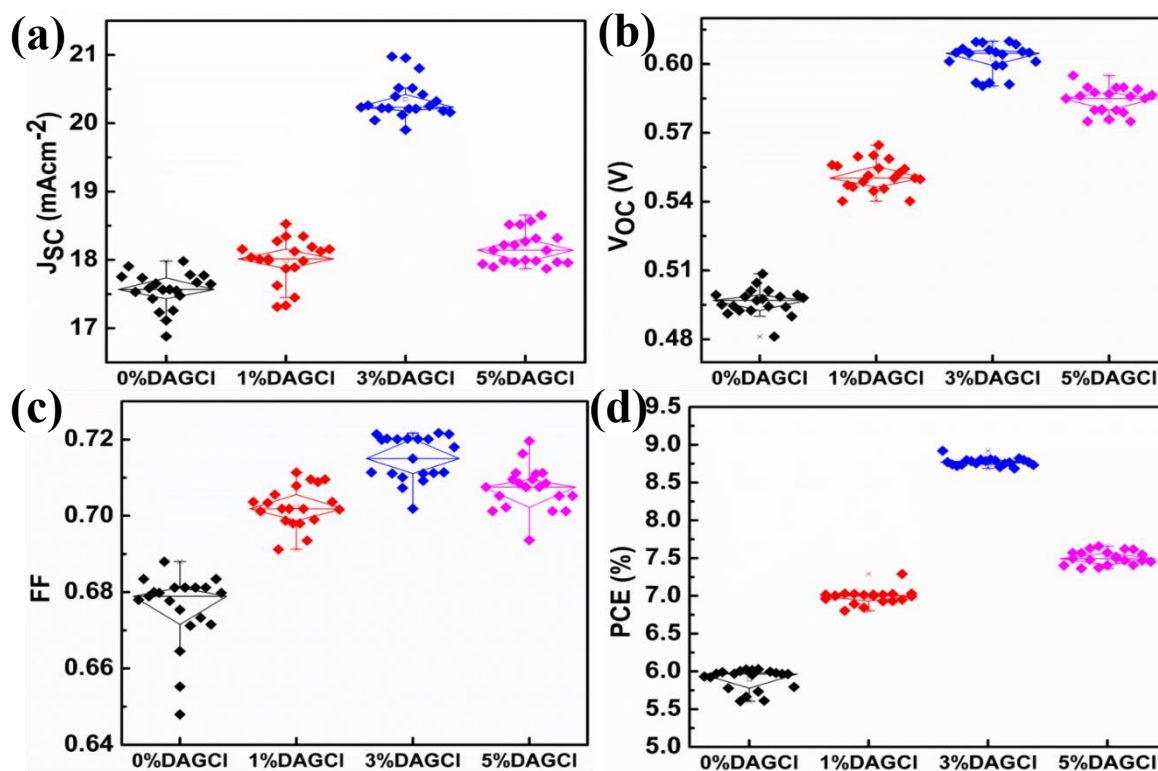

Figure 3.2-13. The statistical profiles of the (a) PCE, (b) Jsc, (c) Voc, (d) FF of the FASnI$_3$ based PSCs with 0 mol%, 1 mol%, 3 mol% and 5 mol% DAGCl, respectively.

3.2.7 Perovskite Solar Cells Properties

To gain a better understanding of the influence of DAGCl on the charge carrier transport and recombination behaviours in the fabricated PSCs, we examined the transient photovoltage (TPV) and transient photocurrent (TPC) of pristine and modified PSCs as shown in **Figure 3.2-14a, b**. The modified PSC showed a longer photovoltage decay constant of 4.50 µs than the pristine PSC (3.99 µs). This enhancement indicated that the photogenerated carrier recombination of the corresponding films was delayed, resulting in a higher V_{OC}. In contrast, the modified PSCs showed a faster TPC decay lifetime of 1.28 µs than the pristine (1.69 µs). This result confirmed that the modified films showed better charge transportation through PSCs. These advantages of the charge carrier dynamics of the modified PSCs demonstrated the defect passivation ability of

the DAGCl additive. Electrochemical impedance spectroscopy (EIS) measurements in dark conditions were also used to examine the charge carrier recombination properties of PSCs. According to the Nyquist plots, the FASnI$_3$-DAGCl (3%) based PSC has a bigger semicircle, indicating a higher recombination resistance (R_{rec}) than the pristine PSC, as shown in **Figure 3.2-14c**. The higher R_{rec} for the modified PSC means that the DAGCl additive suppresses the charge carrier recombination and leads to faster charge transportation through the PSCs. Additionally, we examined the dark *J-V* analysis to elucidate the intrinsic properties of the PSCs, as shown in **Figure 3.2-14d**. It is noticeable that the modified PSC has shown a lower leakage current than the pristine PSC. The lower leakage current of the modified PSC means a lower trap density, a reduction of background carrier density, and enhanced charge transportation. This result is consistent with the TPV and TPC analysis for the DAGCl passivation effect.
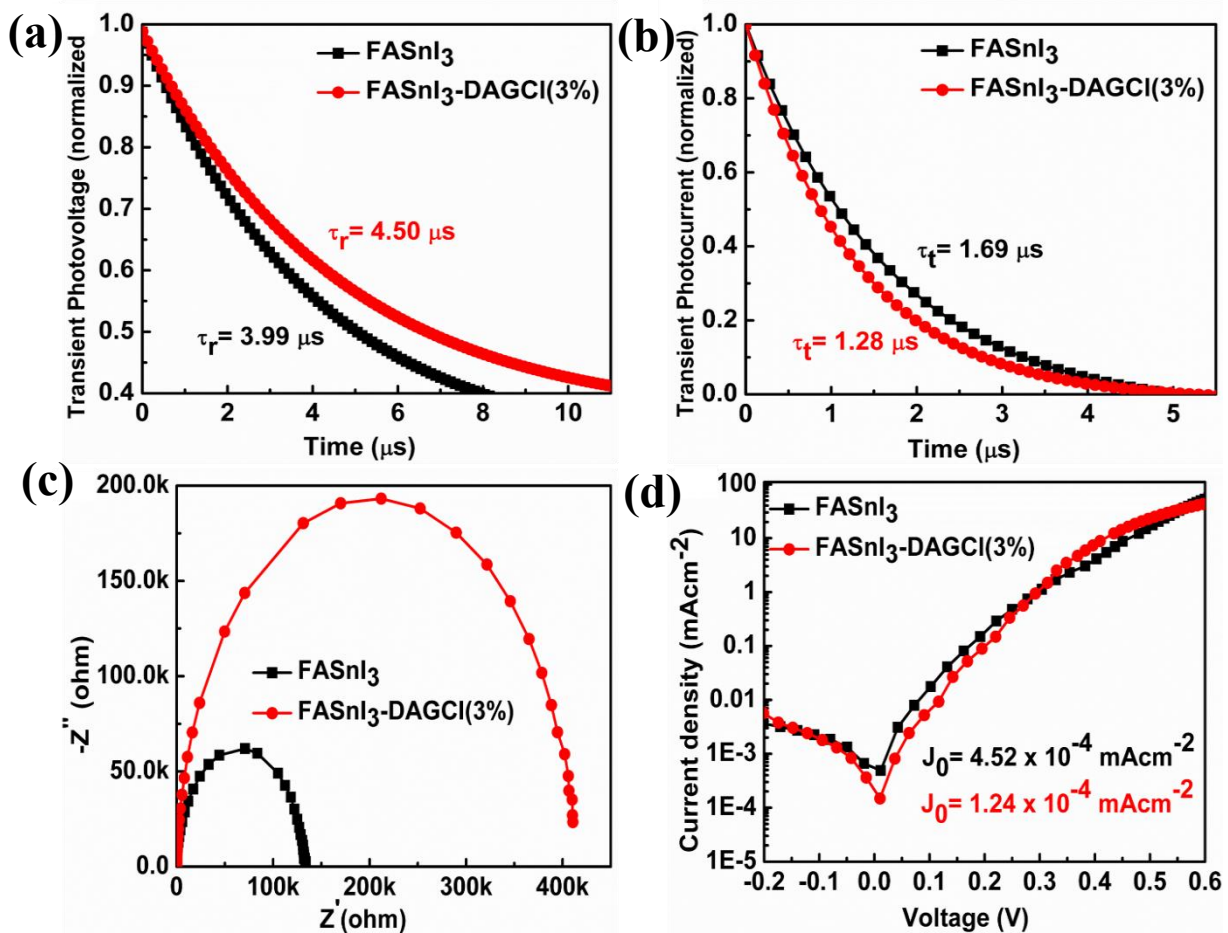

Figure 3.2-14. (a) Transient photovoltage decay, (b) transient photocurrent decay, (c) Nyquist plot measured under dark conditions, (d) dark J-V curves.
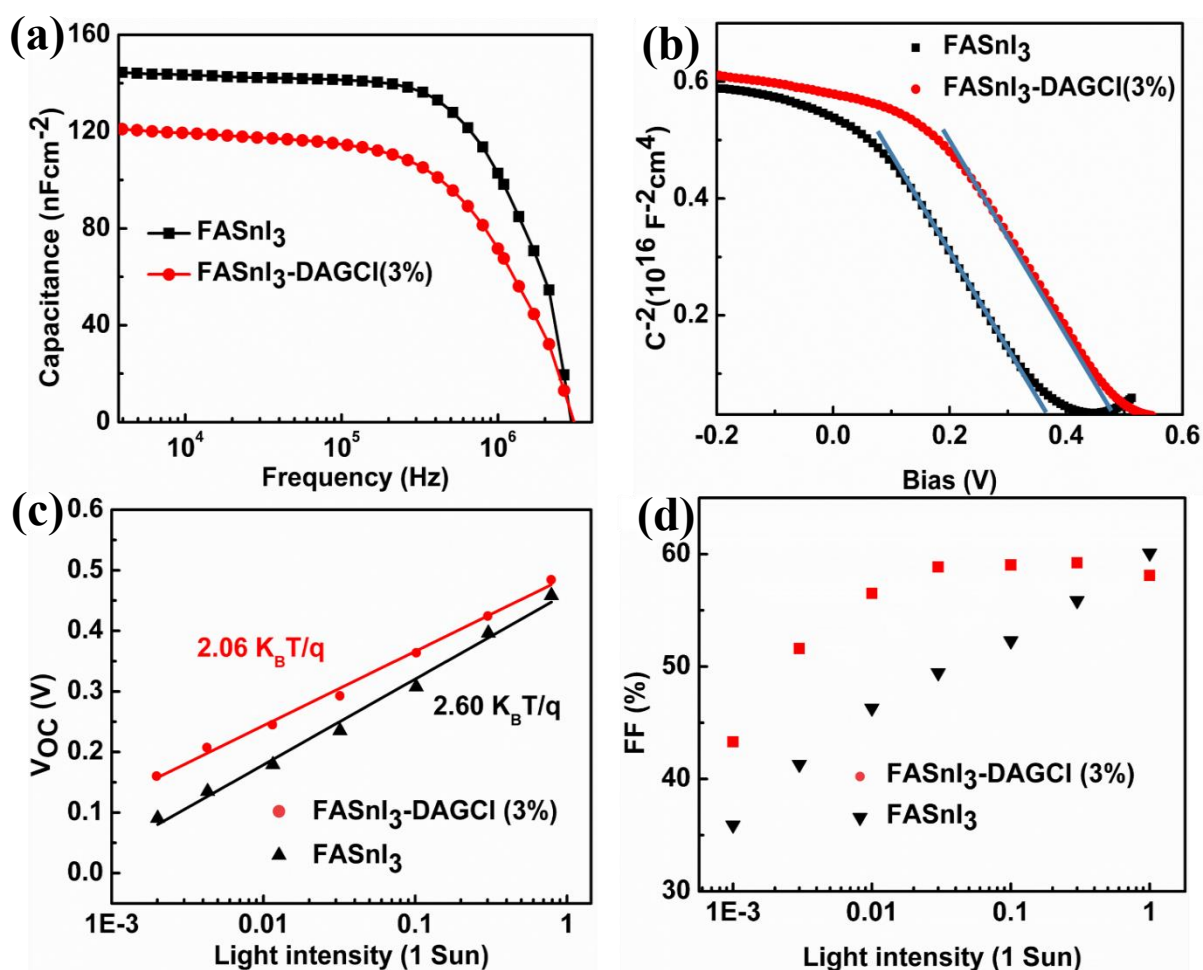
Figure 3.2-15. (a) Admittance spectra, and (b) Mott-Schottky profiles of the FASnI$_3$ and FASnI$_3$-DAGCl (3 mol%)-based PSCs. Light intensity dependency of (c) V_{OC} and (d) FF of FASnI$_3$ and FASnI$_3$-DAGCl (3%) based PSCs.

Further, we gain a deeper knowledge of defect densities and a probable reason for the V_{OC} enhancement by capacitance characteristics of the PSCs. We have examined the PSCs for pristine FASnI$_3$ and modified FASnI$_3$-DAGCl (3%) to understand the capacitance (C) response with the charge carrier distribution, i.e., free carrier and trap densities, as shown in **Figure 3.2-15a**. The values of C reflect the number of charge carriers trapped at the defect states of the absorber layer and interfaces of the PSCs. The C at the lower-frequency region indicates the existence of the electronic trap state in both PSCs. The lowered C value for the modified PSC than the pristine PSC all over the range implies that the DAGCl additive can reduce the electronic trap states of the perovskite absorber layer and the interfaces of PSCs. The higher C all over the frequency range for pristine suggests a higher trap density inside PSCs. For Mott-Schottky profiles, as shown in **Figure 3.2-15b**,

we have calculated the built-in potential (V_{bi}). The larger V_{bi} is beneficial for charge carrier separation, transportation, and extraction. The modified PSC had a greater V_{bi} ($\sim$ 0.48 V) than the pristine PSC ($\sim$ 0.36 V). The existence of a greater electric field at the interfaces, as indicated by a higher V_{bi}, allows effective charge transfer via the interfaces. The higher V_{bi} facilitates the enhancement of V_{OC}.

To elucidate the charge recombination kinetics during solar cell operation, we analyzed V_{OC} and FF as a function of light intensity for pristine and modified PSCs. **Figure 3.2-15c** illustrates the light intensity dependency of V_{OC} for PSCs without and with DAGCl. The relation of V_{OC} with the light intensity can be written as $V_{OC} = (nk_BT/q)$ In (I/I+1), where n is the ideality factor, q is the elementary charge, k_B is the Boltzmann constant, and T is the temperature. In an ideal case of the device, the ideality factor is close to 1 which suggests radiative recombination. While the value is close to 2, it indicates nonradiative recombination mainly through traps or defects within the device. After linear fitting of the plot of V_{OC} vs semilogarithmic light intensity, we had a slope of 2.60 k_BT/q and 2.06 k_BT/q for the pristine and modified PSCs, respectively. The lower value of the slope indicates the suppression of trap-assisted Shockley-Read-Hall (SRH) recombination of the modified PSC under open-circuit conditions. This could be due to the higher crystalline perovskite films than pristine with more effective electronic defect passivation. The light intensity dependence of FF for pristine and modified PSCs is shown in **Figure 3.2-15d**. The FF is associated with trap filling and bimolecular recombination, occurring at a low density and at a high density of photogenerated carriers, respectively. In the case of the FASnI$_3$-DAGCl (3%) based PSC, the value of FF increases initially up to 3 mWcm^{-2} and then remains almost constant at a higher intensity of light. This trend indicates the reduction of trap-assisted recombination in the PSC and expects better FF at a lower carrier density (lower light intensity). On the other hand, the FF increased gradually with increasing light intensity up to 1 sun condition for the pristine PSC. This behaviour suggested that more photogenerated charge carriers are needed to fill the traps to suppress trap-assisted recombination.

We examined the stability of the fabricated PSCs based on FASnI$_3$ and FASnI$_3$-DAGCl (3%). The PSCs were stored inside an N$_2$ glovebox and tested the stability over time. The FASnI$_3$-based PSC decreased by about 45% of the original PCE after 1100 h, as shown in **Figure 3.2-16a**. In comparison, the FASnI$_3$-DAGCl (3%) based PSC retained about 95% of the original PCE after 1100 h. Most importantly, we tested encapsulated

PSCs (**Figure 3.2-17**) under continuous light illumination (1 sun condition) at room temperature. The FASnI$_3$-based PSC degraded much faster at continuous light soaking, whereas the FASnI$_3$-DAGCl (3%) based PSC retained PCE of 65% after 400 h under continuous light soaking (**Figure 3.2-16b**). Such stability under light soaking indicates the good quality and lower anionic vacancies of the respective perovskite films.
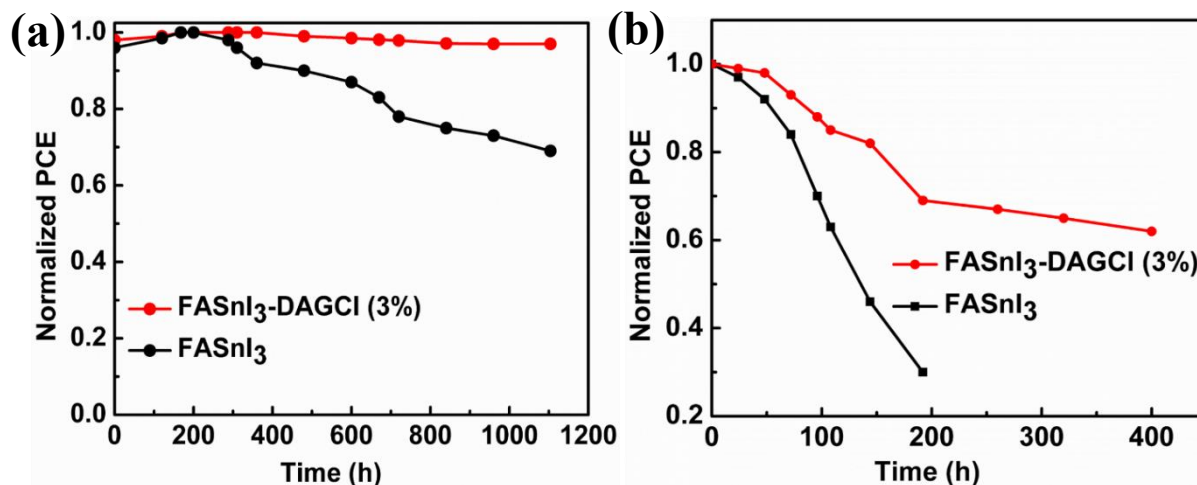

Figure 3.2-16. (a) Shelf-life stability of FASnI$_3$ and FASnI$_3$-DAGCl (3%)-based PSCs in an N$_2$-filled glovebox and (b) light-soaking stability of FASnI$_3$ and FASnI$_3$-DAGCl (3%)-based encapsulated PSCs under 1 sun (100 mWcm^{-1}) illumination of the MPPT system (**Figure 3.2-17**).
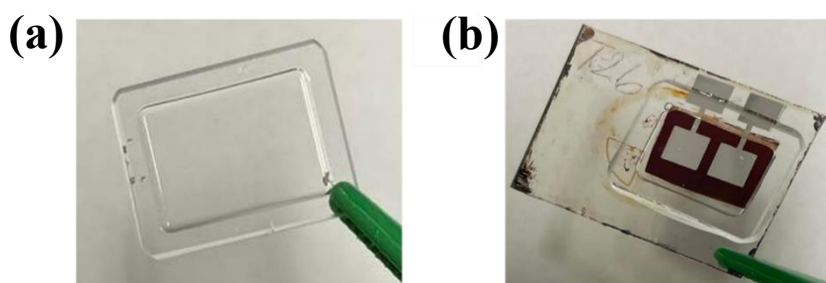

Figure 3.2-17. (a) Cavity glass, (b) Encapsulated Sn-PSC.

We introduced the bulky guanidine-based additive 1,3-diaminoguanidine monohydrochloride (DAGCl) into a Sn perovskite to improve the perovskite crystallization and passivate the electronic defects. The amino groups of the bifunctional DAGCl formed hydrogen bonding with iodide in the FASnI$_3$ framework and suppressed the losses of I$^-$. The Cl$^-$formed covalent bonds with undercoordinated Sn^{2+} ions and improved the crystallinity with a stabilized FASnI$_3$ perovskite structure and retarded the Sn^{2+} oxidation. This dual aspect of the DAGCl additive simultaneously affects the fabrication process, enhances electron mobility, and reduces

Results and Discussion

trap density. The modified PSC (3% mol DAGCl) showed a PCE of 8.92% with a significantly improved V_{OC} of up to 0.61 V. The enhancement of V_{OC} is about 110 mV compared to the pristine PSC (0.50 V) due to the improved perovskite film quality and the well-matched energy band diagram with the adjacent transport layer. Moreover, the modified PSC retained 95% of its initial PCE after 1100 h and showed stability during continuous light soaking.

3.3 Inhibition of Sn^{2+} Oxidation in FASnI₃ Perovskite Precursor Solution and Enhanced Stability of Sn-Based Perovskite Solar Cells by Multifunctional Additive

Results and Discussion

3.3.1 Interaction of 4-fluorophenylhydrazine Hydrochloride with Perovskite Precursor Solution

The solution process prepared Sn-based perovskite used precursor solution, and the fabricated films quality always depends on the properties of precursor solutions. Due to the fast crystallization and easy oxidation of free Sn^{2+} ions in commonly used solvent DMSO, the fabricated films always form voids and pinholes and generate several various defects (Sn vacancy and I vacancy). It is reported that the I ions (I^-) in the precursor solution could produce ionic accumulation to generate I_2 due to the volatilization of DMSO and weak van der Waals-type interaction between SnI_2 and DMSO.[75] To solve above mentioned problems, the 4-fluorophenylhydrazine hydrochloride (4F-PHCl) is introduced in the $FASnI_3$ perovskite precursor solution.
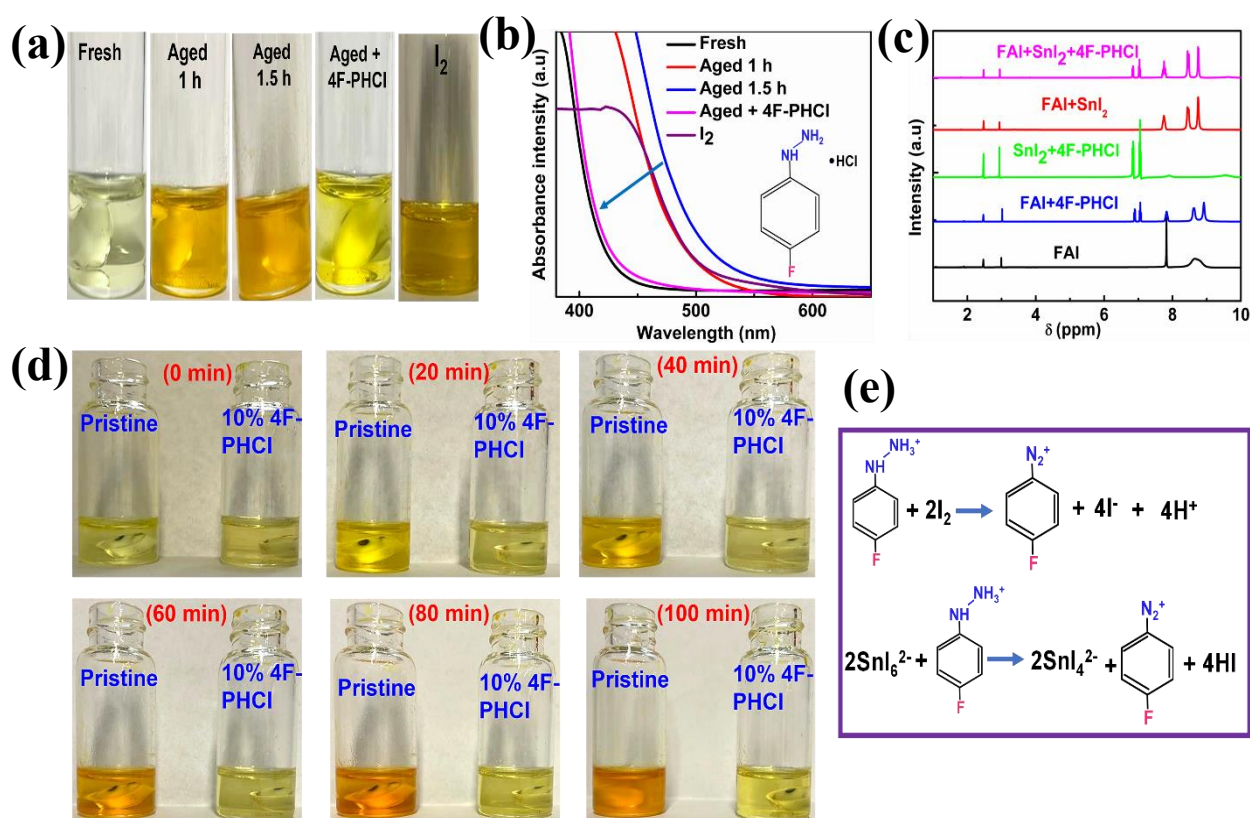

Figure 3.3-1. (a) Photographs of SnI_2 solution, aged SnI_2 solution, aged SnI_2+4F-PHCl solution and I_2 solution in DMSO solvent. (b) Ultraviolet (UV)-visible absorption spectra of solution in Figure 1a. (c) ^1H NMR spectra of FAI, FAI+4F-PHCl, SnI_2+4F-PHCl, FAI+SnI_2, and FAI+SnI_2+4F-PHCl in DMSO-d_6 solution. (d) Photographic images of pristine and 10 % 4F-PHCl modified $FASnI_3$ precursor solution in air for different period of time. (e) Possible chemical reactions for I_2 and Sn^{4+} defects back to I^- and Sn^{2+}.

To justify the oxidation of I^- to I_2/I_3^- in the precursor solution, we first prepared the solution of SnI_2 in DMSO and placed it in an ambient environment at 30% relative humidity. The color of the SnI_2 solution turns

deddish yellow after aging, disclosing that the I⁻ in the SnI$_2$ solution is oxidized to I⁻/I$_3$⁻ during the aging process, as shown in **Figure 3.3-1a**. The characterizing UV-vis absorption edge of I$_2$ or I$_3$⁻ was shifted to a longer wavelength after the SnI$_2$ solution was aged, as shown in **Figure 3.3-1b**. After adding 4F-PHCl into the aged SnI$_2$ solution, the absorption edge turns to a shorter wavelength again, validating that the hydrazine group containing 4F-PHCl additive could effectively reduce the I$_2$/I$_3$⁻ defects and restore them to I⁻. This finding indicates that the 4F-PHCl can interact with SnI$_2$ and significantly suppress the oxidation of I⁻ in the precursor solution and maintain the properties of a solution. To confirm the interaction of 4F-PHCl with SnI$_2$ and the formation of coordination bond, we examined the Fourier transform infrared (FTIR) spectra for SnI$_2$ powder, 4F-PHCl powder, SnI$_2$-DMSO adduct, and SnI$_2$-4F-PHCl adduct, as shown in **Figure 3.3-2a**. Powdered 4F-PHCl has a characteristic absorption at 3206 cm^{-1}, which corresponds to the stretching vibration frequencies of the N-H group based on FTIR analysis. The peak was shifted to lower wavenumbers at 3183 cm^{-1} after interaction with SnI$_2$. This shift could be related to the formation of coordination bonds by 4F-PHCl with SnI$_2$.[84] In addition, the color of the 4F-PHCl additive turned reddish yellow from brown after interaction with SnI$_2$, as shown in **Figure 3.3-2b.**
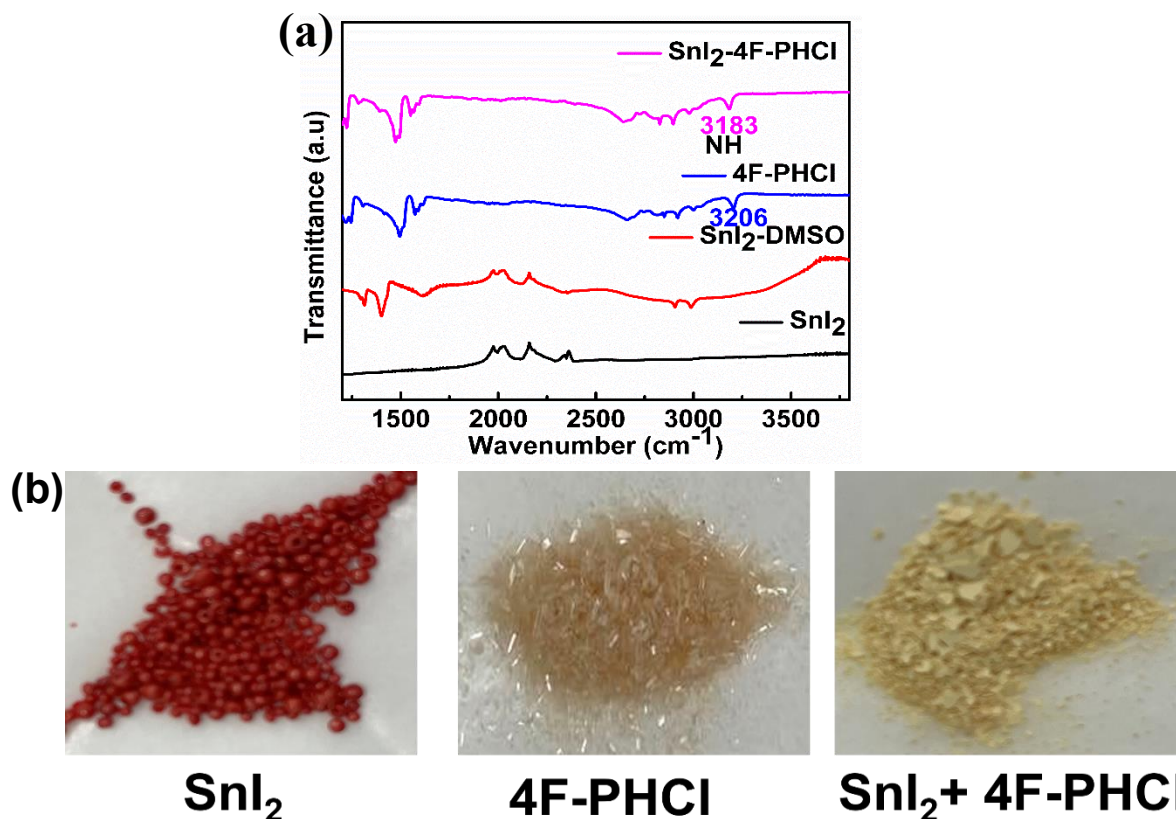

Figure 3.3-2. (a) FTIR spectra of SnI$_2$ powder, SnI$_2$-DMSO adduct, 4F-PHCl powder, and SnI$_2$-4F-PHCl adduct. (b) Pictorial presentation of SnI$_2$ powder, 4F-PHCl powder and SnI$_2$-4F-PHCl adduct powder.

Results and Discussion

We performed the liquid-state photon nuclear magnetic resonance (^{1}H NMR) spectra of FAI, FAI+4F-PHCl, SnI$_2$+4F-PHCl, FAI+SnI$_2$, and FAI+SnI$_2$+4F-PHCl in deuterated dimethyl sulfoxide-d_6 (DMSO- d_6) solution, as shown in **Figure 3.3-1c**. Proton resonance peaks at 7.78, 8.46, and 8.76 ppm in FAI+SnI$_2$ ^{1}H NMR spectra have been attributed to CH$_2$, NH$_2$, and NH$_3$ for FA, respectively. However, when 4F-PHCl was introduced into the FAI+SnI$_2$ solution, two new peaks formed at 6.87 ppm and 7.07 ppm. Those two peaks were in addition to the three peaks that were mentioned earlier. Based on these findings, we decided to come up with the assumption that the end groups of 4F-PHCl that contain ammonium (NH$_3$$^+$) undergo a hydrogen bond (-N−H···I) interaction with iodide originating from [SnI$_6$]$^{4-}$ octahedra.
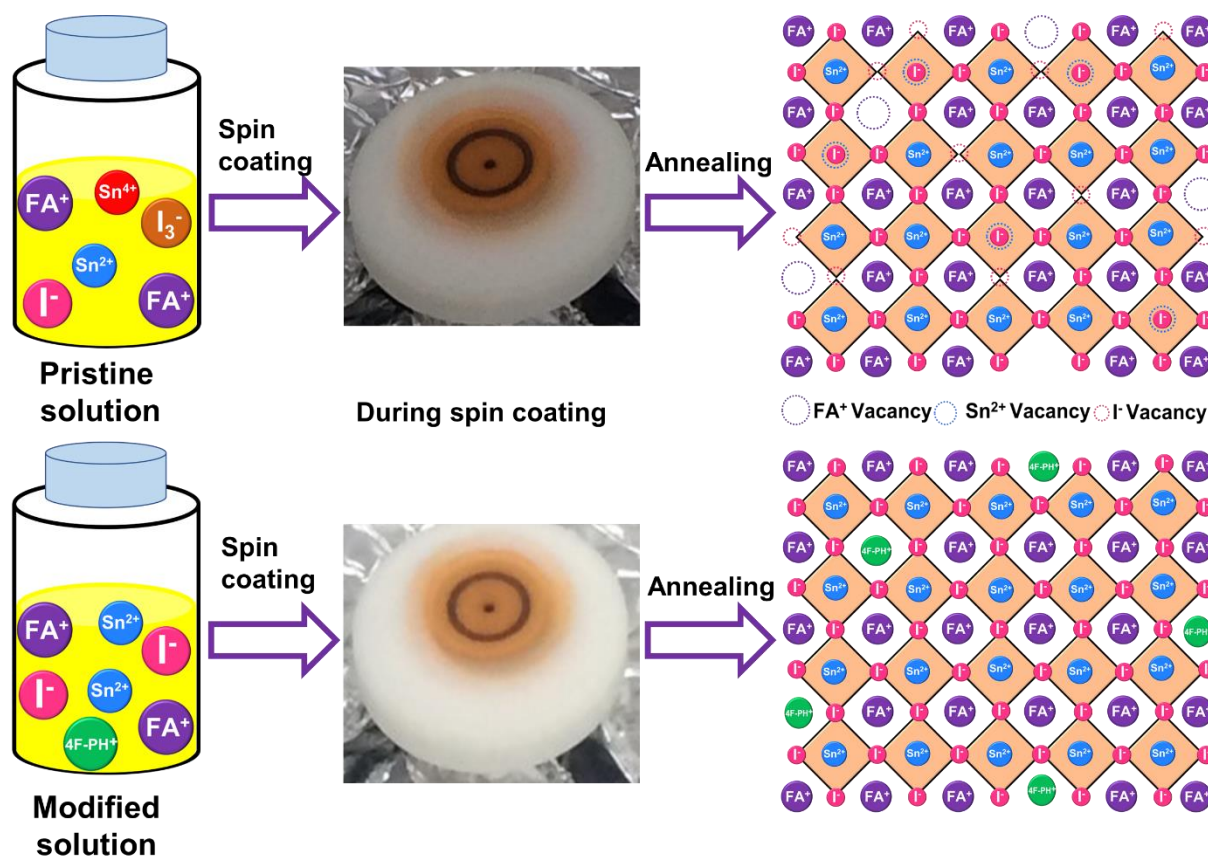

Figure 3.3-3. Schematic illustration of crystallization process of pristine and 10% 4F-PHCl modified films.

The ultimate outcome of these strong interactions is a stable precursor solution that will effectively prevent oxidation involving Sn^{2+} and DMSO. To accomplish this goal, a fresh solution of FASnI$_3$ with and without 4F-PHCl is prepared and exposed to the precursor solution in the air at a relative humidity of 40%, as illustrated in **Figure 3.3-1d**. At first, the color of both precursor solutions was similar to that of a light yellow. After being exposed for 100 minutes in the ambient air, the pristine perovskite precursor solution changes color to a

reddish darken, indicating the oxidation of Sn^{2+} to Sn^{4+} by DMSO.[34] On the other hand, adding 4F-PHCl in

the precursor solution of FASnI$_3$ maintains almost the initial color indicating it the strongly protected from the

Sn^{2+} oxidation and maintains the precursor solution characteristics properties. According to this study, the

incorporation of 4F-PHCl into the precursor solution enhances the solution stability with inhabited the Sn^{2+}

oxidation by DMSO. The possible chemical reaction for restoring the I$_2$ and Sn^{4+} defects back to me$^-$ and Sn^{2+}

is shown in **Figure 3.3-1e**. The crystallization process of pristine and modified perovskite films is

schematically illustrated in **Figure 3.3-3**.

To confirm the chemical interaction between perovskite and 4F-PHCl, we examined the X-ray

photoelectron spectroscopy (XPS) measurement. In **Figure 3.3-4**, the characteristic peaks of C 1s and N 1s

from FA$^+$ move to lower binding energy. This result indicates the electron-rice environment on the perovskite

matrix due to the electron-doner effect of phenyl-containing 4F-PHCl additive.
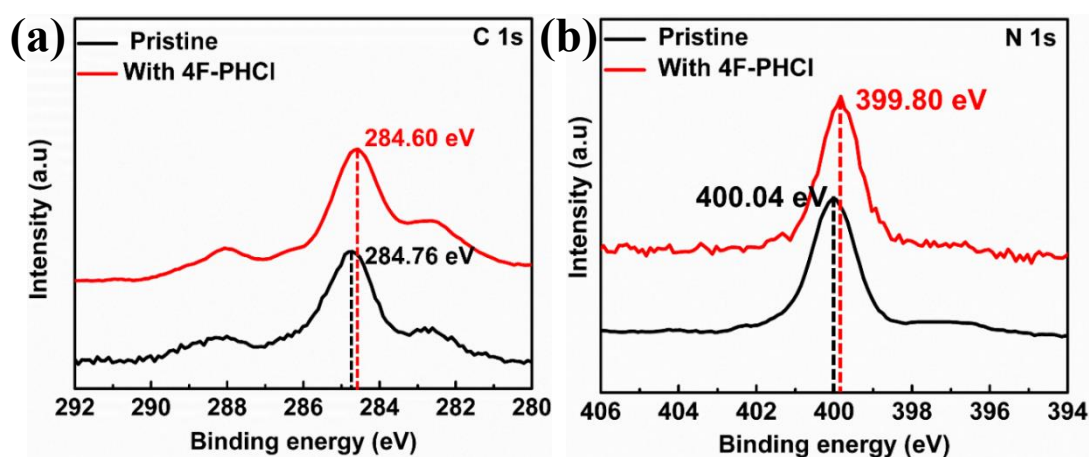

Figure 3.3-4. The XPS spectra of (a) C 1s and (b) N 1s.

3.3.2 Morphology and Crystallinity of the Perovskite Films

Scanning electron microscopy (SEM) measurements have been explored to evaluate the 4F-PHCl additive

impact on the nucleation and crystallization processes. Perovskite films were deposited on indium tin oxide

(ITO) substrates coated with poly (3,4 ethylenedioxythiophene: poly(styrenesulfonate) (PEDOT: PSS),

followed by thermal annealing. As seen in **Figure 3.3-5**, the addition of 4F-PHCl has a positive effect on the

crystallization process of 3D FASnI$_3$ perovskite. With the addition of 4F-PHCl additive in the precursor

solution, the crystal grain size of the films changes to become progressively smooth and larger. We found that

the pristine perovskite has a narrow grain size distribution and has an average grain size (D_{av}) of 270 nm with

a standard deviation of 59 nm, as shown in **Figure 3.3-6**. Perovskite films with 10% 4F-PHCl content have a large average grain size of 520 nm with a standard deviation of 80 nm.
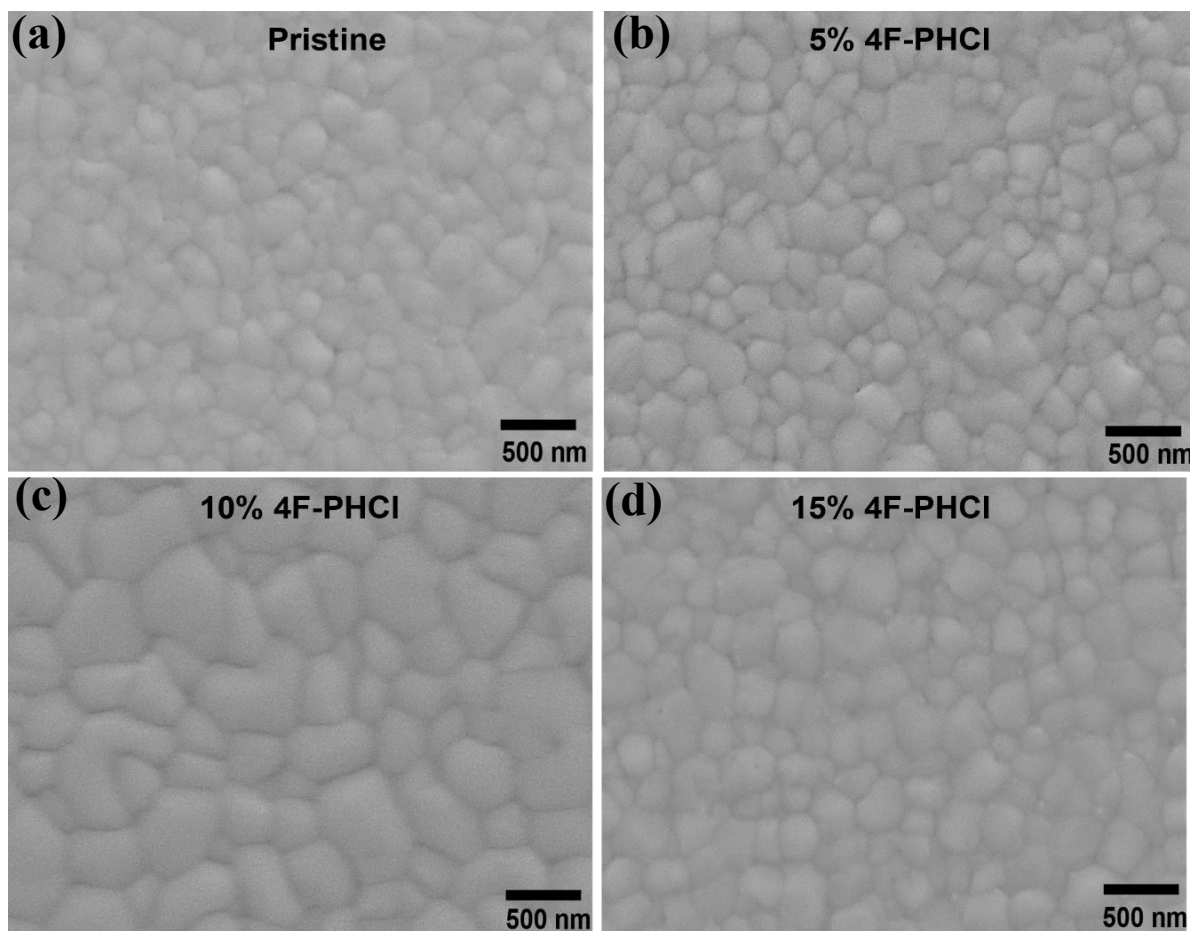

Figure 3.3-5. SEM images of the (a) pristine, (b) 5% 4F-PHCl, (c) 10% 4F-PHCl, and (d) 15% 4F-PHCl-modified $FASnI_3$ perovskite films.

We noticed that the grain size increased up to a concentration of 10% 4F-PHCl, but after that, at a concentration of 15 % 4F-PHCl, the grain size began to decline. In spite of the fact that the grain size range is rather large in all 4F-PHCl-contained perovskites film, the total grain size is much larger than in pristine perovskite films (**Figure 3.3-6**). The cross-sectional SEM images of pristine and 10% 4F-PHCl modified perovskite are shown in **Figure 3.3-7**. The modified perovskite film is almost composed of grain, and pristine perovskite has a less aligned grain. From top view SEM and cross-sectional SEM, it may conclude that the 10% 4F-PHCl modified perovskite has denser and more compact grain at the surface and bulk. Perovskite films with large grains may have resulted from additive-induced nucleation of perovskite films. Additive 4F-PHCl plays three roles in enhancing the perovskite film quality. First, it maintains the precursor solution properties by detrimental I_2

Results and Discussion

defects back to I⁻ and suppresses the Sn^{2+} oxidation in the precursor solution. Second, the 4F-PHCl additive makes coordination with $[SnX_6]^{4-}$ in the perovskite lattice by hydrogen bond (-N−H···X). The interaction leads to slowing down the crystallization process (**Figure 3.3-8**) and reduces the number of nucleation sites and sluggishness in the pace of crystallization. Third, 4F-PH⁺ cations could be taken place in the vacant position of FA⁺.

Figure 3.3-6. The graine size distribution of (a) pristine, (b) 5% 4F-PHCl, (c) 10% 4F-PHCl and (d) 51% 4F-PHCl-modified FASnI₃ perovskite film, respectively. Grain size (total 100 for each case) calculated by ImageJ software.

To verify the inclusion of 4F-PH⁺ into the crystal lattice, we evaluated the X-ray diffraction (XRD) analysis of the pristine and 4F-PHCl containing perovskite films. The perovskite films were prepared using FASnI₃ precursor solution with varying molar ratios of 4F-PHCl (0%, 5%, 10%, and 15%). As illustrated in **Figure**

3.3-9, all the films have shown the dominant diffraction peaks at 14.1°, 24.4°,28.2°, and 31.6° can be ascribed to the (100), (102), (200), and (122) orthorhombic lattice (*Amm2*) crystal planes of the $FASnI_3$ perovskite, respectively. In addition, the intensity of diffraction peaks corresponding to the [100] plane is significantly enhanced with the addition of 4F-PHCl, which suggests that the introduction of 4F-PHCl in perovskite precursor solution is beneficial for improving the crystalline quality of the fabricated perovskite film. However, diffraction angles gradually shift to a lower angle with increasing the amount of 4F-PHCl, indicating that 4F-PH$^+$ is incorporated into the $FASnI_3$ perovskite crystal lattice. Fortunately, no diffraction peaks have arisen in the lower angle, indicating no dimensional reduction happens after the inclusion of 4F-PH$^+$ in the 3D $FASnI_3$ perovskite crystal lattice.

Figure 3.3-7. Cross-sectional SEM images of (a) pristine and (b) 10% 4F-PHCl modified PSCs.

Figure 3.3-8. Pictorial presentation of crystallization process during spin coating process.

Figure 3.3-9. XRD patterns of the pristine and 4F-PHCl modified perovskite films.

3.3.3 XPS Analysis for Sn and I Defects

Figure 3.3-10. High-resolution XPS spectra of pristine and 4F-PHCl modified perovskite films for (a, b, c and d) Sn $3d_{5/2}$ and (e, f, g and h) I $3d_{5/2}$, respectively. (i) Stoichiometric ratio of Sn^{2+}/I^- for corresponding films.

Results and Discussion

The perovskite films are prepared by spin-coating process and then annealed for full crystallization. During the spin-coating, while volatile DMSO leaves the film due to weakly bonded with SnI_2 layer space by van der Waals-type interaction, the fast crystallization is attributed to the lower quality of films. After the inclusion of 4F-PHCl in the perovskite precursor solution, the crystallization kineties have changed and slowed down the nucleation process by a hydrogen bond (-N−H···X) formed between the ammonium group in 4F-PH^+ and I^-/Cl^- in $[SnX_6]^{4-}$ framework of perovskite matrix. This 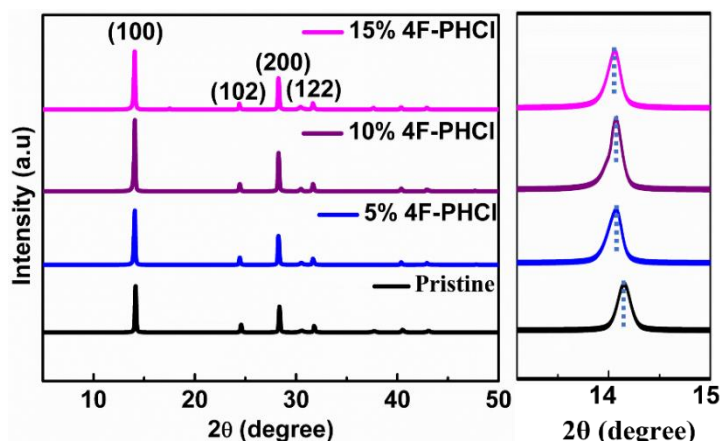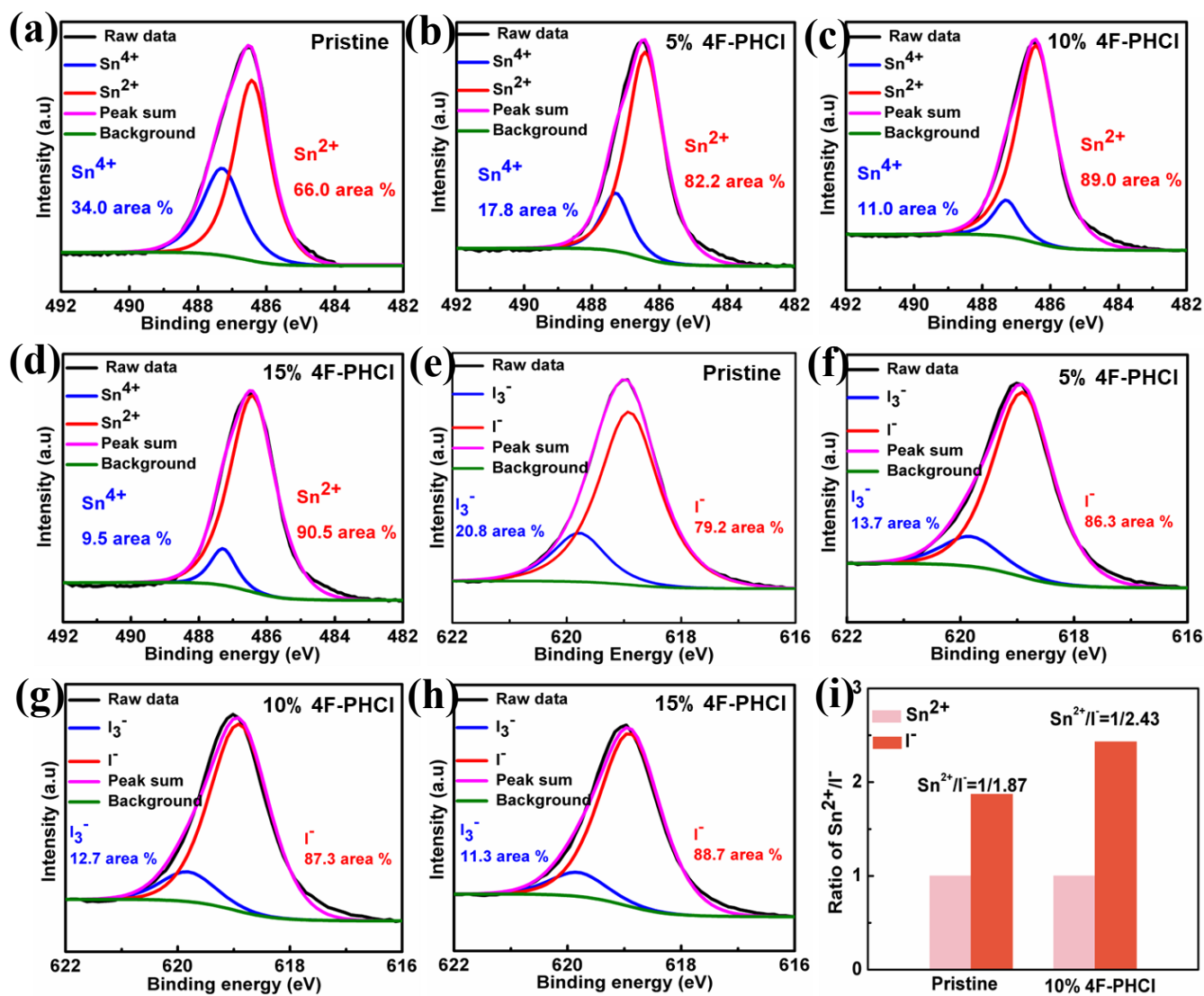type of interaction inhabited the oxidation of Sn^{2+} to Sn^{4+}, and I^- ions to I_2 or I_3^-, which would reduce the Sn and I defects on top of the surface of the films. These defects make it easier to produce major deep-level traps, which results in nonradiative recombination loss.[95] To quantify the Sn and I defects in perovskite films, we conducted the XPS on these films. As demonstrated in **Figure 3.3-10a, b, c, d,** the Sn 3d area showed two distinct peaks, one at 486.42 eV and the other at 487.29 eV. These peaks may be attributed to the binding energy of the Sn^{2+} atom in the perovskite structure and the oxidized Sn^{4+} atom on the surface of the film, respectively. We observed the reduced atomic percentage of Sn^{4+} for the 10% 4F-PHCl containing perovskite films as compared to pristine film. The modified films showed the remarkably suppressed Sn^{4+} content of 34.0% of the pristine film to 11.0% of 10% 4F-PHCl modified films.

Table 3.3-1. The fitting results of XPS spectra for the pristine and 10% 4F-PHCl modified $FASnI_3$ films.

Sample FASnI₃	Sn $3d_{5/2}$		I $3d_{5/2}$		Stoichiometric ratio of Sn^{2+} and I^-
	Sn^{2+}	Sn^{4+}	I^-	I_3^-	
Area	7755	3995	14555	3809	**1:1.87**
10% 4F-PHCl	Sn $3d_{5/2}$		I $3d_{5/2}$		
	Sn^{2+}	Sn^{4+}	I^-	I_3^-	
Area	11125	1375	27033	3932	**1:2.43**

In terms of I defects, the pristine films possess a percentage of I^- up to 79.2% is lower than 10% 4F-PHCl modified film (87.3%), as shown in **Figure 3.3-10e, f, g, h**. Interestingly, the ratio of I_3^-/I in the pristine film is 20.8%, while this ratio of 10% 4F-PHCl modified films is 12.7%. The lower ratio of I_3^-/I for 10% 4F-PHCl modified film indicates the higher quality of films with less amount of I_3^- on top of the perovskite surface.

Results and Discussion

From the XPS analysis, it is confirmed that the incorporation of 4F-PHCl in FASnI$_3$ perovskite precursor solution is beneficial and significantly suppressed the loss of Sn^{2+} and I$^-$. This suppression maintains the stoichiometric ratio of Sn^{2+}/I$^-$ is 1: 2.43 (theoretical value is 1:3), while the ratio of pristine is 1:87, as shown in **Figure 3.3-10i**. The details information of XPS analysis for pristine and 10% 4F-PHCl modified film is demonstrated in **Table 3.3-1.** Moreover, the contact angle measurements were conducted to evaluate the hydrophobicity of both the pristine film and 10% 4F-PHCl modified film.

3.3.4   Water Contact Angle

As demonstrated in **Figure 3.3-11,** the water contact angle of the modified film was increased from 58.8° to 76.2°. This indicated that the inclusion of 4F-PHCl in perovskite resulted in an enhancement of the hydrophobicity of the films. The inclusion of 4F-PH$^+$ in the crystal lattice enhanced the grain size and reduced the density of the grain boundary (GB). The lower number of GB and the presence of hydrophobic fluoride ions benzene ring in 4F-PHCl combinedly showed the resistivity against water.[1] This improved hydrophobicity is the foundation for preventing perovskite degradation under ambient environments, which enables a stable Sn-based PSC.

Figure 3.3-11. Water contact angle measurement of the pristine and 10% 4F-PHCl modified perovskite films.

3.3.5   Photophysical Properties of Perovskite Films

The results of studies using steady-state photoluminescence (PL) and time-resolved photoluminescence (TRPL) spectroscopy are shown in **Figures 3.3-12a, b**. It has been found that there is a shift to the blue side of the spectrum at the peak of the PL spectra for 10% 4F-PHCl-containing perovskite films. This blue shifted because of the inclusion of 4F-PH$^+$ into the crystal lattice. The stronger PL intensity for 10% 4F-PHCl containing perovskite film indicates the 4F-PH$^+$ helps to the formation of higher quality film and effectively

suppresses the nonradiative charge carrier recombination. In addition, the pristine film in **Figure 3.3-12b** has a carrier lifetime of 4.36 ns, but the film with 10% 4F-PHCl has a carrier lifetime of 8.9 ns. The prolonged carrier lifetime is due to the higher crystallinity and suppression of defects in the perovskite films.

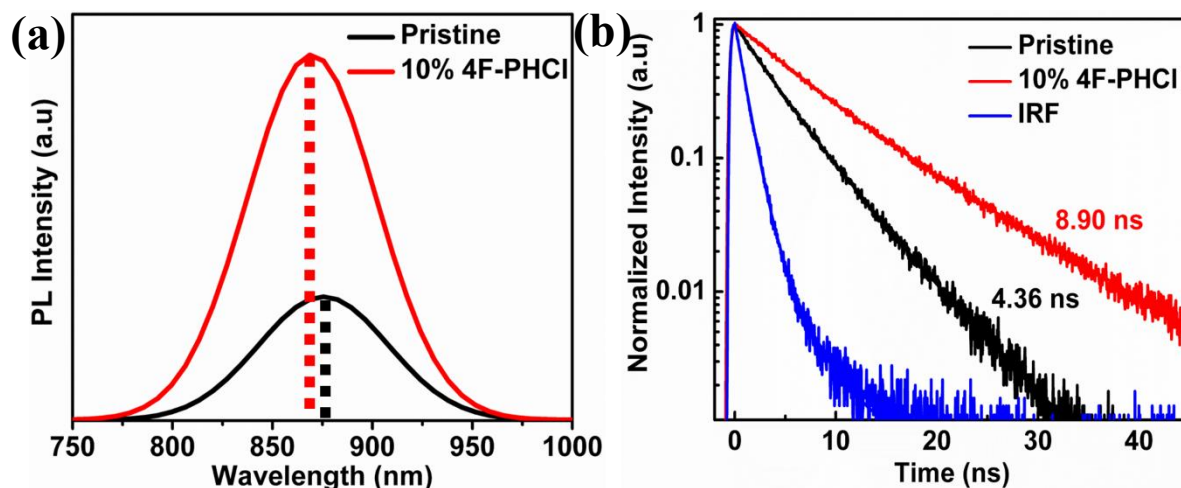**Figure 3.3-12.** (a) Steady-state PL spectra and (b) Normalized time-resolved photoluminescence (TRPL) spectra of pristine and 10% 4F-PHCl modified films fabricated on glass substrates.

3.3.6   Photovoltaic Performances and Reproducibility

To evaluate the effect of 4F-PHCl additive on photovoltaic performance, we fabricated inverted structure PSCs with an ITO/PEDOT: PSS/perovskite/C_{60}/bathocuproine (BCP)/Ag, as shown in **Figure 3.3-13a**. The comparable cross-sectional SEM images of pristine and 10% 4F-PHCl modified PSCs are shown in **Figure 3.3-7**. The modified PSCs showed the more uniform grain of the perovskite layer, which was well sandwiched between the C_{60} electron transport layer (ETL) and the PEDOT: PSS hole transport layer (HTL). **Figure 3.3-13b** shows the current density-voltage (*J-V*) of pristine and 10% 4F-PHCl modified PSC. The PSCs of pristine have a PCE of 6.32%, with a J_{SC} of 17.90 mAcm^{-2}, V_{OC} of 0.51 V, and fill factor (FF) of 69.2%. With the inclusion of 10% 4F-PHCl, the photovoltaic performance of the PSCs has significantly improved PCE of 10.86%, with a J_{SC} of 20.95 mAcm^{-2}, V_{OC} of 0.73 V, and fill factor (FF) of 71.0 %. The PCE improvement is due to the enhancement of J_{SC} and FF. The higher J_{SC}, V_{OC}, and FF due to the enlarger crystal grain ensures more charge transportation and lower trapped of the carrier. The incident photon-to-current conversion efficiency (IPCE) spectra of pristine and 10% 4F-PHCl-containing PSCs are shown in **Figure 3.3-13c**. The IPCE enhancement ensures the reliability of improved photocurrent. The modified PSCs showed an increased

Results and Discussion

IPCE value in the wavelength range from 300-830 nm, which correlates to the higher J_{SC} value for 4F-PHCl-containing PSCs. The integrated J_{SC} from the IPCE measurements well matches the calculated J_{SC} value from the *J-V* curves. **Figure 3.3-13d** shows the distribution of photovoltaic PCEs of pristine and 10% 4F-PHCl modified PSCs. The modified PSCs have shown the more uniform distribution of PCE indicates good reproducibility.

Figure 3.3-13. (a) Complete PSC structure. (b) *J-V* curves and (c) IPCE of pristine and 10% 4F-PHCl modified PSCs. (d) Statistical distribution of PCE for pristine and 10% 4F-PHCl modified PSC.

3.3.7 Perovskite Solar Cells Properties

To evaluate the passivation effect in 10% 4F-PHCl modified perovskite films, the space-charge-limited current (SCLC) analysis has been used to quantify the trap-state density and electron mobility for electron only devices based on pristine and 10% 4F-PHCl modified. The device structure ITO/SnO$_2$/FASnI$_3$/C$_{60}$/Ag as in

Results and Discussion

Figure 3.3-14a, and defect density was calculated by using trap-filled limit (TFL) voltage (V_{TFL}). The defect density (n_t) can be calculated by using the following equation.

$$n_t = 2\ \varepsilon_r \varepsilon_o V_{TFL}/qL^2$$

where q is the elementary charge of the electron, ε_r is the relative dielectric constant (5.7), ε_o is an absolute dielectric constant of vacuum (8.85 $\times$ 10^{-14} Fcm^{-1}), and L is the thickness of perovskite film (180 nm).[96] The trap density of the pristine and 10% 4F-PHCl modified device are 4.87×10^{15}, and 2.92×10^{15} cm^{-3} with V_{TFL} values are 0.25 V and 0.15 V, respectively. In addition, we have calculated the electron mobility of the respected devices by using the following equation.

$$J = 9\varepsilon_r \varepsilon_o \mu_e V^2/8L^3$$
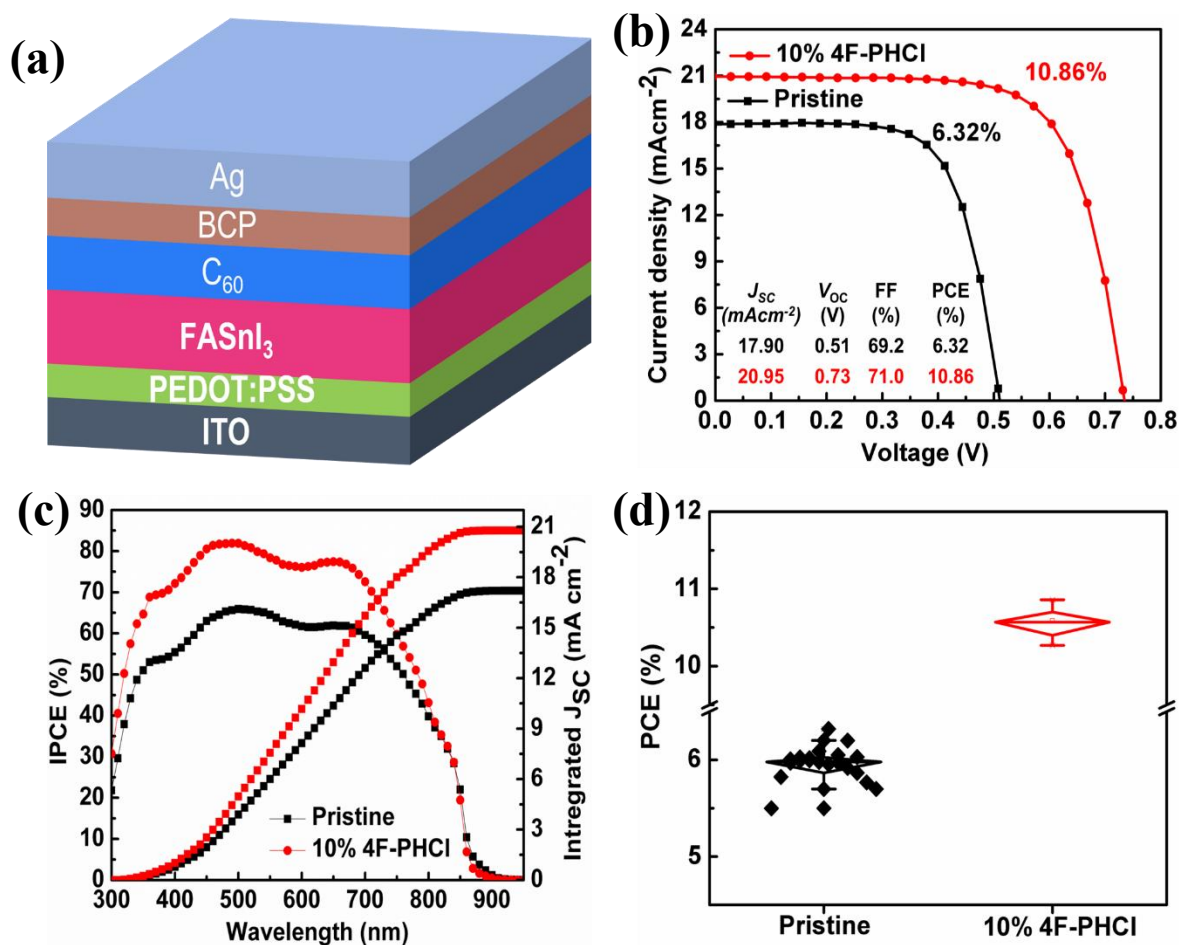
where J and V are the current and voltage of the electron-only device, respectively. The calculated electron mobility of the 10% 4F-PHCl modified device is 3.36×10^{-3} cm^2 V^{-1} s^{-1}, which is higher than a pristine device (1.57×10^{-4} cm^2 V^{-1} s^{-1}). The reduction of trap density and enhancement of electron mobility of modified device due to the high quality of fabricated perovskite film.

To examine the charge transport characteristics of pristine and 10% 4F-PHCl modified PSCs, we conducted electrochemical impedance spectroscopy (EIS) measurements in dark conditions, as shown in **Figure 3.3-14b**. The charge recombination resistance values are connected to the single semicircle that can be seen in the Nyquist plots of both the pristine and modified PSCs. The modified PSC has a bigger semicircle, which indicates that it has a larger recombination resistance (R_{rec}) than the pristine PSC. The enhancement of crystal quality and suppression of Sn^{2+} oxidation and I$^-$ losses, both of which work together to effectively limit the recombination of charge carriers. To gain more information on charge carrier transportation, we examined the transient photovoltage (TPV) of the PSCs, as shown in **Figure 3.3-14c**. TPV measurement is conducted under an open circuit condition and reflects the information about photo carrier recombination. The pristine PSC showed a lower photovoltage decay constant of 3.22 μs than the modified PSC (4.32 μs). This finding indicated that the carrier recombination was delayed for modified PSC than pristine PSC. To confirm the reasons for reduced charge recombination for PSCs, we carried out the dark *J-V* measurement for both PSCs, as shown in **Figure 3.3-14d**. The modified PSC displays are subjected to lower leakage current than pristine

PSC. The lower leakage current of modified PSC indicated a significantly lower background carrier density and more good diode behaviour than pristine PSC.
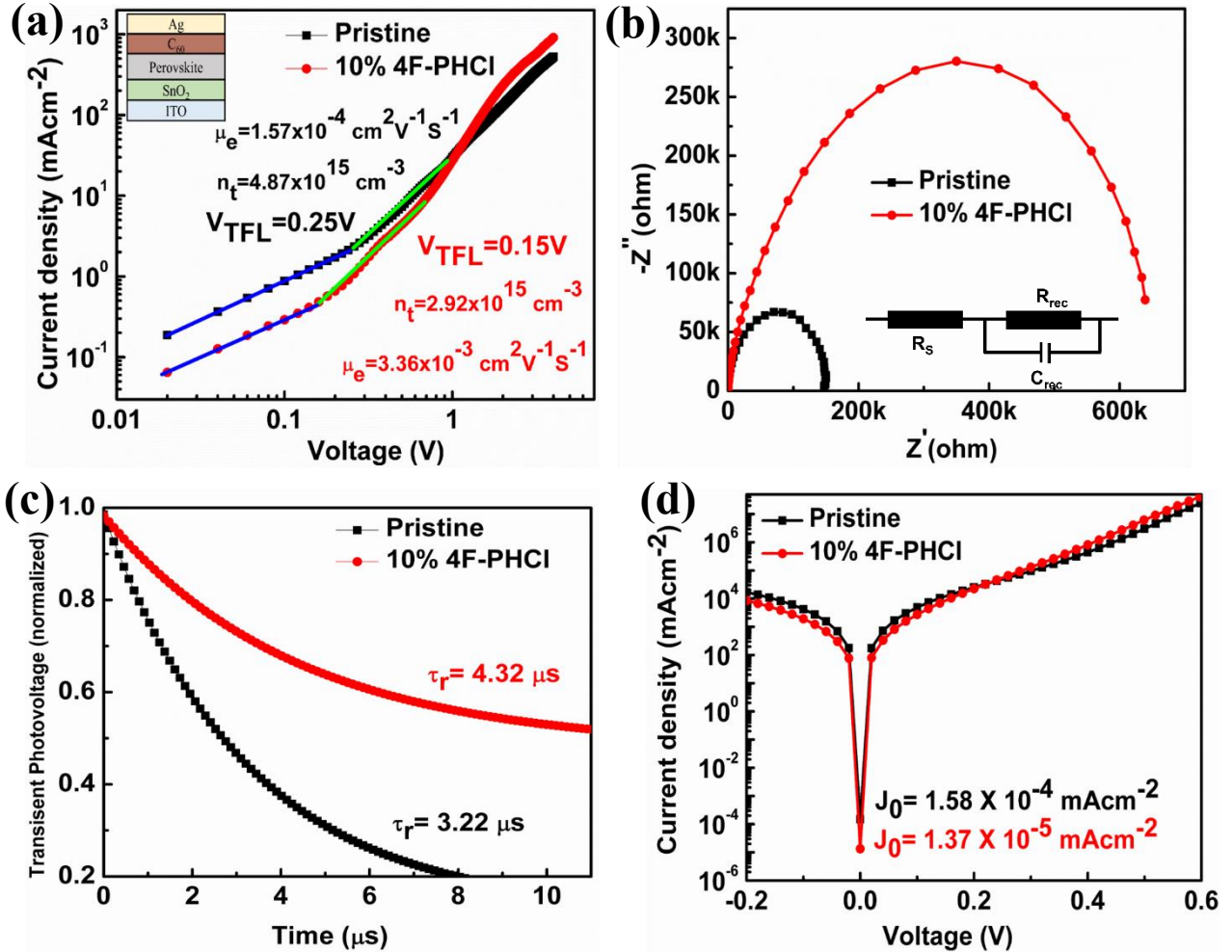
Figure 3.3-14. (a) Dark *J-V* curves of the electron-only devices fabricated with pristine and 10% 4F-PHCl modified absorber layer. (b) Nyquist plot measurement under dark conditions, (c) Transient photovoltage decay, and (d) dark *J-V* curves of pristine and 10% 4F-PHCl modified PSCs.

3.3.8 Stability of PSCs

To evaluate the stability of the fabricated PSC, we stored it inside an N_2-filled glovebox and monitored the stability over a period of time. The pristine PSC decreased its original PCE by about 40% after 25 days, as shown in **Figure 3.3-15**. In contrast, the modified PSC retained about 92% of its original PCE after 80 days. Therefore, the high quality of fabricated films after modification by 4F-PHCl could effectively suppress the Sn^{2+} oxidation and I^- losses and manage the PSC stability in N_2 environments.
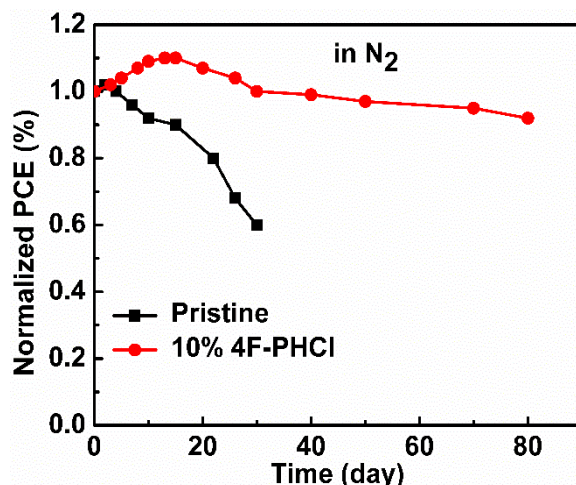
Figure 3.3-15. Shelf-life stability of pristine and 10% 4F-PHCl modified PSCs in an N_2 glovebox.

In summary, we introduced the 4F-PHCl additive in the $FASnI_3$ precursor solution and stabilized the solution properties. It is demonstrated that the hydrazine functional group maintains the $FASnI_3$ precursor solution quality by controlling SnI_2 dissociation in DMSO solvent. This additive could I_2 defects back to I^-, which inhibits the formation of I_2 and generation of free Sn^{2+} ions in precursor solution and effectively suppresses the Sn^{2+} oxidation. In addition, large organic cation $4F-PH^+$ ions are successfully incorporated into the crystal lattice without any dimensionality reduction of 3D perovskite crystals and maintain moisture stability due to the presence of a hydrophobic fluorinated benzene ring. As a result, 10 % 4F-PHCl modified PSCs showed PCE of 10.86%, and the unencapsulated device maintained over 92% of initial PCE in N_2 glovebox for 80 days. This work light on the initial source of Sn^{2+} oxidation in final films and provides an in-depth insight into effective strategies to hinder the Sn^{2+} oxidation in precursor solution and fabricated high-quality films.

CHAPTER 4:
CONCLUSION

Conclusion

Globalization and mankind fully depend on the availability of energy. To meet the energy demand while considering the environmental impact, the future energy hub may possibly use renewable energy. Solar energy has to play the leading role in renewable energy due to the sun being the never-ending source and the most dependable. Photovoltaic cells convert sunlight into electricity, and modern technological advantages help to improve performance over time. The use of perovskite materials as an absorber in perovskite solar cells (PSCs) has been highlighted as a potentially game-changing innovation in photovoltaic technology. The power conversion efficiency (PCE) of PSCs is quickly catching up to that of established solar technology as a consequence of worldwide research efforts in a short period of time. The most interesting aspect of PSCs is their easy and low-cost fabrication system. Due to the promising optoelectronic properties and easy fabrication process, researchers of the photovoltaic community have been inspired to solve the existing problems. To consider the commercialization of PSCs, their performance, as well as stability and reproducibility, are important. The absorber layer is the key concerning issues of PSCs. In this thesis, our aim is to develop lead-free perovskite materials while considering the reproducibility, stability, and performance of PSCs.

In this thesis, I have successfully fabricated the reproducible and stable $CsBi_3I_{10}$ PSCs with optimized fabrication conditions of thin films and introduced a bathocuproine (BCP) interfacial layer (BIL) at the perovskite/ETL interface. We obtained suitable fabrication conditions. Furthermore, for the first time in Bi-PSCs, we introduced a BIL in the perovskite/ETL interface of inverted planar device structure; ITO/ PEDOT: PSS/ $CsBi_3I_{10}$/BCP/C_{60}/BCP/Ag. The inclusion of BIL at the perovskite/ETL interface reduced the possible hole leakage from the HTL to the ETL through $CsBi_3I_{10}$. The BIL reduced the interfacial defects at perovskite/ETL interfaces and improved the reproducibility of the respective PSCs. The PSC with a 6-nm-sized BIL has a maximum PCE of 0.80% and excellent reproducibility. Furthermore, the PSC exhibits negligible hysteresis effects and retains ~90% PCE of its initial efficiency after 528 h. Although the PCE of $CsBi_3I_{10}$ PSC is still lacking, this study showed the pathway to improve the reproducibility and stability of Bi-PSCs, which is a basic requirement for the systematic development of PCE.

In an attempt to improve the PSC's performance of Sn-PSCs, we introduced the bulky guanidine-based

Conclusion

additive 1,3-diaminoguanidine monohydrochloride (DAGCl) into an Sn perovskite to improve the perovskite crystallization and passivate the electronic defects. The amino groups of the bifunctional DAGCl formed hydrogen bonding with iodide in the $FASnI_3$ framework and suppressed the losses of I^-. The Cl^- formed covalent bonds with undercoordinated Sn^{2+} ions and improved the crystallinity with a stabilized $FASnI_3$ perovskite structure and retarded the Sn^{2+} oxidation. This dual aspect of the DAGCl additive simultaneously affects the fabrication process, enhances electron mobility, and reduces trap density. The modified PSC (3% mol DAGCl) showed a PCE of 8.92% with a significantly improved V_{OC} of up to 0.61 V. The enhancement of V_{OC} is about 110 mV compared to the pristine PSC (0.50 V) due to the improved perovskite film quality and the well-matched energy band diagram with the adjacent transport layer. Moreover, the modified PSC retained 95% of its initial PCE after 1100 h and showed stability during continuous light soaking.

In this thesis, we attempted to determine the cause of Sn^{2+} oxidation in Sn-perovskite and introduced the possible solutions. We introduced the 4F-PHCl additive in the $FASnI_3$ precursor solution and stabilized the solution properties. It is demonstrated that the hydrazine functional group maintains the $FASnI_3$ precursor solution quality by controlling SnI_2 dissociation in DMSO solvent. This additive could I_2 defects back to I^-, which inhibits the formation of I_2 and generation of free Sn^{2+} ions in precursor solution and effectively suppresses the Sn^{2+} oxidation. In addition, large organic cation 4F-PH$^+$ ions are successfully incorporated into the crystal lattice without any dimensionality reduction of 3D perovskite crystals and maintain moisture stability due to the presence of a hydrophobic fluorinated benzene ring. As a result, 10 % 4F-PHCl modified PSCs showed PCE of 10.86%, and the unencapsulated device maintained over 92% of initial PCE in N_2 glovebox for 80 days. This work light on the initial source of Sn^{2+} oxidation in final films and provides an in-depth insight into effective strategies to hinder the Sn^{2+} oxidation in precursor solution and fabricated high-quality films.

In conclusion, this thesis work instructs the reader on how to improve the reproducibility and stability of Bi-PSCs. In the case of Sn-PSCs, this thesis introduced an effective way to reduce the Sn^{2+} oxidation and I^- ion losses. This work finds out the origin of Sn^{2+} oxidation in the precursor solution of Sn-perovskite and introduces an effective way to solve this problem.
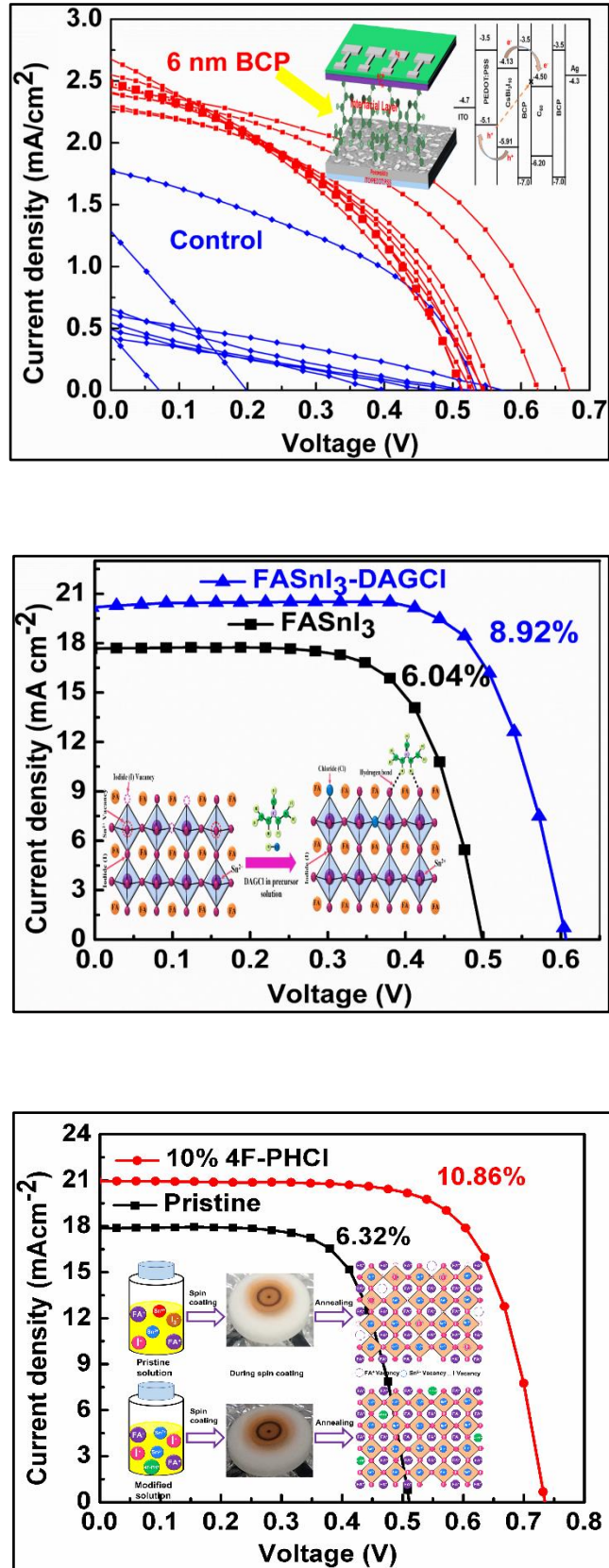
Conclusion

Figure 4.1. Summary of the research in this thesis.

CHAPTER 5: REFERENCES

References

References:

(1) Atehmengo, N.; Idika, I. K.; Shehu, A.; Ibrahim, R. Climate Change/Global Warming and its Impacts on Parasitology/Entomology. *Parasitology* **2014** ,5, 1-11.

(2) Twidell, J. Renewable Energy Resources. *Routledge* **2021**.

(3) Hamdeh, U. H. Solution-Processed Bismuth Halide Thin Film Semiconductor for Photovoltaic Application. Iowa State University **2019**.

(4) U.S. Energy Information Administration, Independent Statistics and Analysis. (March 3, 2022), www.eia.gov/aeo.

(5) Lu, Y.; Khan, Z. A.; Alvarez-Alvarado, M. S.; Zhang, Y.; Huang, Z.; Imran, M. J. S. A Critical Review of Sustainable Energy Policies for the Promotion of Renewable Energy Sources. *Sustainability*, **2020,** 12, 5078.

(6) Palz, W.; Power for the World: The Emergence of Electricity from the Sun. Belgium: Pan Stanford Publishing. **2010**.

(7) Chapin, D.; Fuller, C.; Pearson, G. A New Silicon P-N Junction Photocell for Converting Solar Radiation into Electrical Power. *J. Appl. Phys.* **1954,** 25, 676-677.

(8) Shah, A.; Torres, P.; Tscharner, R.; Wyrsch, N.; Keppner, H. Photovoltaic Technology: The Case for Thin-Film Solar Cells. *Science.* **1999**, 285, 692-698.

(9) Goswami, R. Three Generations of Solar Cells. *AMR* **2021**, 1165, 113–30.

(10) Wenk, H. R.; Bulakh, A. Minerals: Their Constitution and Origin. *New York, NY: Cambridge University Press*. **2004**.

(11) Cho, Y. J.; Jeong, M. J.; Park, J. H.; Hu, W.; Lim, J.; Chang, H. S. Charge Transporting Materials Grown by Atomic Layer Deposition in Perovskite Solar Cells. *Energies* **2021,** 14, 1156.

(12) Jacobsson, T. J.; Pazoki, M.; Hagfeldt, A.; Edvinsson, T. Goldschmidt's Rules and Strontium Replacement in Lead Halogen Perovskite Solar Cells: Theory and Preliminary Experiments on $CH_3NH_3SrI_3$. *J. Phys. Chem. C* **2015**, *119*, 25673-25683.

(13) Fan, Z.; Sun, K.; Wang, J. Perovskites for Photovoltaics: A Combined Review of Organic-Inorganic Halide Perovskites and Ferroelectric Oxide Perovskites. *J. Mater. Chem. A*, **2015,** *3,* 18809-18828.

(14) De Wolf, S.; Holovsky, J.; Moon, S.-J.; Löper, P.; Niesen, B.; Ledinsky, M.; Haug, F.-J.; Yum, J.-H.; Ballif,

References

C. Organometallic Halide Perovskites: Sharp Optical Absorption Edge and its Relation to Photovoltaic Performance. *J. Phys. Chem. Lett.*, **2014,** *5*, 1035-1039.

(15) De Wolf, S.; Holovsky, J.; Moon, S.-J.; Löper, P.; Niesen, B.; Ledinsky, M.; Haug, F.-J.; Yum, J.-H.; Ballif, C. Organometallic Halide Perovskites: Sharp Optical Absorption Edge and its Relation to Photovoltaic Performance. *J. Phys. Chem. Lett.* **2014,** *5*, 1035-1039.

(16) Jensen, N.; Hausner, R.; Bergmann, R.; Werner, J.; Rau, U. Optimization and Characterization of Amorphous/Crystalline Silicon Heterojunction Solar Cells. *Prog Photovolt* **2002,** 10, 1-13.

(17) Baranowski, M.; Plochocka, P. Excitons in Metal-Halide Perovskites. *Adv. Energy Mater.* **2020**, 10, 1903659.

(18) Xing, G.; Mathews, N.; Sun, S.; Lim, S. S.; Lam, Y. M.; Grätzel, M.; Mhaisalkar, S.; Sum, T. C. Long-Range Balanced Electron-and Hole-Transport Lengths in Organic-Inorganic $CH_3NH_3PbI_3$. *Science* **2013,** 342, 344-347.

(19) Kojima, A.; Teshima, K.; Shirai, Y.; Miyasaka, T. Organometal Halide Perovskites as Visible-Light Sensitizers for Photovoltaic Cells. *J. Am. Chem. Soc.* **2009,** 131, 6050-6051.

(20) Meng, L.; You, J.; Guo, T.-F.; Yang, Y. Recent Advances in the Inverted Planar Structure of Perovskite Solar Cells. *Acc. Chem. Res.* **2016**, 49, 1, 155–165.

(21) Basumatary, P.; Kumari, J.; Agarwal, P. In Enhancing the Performance and Stability of $MAPbI_3$ Perovskite Solar Cells by Inserting the ITO Layer Before the Ag Electrode. *AIP Conference Proceedings* **2021**, 020022.

(22) Wang, J.; Zhang, J.; Zhou, Y.; Liu, H.; Xue, Q.; Li, X.; Chueh, C.-C.; Yip, H.-L.; Zhu, Z.; Jen, A. K. Y. Highly Efficient All-Inorganic Perovskite Solar Cells with Suppressed Non-Radiative Recombination by A Lewis Base. *Nat. Commun*. **2020,** 11, 1-9.

(23) Gidlow, DA. Lead Toxicity. *Occupational Medicine.* **2004,** 54, 76-81.

(24) Pathak, S. K.; Abate, A.; Ruckdeschel, P.; Roose, B.; Gozdel, K. C.; Vaynzof, Y. Performance and Stability Enhancement of Dye-Sensitized and Perovskite Solar Cells by Al Doping of TiO_2. *Adv Funct Mater.* **2014,** 24, 6046-6055.

(25) Fewtrell, L.; Kaufmann, R.; Prüss-Üstün, A.; *Lead:* Assessing the Environmental Burden of Disease at National and Local Levels (World Health Organization, **2003**).

References

(26) Zayed, J.; Philippe, S. Acute Oral and Inhalation Toxicities in Rats with Cadmium Telluride. *Int. J. Toxicol.,* **2009,** *28*, 259-65.

(27) Abate, A. Perovskite Solar Cells go Lead free. *Joule* **2017**, 1, 659-664.

(28) Jin, Z.; Zhang, Z.; Xiu, J.; Song, H.; Gatti, T.; He, Z. A Critical Review on Bismuth and Antimony Halide Based Perovskites and their Derivatives for Photovoltaic Applications: Recent Advances and Challenges. *J. Mater. Chem. A* **2020,** *8*, 16166-16188.

(29) Eckhardt, K.; Bon, V.; Getzschmann, J.; Grothe, J.; Wisser, F. M.; Kaskel, S. Crystallographic Insights into $(CH_3NH_3)_3(Bi_2I_9)$: A New Lead-Free Hybrid Organic-Inorganic Material as a Potential Absorber for Photovoltaics. *Chem Commun.* **2016,** 52, 3058-3060.

(30) Murugan, V.; Ohta, T.; Iikubo, S.; Kapil, G.; Ripolles, T. S.; Ogomi, Y.; Ma, T.; Pandy, S. S.; Shen, Q.; Toyoda, T.; Yoshino, T.; Minemoto, T.; Hayase, S. Facile Synthesis and Characterization of Sulfur Doped Low Bandgap Bismuth Based Perovskites by Soluble Precursor Route. *Chem Mater.* **2016,** 28, 6436-6440.

(31) Sebastia-Luna, P.; Gelvez-Rueda, M. C.; Dreessen, C.; Sessolo, M.; Grozema, F. C.; Palazon, F.; Bolink, H. J. Potential and Limitations of $CsBi_3I_{10}$ as a Photovoltaic Material. *J. Mater. Chem. A* **2020,** 8, 15670.

(32) Rühle, S. Tabulated Values of the Shockley-Queisser Limit for Single Junction Solar Cells. *Solar Energy* **2016,** *130*, 139-147.

(33) Mallick, A.; Visoly-Fisher, I. Pb in Halide Perovskites for Photovoltaics: Reasons for Optimism. *Mater. Adv.,* **2021**, 2, 6125.

(34) National Renewable Energy Laboratory (NREL). https://www.nrel.gov/pv/assets/pdfs/best-research-cell-efficiencies-rev220630.pdf (accessed 30 June 2022).

(35) Eperon, G. E.; Stranks, S. D; Menelaou, C.; Johnston, M. B.; Herz, L. M.; Snith, H, J. Formamidinium Lead Trihalide: A Broadly Tunable Perovskite for Efficient Planar Heterojunction Solar Cells. *Energy Env. Sci* **2014**, **7**, 982–988.

(36) Stranks, S. D. *et al.* Electron-Hole Diffusion Lengths Exceeding 1 Micrometer in an Organometal Trihalide Perovskite Absorber. *Science* **2013**, 342, 341–344.

(37) Lee, M. M.; Teuscher, J.; Miyasaka, T.; Murakami, T. N.; Snaith, H. J. Efficient Hybrid Solar Cells Based on Meso-Superstructured Organometal Halide Perovskites. *Science* **2012**, 338, 643– 647.

References

(38) Yin, W.-J.; Shi, T.; Yan, Y. Unique Properties of Halide Perovskites as Possible Origins of the Superior Solar Cell Performance. *Adv. Mater.* **2014**, 26, 4653–4658.

(39) You, J. *et al.* Low-Temperature Solution-Processed Perovskite Solar Cells with High Efficiency and Flexibility. *ACS Nano* **2014**, 8, 1674–1680.

(40) Yang, W. S.; Noh, J. H.; Jeon, N. J.; Kim, Y. C.; Ryu, S.; Seo, J.; Seok, S. High-Performance Photovoltaic Perovskite Layers Fabricated through Intramolecular Exchange. *Science* **2015**, 348, 1234.

(41) Saliba, M. *et al.* A Molecularly Engineered Hole-Transporting Material for Efficient Perovskite Solar Cells. *Nat. Energy* 2016, 1, 15017.

(42) Filip, M. R.; Eperon, G. E.; Snaith, H. J.; Giustino, F. Steric Engineering of Metal-Halide Perovskites with Tunable Optical Band Gaps. *Nat Commun* **2014**, 5, 5757.

(43) Kim, Y. -H.; cho, H.; Heo, J. H.; Kim, T. -S.; Myoung, N.; Lee, C. -L.; Im, S. H.; Lee, T. -W. Multicolored Organic/Inorganic Hybrid Perovskite Light-Emitting Diodes. *Adv. Mater.* **2015**, 27, 1248–1254.

(44) Zhu, H.; Fu, Y.; Meng, F.; Wu, X.; Gong, Z.; Ding, Q.; Gustafsson, M. V.; Trinh, M. T.; Zhu, X-Y. Lead Halide Perovskite Nanowire Lasers with Low Lasing Thresholds and High Quality Factors. *Nature Mater* **2015**, 14, 636–642.

(45) Dou, L.; Yang, Y.; You, J.; Hong, Z.; Chang, W-H.; Li, G.; Yang, Y. Solution-Processed Hybrid Perovskite Photodetectors with High Detectivity. *Nat Commun* **2014**, 5, 5404.

(46) Babayigit, A.; Ethirajan, A.; Muller, M.; Conings, B. Toxicity of Organometal Halide Perovskite Solar Cells. *Nat. Mater.* **2016**, 15, 247.

(47) Conings, B.; Drijkoningen, J.; Gauquelin, N.; Babayigit, A.; D'Haen, J.; D'Olieslaeger, L.; Ethirajan, A.; Verbeeck, J.; Manca, J.; Mosconi, E.; Angelis, F. D.; Boyen, H-G. (2015). Intrinsic Thermal Instability of Methylammonium Lead Trihalide Perovskite. *Adv. Energy Mater*. **2015**, 5, 1500477.

(48) Divitini, G.; Cacovich, S.; Matteocci, F.; Cina, L.; Carlo, A. D.; Ducati, C. In situ Observation of Heat-Induced Degradation of Perovskite Solar Cells. *Nat Energy* **2016**, 1, 15012.

(49) Manser, J. S.; Saidaminov, M. I.; Christians, J. A.; Bakr, O. M.; Kamat, P. V.; Making and Breaking of Lead Halide Perovskites. *Acc. Chem. Res.* 2016, 49, 330–338.

(50) Nelson, W. O.; Campbell, P. G. C. The Effects of Acidification on the Geochemistry of Al, Cd, Pb and Hg

References

in Freshwater Environments: A Literature Review. *Environ. Acidif. Met.* **1991**, 71, 91–130.

(51) Lyu, M.; Yun, J.-H.; Cai, M.; Jiao, Y.; Bernhardt, P. V.; Zhang, M.; Wang, Q.; Du, A.; Wang, H.; Liu, G.; Wang, L. Organic–inorganic Bismuth (III)-Based Material: A Lead-Free, Air-Stable and Solution-Processable Light-Absorber Beyond Organolead Perovskites. *Nano Res.* **2016,** *9*, 692-702.

(52) Li, F.; Fan, H.; Wang, P.; Li, X.; Song, Y.; Jiang, K.-J. Improved Film Morphology of $(CH_3NH_3)_3Bi_2I_9$ via Cation Displacement Approach for Lead-Free Perovskite Solar Cells. *J mater Sci.* **2019,** *54*, 10371-10378.

(53) Park, B. W.; Philippe, B.; Zhang, X.; Rensmo, H.; Boschloo, G.; Johansson, E. M. J. Bismuth Based Hybrid Perovskites $A_3Bi_2I_9$ (A: Methylammonium or Cesium) for Solar Cell Application. *Adv. Mater.* **2015,** *27*, 6806-6813.

(54) Jain, S. M.; Phuyal, D.; Davies, M. L.; Li, M.; Philippe, B.; De Castro, C.; Qiu, Z.; Kim, J.; Watson, T.; Tsoi, Olof, K.; Rensmo, H.; Boschloo, G.; Edvinsson. T.; Durrant, J. R. An Effective Approach of Vapour Assisted Morphological Tailoring for Reducing Metal Defect Sites in Lead-Free, $(CH_3NH_3)_3Bi_2I_9$ Bismuth-Based Perovskite Solar Cells for Improved Performance and Long-Term Stability. *Nano Energy* **2018,** *49*, 614-624.

(55) Johansson, M. B.; Zhu, H.; Johansson, E. M. J. Extended Photo-Conversion Spectrum in Low-Toxic Bismuth Halide Perovskite Solar Cells. *J. Phys. Chem. Lett.* **2016,** *7*, 3467-3471.

(56) Zhu, H.; Johansson, M. B.; Johansson, E. M. J. The Effect of Dopant-Free Hole-Transport Polymers on Charge Generation and Recombination in Cesium–Bismuth–Iodide Solar Cells. *ChemSusChem* **2018,** *11*, 1114-1120.

(57) Shin, J.; Kim, M.; Jung, S.; Kim, C. S.; Park, J.; Song, A.; Chung, K.-B.; Jin, S.-H.; Lee, J. H.; Song, M. Enhanced Efficiency in Lead-Free Bismuth Iodide with Post Treatment Based on a Hole-Conductor-Free Perovskite Solar Cell. *Nano Research* **2018,** *11*, 6283-6293.

(58) Mariyappan, P.; Chowdhury, T. H.; Subashchandran, S.; Bedja, I.; Ghaithan, H. M.; Islam, A. Fabrication of Lead-Free $CsBi_3I_{10}$ Based Compact Perovskite Thin Films by Employing Solvent Engineering and Anti-Solvent Treatment Techniques: an Efficient Photo-Conversion Efficiency up to 740 nm. *Sustainable Energy Fuels* **2020,** *4*, 5042-5049.

(59) Mariyappan, P.; Chowdhury, T. H.; Subashchandran, S.; Bedja, I.; Ghaithan, H. M.; Islam, A. Influence

of Inorganic NiO_x Hole Transport Layer on the Growth of $CsBi_3I_{10}$ Perovskite Films for Photovoltaic Applications. *Adv. Mater. Interfaces* **2021**, 2002083.

(60) Shao, S.; Loi, M. A. The Role of the Interfaces in Perovskite Solar Cells. *Adv. Mater. Interfaces* **2020,** *7*, 1901469.

(61) Thanh, N. T.; Maclean, N.; Mahiddine, S. Mechanisms of Nucleation and Growth of Nanoparticles in Solution. *Chem. Rev*. **2014,** *114*, 7610-7630.

(62) Ahn, N.; Kang, S. M.; Lee, J.-W.; Choi, M.; Park, N.-G. Thermodynamic Regulation of $CH_3NH_3PbI_3$ Crystal Growth and its Effect on Photovoltaic Performance of Perovskite Solar Cells. *J. Mater. Chem. A* **2015,** *3*, 19901-19906.

(63). Wan, Z.; Lai, H.; Ren, S.; He, R.; Jiang, Y.; Luo, J.; Chen, Q.; Hao, X.; Wang, Y.; Zhang, J.; Wu, L.; Zhao, D. *J*. Interfacial Engineering in Lead-Free Tin-Based Perovskite Solar Cells. *Energy Chem.* **2021**, 57, 147.

(64). Nasti G.; Abate, A. Tin Halide Perovskite ($ASnX_3$) Solar Cells: A Comprehensive Guide toward the Highest Power Conversion Efficiency**.** Adv. *Energy Mater.* **2020**, 10, 1902467.

(65). Yu, B.-B.; Chen, Z.; Zhu, Y.; Wang, Y.; Han, B.; Chen, G.; Zhang, X.; Du, Z.; He, Z. Heterogeneous 2D/3D Tin-Halides Perovskite Solar Cells with Certified Conversion Efficiency Breaking 14%. *Adv. Mater*. **2021**, 33, 2102055.

(66) Jiang, X.; Wang, F.; Wei, Q.; Li, H.; Shang, Y.; Zhou, W.; Wang, C.; Cheng, P.; Chen, Q.; Chen, L.; Ning, Z. Ultra-High Open-Circuit Voltage of Tin Perovskite Solar Cells via an Electron Transporting Layer Design. *Nat Commun*. **2020**, 11, 1245.

(67) Liu, M.; Chen, Z.; Yang, Y.; Yip, H.L.; Cao, Y. Reduced Open-Circuit Voltage Loss for Highly Efficient Low-Bandgap Perovskite Solar Cells via Suppression of Silver Diffusion. *J. Mater. Chem. A* **2019**, 7, 17324.

(68) Li, S.; Yang, F.; Chen, M.; Yang, J.; Jiang, L.; Sun, Y.; Graced, A.N.; Jain, S.M.; Liu, H. Additive Engineering for Improving the Stability of Tin-Based Perovskite ($FASnI_3$) Solar Cells. *Solar Energy* **2022**, 243, 134-141.

(69) Zhang, F.; Zhu, K. Additive Engineering for Efficient and Stable Perovskite Solar Cells. *Adv. Energy Mater*. **2020**, 10, 1902579.

(70) Li, Y.; Li, Z.; Liu, F.; Wei, J. Defects and Passivation in Perovskite Solar Cells. *Surface Innovations* **2022**,

References

10, 3-20.

(71) Abdel-Shakour, M.; Chowdhury, T. H.; Matsuishi, K.; Karim, M.A.; He, Y.; Moritomo, Y.; Islam, A. Diaminomaleonitrile Lewis Base Additive for Push−Pull Electron Extraction for Efficient and Stable Tin-Based Perovskite Solar Cells. *ACS Appl. Energy Mater.* **2021**, 4, 12515-12524.

(72) Kayesh, M. E.; Chowdhury, T. H.; Matsuishi, K.; Kaneko, R.; Kazaoui, S.; Lee, J.-J.; Noda, T.; Islam, A. Enhanced Photovoltaic Performance of FASnI$_3$-Based Perovskite Solar Cells with Hydrazinium Chloride Coadditive. *ACS Energy Lett.* **2018**, 3, 1584-1589.

(73) Jokar, E.; Chien, C.-H.; Fathi, A.; Rameez, M.; Chang, Y.-H.; Diau, E. W.-G. Slow Surface Passivation and Crystal Relaxation with Additives to Improve Device Performance and Durability for Tin-Based Perovskite Solar Cells. *Energy Environ. Sci.* **2018**, 11, 2353-2362.

(74) Chowdhury, T. H.; Kaneko, R.; Kaneko, Tomoaki.; Sodeyama, K.; Lee, J.J.; Islam, A. Electronic Defect Passivation of FASnI$_3$ Films by Simultaneous Hydrogen-Bonding and Chlorine Co-Ordination for Highly Efficient and Stable Perovskite Solar Cells. *Chem. Engg. Journal* **2021**, 431, 133745.

(75) Li, G.; Su, Z.; Li, M.; Yang, F.; Aldamasy, M. H.; Pascual, J.; Yang, F.; Liu, H.; Zuo, W.; Girolamo, D. D.; Iqbal, Z.; Nasti, G.; Dallmann, A.; Gao, X.; Wang, Z.; Saliba, M.; Abate, A. Ionic Liquid Stabilizing High-Efficiency Tin Halide Perovskite Solar Cells. *Adv. Energy Mater.* **2021**, 11, 2101539.

(76) Liu, G.; Zhong, Y.; Feng, W.; Yang, M.; Yang, G.; Zhong, J.-X.; Tian, T.; Luo, J. -B.; Tao, J.; Yang, S.; Wang, X.-D.; Tan, L.; Chen, Y.; Wu, W.-Q. Multidentate Chelation Heals Structural Imperfections for Minimized Recombination Loss in Lead-Free Perovskite Solar Cells. *Angew. Chem. Int. Ed.* **2022,** 61, e202209464.

(77) Cao, D. H.; Stoumpos, C. C.; Yokoyama, T.; Logsdon, J. L.; Song, T.-B.; Farha, O. K.; Wasielewski, M. R.; Hupp, J. T.; Kanatzidis, M. G. Thin Films and Solar Cells Based on Semiconducting Two-Dimensional Ruddlesden–Popper (CH$_3$(CH$_2$)$_3$NH$_3$)$_2$(CH$_3$NH$_3$)$_{n-1}$Sn$_n$I$_{3n+1}$ Perovskites. *ACS Energy Lett.* **2017**, 2, 982-990.

(78) Shao, S.; Liu, J.; Portale, G.; Fang, H.-H.; Blake, G. R.; ten Brink, G. H.; Koster, L. J. A.; Loi, M. A. Highly Reproducible Sn-Based Hybrid Perovskite Solar Cells with 9% Efficiency. *Adv. Energy Mater.* **2018**, 8, 1702019.

(79) Kayesh, M. E.; Matsuishi, K.; Kaneko, R.; Kazaoui, S.; Lee, J.-J.; Noda, T.; Islam, A. Coadditive

References

Engineering with 5-Ammonium Valeric Acid Iodide for Efficient and Stable Sn Perovskite Solar Cells. *ACS Energy Lett*. **2019**, 4, 278-284.

(80) Jokar, E.; Chien, C.-H.; Tsai, C.-M.; Fathi, A.; Diau, E. W.-G. Robust Tin-Based Perovskite Solar Cells with Hybrid Organic Cations to Attain Efficiency Approaching 10%. *Adv. Mater*. **2019**, 31, 1804835.

(81) Fu, Q.; Tang, X.; Li, D.; Huang, L.; Xiao, S.; Chen. Y.; Hu, T. An Efficient and Stable Tin-Based Perovskite Solar Cell Passivated by Aminoguanidine Hydrochloride. ***J. Mater. Chem. C* 2020**, **8**, 7786-7792.

(82) Yao, J.; Wang, H.; Wang, P.; Gurney, R.S.; Intaniwet, A.; Ruankham, P.; Choopun, S.; Liu, D, Wang, T. Trap Passivation and Efficiency Improvement of Perovskite Solar Cells by a Guanidinium Additive. *Mater. Chem. Front.* **2019**, 3, 1357.

(83) Pascual, J.; Nasti, G.; Aldamasy, M. H.; Smith, J. A.; Flatken, M.; Phung, N.; Di Girolamo, D.; Turren-Cruz, S.-H.; Li, M.; Dallmann, A.; Avolio, R.; Abate, A. Origin of Sn (II) Oxidation in Tin Halide Perovskites. *Mater. Adv.* **2020,** 1, 1066-1070.

(84) Li, X.; Dar, M. I.; Yi, C.; Luo, J.; Tschumi, M.; Zakeeruddin, S. M.; Nazeeruddin, M. K.; Han, H.; Grätzel, M. Improved Performance and Stability of Perovskite Solar Cells by Crystal Crosslinking with Alkylphosphonic Acid ω-Ammonium Chlorides. *Nat. Chem*. **2015**, 7, 703-711.

(85) Cao, X.; Li, J.; Dong, H.; Li, P.; Fan, Q.; Xu, R.; Li, H.; Zhou, G.; Wu, Z. Stability Improvement of Tin-Based Halide Perovskite by Precursor-Solution Regulation with Dual-Functional Reagents. *Adv. Funct. Mater*. **2021,** 31, 2104344.

(86) Chen, S.; Xiao, X.; Gu, H.; Huang, J. Iodine Reduction for Reproducible and High-Performance Perovskite Solar Cells and Modules. *Sci. Adv*. **2021,** 7, eabe8130.

(87) Jones, T. W.; Osherov, A.; Alsari, M.; Sponseller, M.; Duck, B. C.; Jung, Y.-K.; Settens, C.; Niroui, F.; Brenes, R.; Stan, Samuel D. S. Lattice Strain Causes Non-Radiative Losses in Halide Perovskites. *Energy Environ. Sci*. **2019,** *12*, 596-606.

(88) Kayesh, M. E.; Matsuishi, K.; Chowdhury, T. H.; Kaneko, R.; Lee, J.-J.; Noda, T.; Islam, A. Influence of Anti-Solvents on $CH_3NH_3PbI_3$ Films Surface Morphology for Fabricating Efficient and Stable Inverted Planar Perovskite Solar Cells. *Thin Solid Films* **2018,** *663*, 105-115.

References

(89) Meng, X.; Lin, J.; Liu, X.; He, X.; Wang, Y.; Noda, T.; Wu, T.; Yang, X.; Han, L. Highly Stable and Efficient FASnI$_3$-Based Perovskite Solar Cells by Introducing Hydrogen Bonding. *Adv. Mater*. **2019**, 31, 1903721.

(90) Quintero-Bermudez, R.; Gold-Parker, A.; Proppe, A. H.; Munir, R.; Yang, Z.; Kelley, S. O.; Amassian, A.; Toney, M. F.; Sargent, E. H. Compositional and Orientational Control in Metal Halide Perovskites of Reduced Dimensionality. *Nat. Mater*. **2018**, 17, 900-907.

(91) Li, H.; jiang, X.; Wei, Q.; Zang, Z.; Ma, M.; Wang, F.; Zhou, W.; Ning. Low-Dimensional Inorganic Tin Perovskite Solar Cells Prepared by Templated Growth. *Angew. Chem. Int. Ed.* **2021**, 60, 16330-16336.

(92) Karim, M.A.; Matsuishi, K.; Chowdhury, T. H.; Chowdhury, W. I.; Abdel-Shakour, M.; Islam, A. Bathocuproine Interfacial Layer Leads to Solid Improvement of Reproducibility and Stability of Pb-Free CsBi$_3$I$_{10}$ Based Perovskite Solar Cells. *J. Mater. Sci.: Mater. Electron*. **2022**, 33, 8114-8126.

(93) Su, Y.; Yang, J.; Liu, G.; Sheng, W.; Zhang, J.; Zhong, Y.; Tan, L.; Chen, Y. Acetic Acid-Assisted Synergistic Modulation of Crystallization Kinetics and Inhibition of Sn^{2+} Oxidation in Tin-Based Perovskite Solar Cells. *Adv. Funct. Mater.* **2022**, *32*, 2109631.

(94) Gu, W.; Xu, X.; Chen, J.; Ma, B.; Qin, M.; Zhu, W.; Qian, J.; Qin, Z.; Shen, W.; Lu, Y.; Zhang, W.; Chen, S.; Lu, X.; Huang, W. Oriented Perovskite Crystal towards Efficient Charge Transport in FASnI$_3$ Perovskite Solar Cells. *Sol. RRL*. **2020**, 4, 2000153.

(95) Li, B.; Chang, B.; Pan, L.; Li, Z.; Fu, L.; He, Z.; Yin, L. Tin-Based Defects and Passivation Strategies in Tin-Related Perovskite Solar Cells. *ACS Energy Lett.* **2020**, 5, 3752-3772.

(96) Karim, M. A.; Matsuishi, K.; Chowdhury, T. H.; Abdel-Shakour, M.; He, Y.; Islam, A. Additive-Assisted Electronic Defect Passivation in Lead-Free Tin Perovskite Solar Cells: Suppression of Sn^{2+} Oxidation and I$^-$ Losses. *ACS Appl. Energy Mater.* **2022**, 5, 15038-15047**.**

List of Publications

During my Ph.D. studies

I) Peer-Reviewed Journals

(1) **Md. Abdul Karim**, Kiyoto Matsuishi, Towhid H. Chowdhury, Muhammad Abdel-shakour, Yulu He, and Ashraful Islam. Additive-Assisted Electronic Defect Passivation in Lead-Free Tin Perovskite Solar Cells: Suppression of Sn^{2+} Oxidation and I^- Losses. *ACS Appl. Energy Mater.* **2022,** 5, 15038-15047.

(2) **Md. Abdul Karim**, Kiyoto Matsuishi, Towhid H. Chowdhury, Wasif Islam Chowdhury, Muhammad Abdel-shakour, and Ashraful Islam. Bathocuproine Interfacial Layer Leads to Solid Improvement of Reproducibility and Stability of Pb-Free CsBi3I10 Based Perovskite Solar Cells. *J Mater Sci: Mater Electron* **2022**, 33, 8114–8126.

(3) Muhammad Abdel-Shakour, Towhid H. Chowdhury, Kiyoto Matsuishi, **Md. Abdul Karim**, Yulu He, Yutaka Moritomo, and Ashraful Islam. Diaminomaleonitrile Lewis Base Additive for Push-Pull Electron Extraction for Efficient and Stable Tin-Based Perovskite Solar Cells. *ACS Appl. Energy Mater.* **2021**, 4, 12515–12524.

(4) Shamim Ahmmed, **Md. Abdul Karim**, Md. Hafijur Rahman, Asma Aktar, Md. Rasidul Islam, Ashraful Islam, and Abu Bakar Md. Ismail. Performance Analysis of Lead-Free $CsBi_3I_{10}$-Based Perovskite Solar Cell through the Numerical Calculation. *Sol. Energy* **2021**, 226, 54- 63.

(5) **Md. Abdul Karim**, Kiyoto Matsuishi, Md. Emrul Kayesh, Yulu He, and Ashraful Islam. Inhibition of Sn^{2+} Oxidation in $FASnI_3$ Perovskite Precursor Solution and Enhanced Stability of Sn-Based Perovskite Solar Cells by Multifunctional Additive. (**Under Preparation for Submission**).

II) Conferences

(1) **Md. Abdul Karim**, Kiyoto Matsuishi, Towhid H. Chowdhury, Wasif Islam Chowdhury, Muhammad Abdel-Shakour, Ashraful Islam. Reproducibility and Stability of Pb-free $CsBi_3I_{10}$ based Perovskite Solar Cells Improved by Bathocuproine Interfacial Layer. (**Oral Presentation**)

Acknowledgement

Time moves fast. I started my Ph.D. study about 3 years ago at the University of Tsukuba. I am unable to express how much I appreciate all your assistance and support throughout my research. Without all your support, I would never have been able to get to this point in my life.

First, I would like to express my cordial thanks to my supervisor, **Professor Kiyoto Matsuishi**, Faculty of Pure and Applied Sciences, University of Tsukuba. He trusted me and gave me the opportunity to join his research group as well as he always provided continuous support and encouragement. During my Ph.D. studies, **Professor Matsuishi** always helped me to go in the right direction in my research, and he always strongly motivated me to scientific results of my research. He was always beside me to solve my problems, answer my questions, review my paper, and support me in my academic work. Without his strong motivation, guidance, and help, I will not be able to do my doctoral studies.

Also, I would like to express my cordial thanks to **Professor Ashraful Islam**, Photovoltaic Materials Group, National Institute for Materials Science (NIMS). **Professor Islam** trusted me and allowed me to work under his group and guidance. He gave me the opportunity to fabricate solar cells by myself. He gave me endless time to solve research-related problems and discussed my findings with me. He always reviewed my work and gave me the right directions. I am very grateful for his support and time.

I'd also like to thank all the people who have worked in the Matsuishi lab in the past and the present for being friendly, giving technical support, and being helpful inside and outside of the lab. I would like to convey my gratitude and profound acknowledgement to my group member at the National Institute of Materials Science (NIMS), namely Dr. Towhid H. Chowdhury, Dr. Md. Emrul Kayesh, Dr. Muhammad Abdelshakour Muhammad Youssef, Mr.Yulu He. I am thankful to Ms. Harue Nagata for administrative support at NIMS.

I am highly thankful to the Japanese government for providing me the financial support for the whole period of research work as the MONBUKAGASHO (MEXT) scholar.

Finally, I would like to thank my parents and my family for their encouragement, patience, sacrifice and unconditional love during my work. Last but not least, I would like to thank my wife, Nadia Sultana, for

Acknowledgement

her sacrifice, patience, care, love, support, and knowledge that provided me the wisdom to pursue my Ph.D. degree throughout all these years.

Throughout my study period at the University of Tsukuba, each and every success and advancement that I have achieved has been strongly connected to the care and support that I have received from my supervisor, lab members, family, and friends. Once again, many thanks for all of them, and I hope the best for them in the future!

Md. Abdul Karim
February 2023
University of Tsukuba, Japan